RIVISTA DEL NUOVO CIMENTO Vol. 38, N. 1 2015
DOI 10.1393/ncr/i2015-10108-x

Parity violation in electron scattering

G. M. Urciuoli

INFN, Sezione di Roma - I-00185 Roma, Italy

received 1 September 2014

Summary. — A review of the experiments that measured the Parity Violating asymmetry in electron scattering is given. A description of the experimental apparatus and of the employed techniques as well as of the goals achieved is given for each experiment. The most important experiments that in the near future will perform Parity Violating asymmetry measurements and the physics fields interested by them (above all the search for physics Beyond the Standard Model) are provided.

PACS 11.30.Er – Charge conjugation, parity, time reversal, and other discrete symmetries.
PACS 12.15.Mm – Neutral currents.
PACS 24.80.+y – Nuclear tests of fundamental interactions and symmetries.
PACS 25.30.Bf – Elastic electron scattering.

1. – Introduction

In physics, a symmetry is defined as a feature of a system that is preserved or remains unchanged under some transformation. An important example of symmetry is the invariance of the form of physical laws under arbitrary differentiable coordinate transformations. There exist continuous symmetries, that are characterized by invariance following a continuous change in the geometry of the system. Spatial translational and rotational invariances and time translational invariance are, for instance, three of them. There exist discrete symmetries too, that describe non-continuous changes in a system, like, for example, time reversal and space inversion. Several invariances are fulfilled in physics: Parity conservation, that is the invariance of physics laws under spatial coordinate reversal ($x \to -x$; $y \to -y$; $z \to -z$), that was considered axiomatically true up to the second half of 1950s, is not. When this fact was discovered scholars were astonished: coordinate reversal is equivalent to a mirror reflection along an axis followed by a 180° rotation around that axis. Because rotational invariance holds true, parity violation means that mirror symmetry is not a feature of nature. In fact, this is just the case for the weak interaction. Parity violation in weak interactions was for the first time supposed by T. D. Lee and C. N. Yang in 1956 [1]. They also indicated how significant experimental tests should be performed. Two systems initially symmetric are allowed to evolve under the interaction to be tested. If there exists a left-right (L-R) asymmetry in the final state, there is Parity Violation (PV). One of the experiments they suggested was performed the following year (1957) by Chien Shiung Wu [2], who reported a nearly maximum asymmetry in the β-disintegration of polarized ^{60}Co nuclei, observing that most of the electrons emitted in the β decay favored a very specific direction of decay, opposite to that of the nuclear spin. It could be surprising that after more than fifty years scholars are still studying parity violation. This is because parity is violated only in the weak interaction. Despite its discovery several years ago, several features of the weak interaction remain elusive. For example, the Standard Model predicts the values of weak couplings and of the weak charge of several fundamental particles but the measurements of these quantities are so far very unsatisfactory. This is caused by the fact that the weak interaction is part of the more general electroweak interaction. In most experiments, the study of the weak interaction is hence very difficult because of the presence of the electromagnetic part of the electroweak interaction whose strength is overwhelmingly much bigger than that of the weak interaction and hides consequently the contribution of the weak part of the electroweak interaction. When, however, one measures Parity Violating asymmetries, that is, observes a reaction in one frame and then measures the same reaction in the mirror symmetric frame and at last calculates the fractional difference of the measurements performed this way, the pure contribution of the electromagnetic part of the electroweak interaction vanishes (electromagnetic forces are parity conserving) and one can observe the contribution of the weak part of the electroweak interaction thanks to its interference with the electromagnetic part. Because the weak interaction is a fundamental one, it does not surprise that several fields are involved in these studies: electron scattering, atomic physics, hadronic physics, search for electric dipole momentum, etc. The experimental techniques vary very much with the physics field involved. Nevertheless all of them have in common the search of a Parity Violating asymmetry. These asymmetries are usually very small (their range usually is 10^{-4}–10^{-7}) and this fact makes Parity Violation experiments extremely difficult to be performed from several points of view: they need high sensitivity and efficiency and they have to collect high statistics while keeping the systematic errors so small that the asymmetry can be

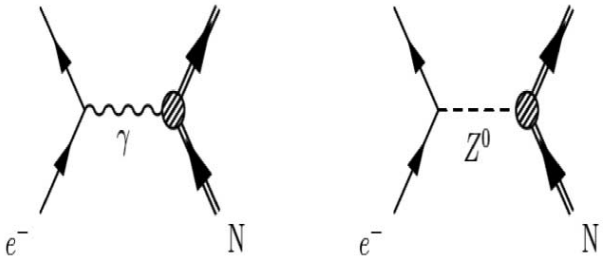

Fig. 1. – An electron e^- scatters from a nucleon N exchanging a virtual photon γ, left, and a neutral weak boson Z^0, right.

observable. This last requirement is particularly challenging, because one has to be sure that the experimental conditions do not change when switching from left-handed to right-handed systems. A complete overview of Parity Violation experiments carried out in physics would probably require an entire volume. We limit ourselves here to the description of Parity Violation in Electron Scattering (PVES). The common features of the PVES experiments, and the techniques employed and the experimental challenges one has to face when performing them are presented in sect. **2**. There will follow sections dedicated to the different physical goals achievable when dealing with Parity Violation in Electron Scattering.

2. – Parity Violation in Electron Scattering (PVES): Overview

Electrons interact with matter through the electroweak force. Consequently, as a rule, electrons of different helicity have different cross-sections when interacting with nuclei and nucleons and a Parity Violation can be observed in electron scattering. Elastic scattering of an electron, e^- from a nucleon (or a nucleus) is described to the first order by the Feynman diagrams shown in fig. 1. The invariant amplitude associated with these diagrams is given by the quantum interference between the invariant amplitudes associated with each individual diagram

$$\mathcal{M} = \mathcal{M}_\gamma + \mathcal{M}_Z, \tag{1}$$

where $\mathcal{M}_\gamma$ and $\mathcal{M}_Z$ are the invariant amplitudes associated with a single photon and Z-boson exchange, respectively.

Far from the Z^0 pole, the electromagnetic interaction dominates by several orders of magnitude over the neutral weak interaction. A direct cross-section measurement of the reaction in fig. 1 will completely obscure the effects of the neutral weak interaction in the measured observable. However, since the weak interaction violates parity, a pseudoscalar observable can be formed whose measurement sheds light on the neutral weak interaction. This pseudoscalar observable is the Parity Violating asymmetry defined as

$$A_{\mathrm{PV}} = \frac{\sigma_R - \sigma_L}{\sigma_R + \sigma_L}, \tag{2}$$

where σ_R (σ_L) is the cross-section for scattering longitudinally polarized electrons that are in the right-handed (left-handed) helicity state (that is whose spins are parallel (an-

tiparallel) to their momenta). In fact, because the cross-sections are proportional to $|\mathcal{M}_\gamma + \mathcal{M}_Z|^2$ and because $\mathcal{M}_\gamma^2$ is equal for left- and right-handed electrons (electromagnetic forces are parity conserving), considering that $\mathcal{M}_\gamma^2 \gg \mathcal{M}_Z^2$, A_{PV} is proportional to the ratio of the weak and electromagnetic amplitudes and $\mathcal{M}_Z$ can be hence measured with satisfactory precision.

The PVES experiments employ common (although improved constantly with time) techniques that are shortly described in this section as separate subsections. To avoid too technical details only the essential of these techniques will be given. The techniques and the peculiarities proper to each experiment will be described with the experiments themselves in the following sections.

2˙1. *Electron source and electron beam.* – The experimental technique in PVES experiments can be conceptually described as follows: the helicity of the primary electron beam is rapidly and randomly flipped in order to create a pseudorandom time sequence of helicity "window pairs" in which the electron beam helicity is opposite. The rapid and random flips of the helicity ensures that the influences of the drifts of the experimental set-up is minimized when calculating the fractional difference in the detector response over window pairs. The helicity of the electron beam is usually controlled by the polarity of the voltage applied to a Pockels cell which is essentially a voltage-controlled retardation plate. The Pockels cell is configured to convert a laser linearly polarized light to right- or left-circularly polarized light. The polarity of the potential difference across the Pockels cell face determines the handedness of the laser beam at the exit of the cell. The circularly polarized laser exiting the Pockels cell illuminates a GaAs photocathode to produce polarized electrons whose helicity state depends on the handedness of the laser beam.

2˙2. *Asymmetry measurement.* – In PVES experiments, in order to accumulate the required statistics at a high rate, the relative scattered flux is often (but not always) measured by integrating the response of the detector rather than by counting individual particles (in the following sections, unless otherwise specified, in the description of the experiments, it will be implicitly assumed that integrating techniques will be used to determine the detector response). The fractional difference in the detector response over window pairs is then calculated. For each windows pair the expression

$$A = \frac{N_R - N_L}{N_R + N_L} \tag{3}$$

is hence calculated, where N_R (N_L) is the detector response for right-handed (left-handed) incident electrons. For each run the mean of the asymmetry values given by (3) weighted by the beam current is then calculated:

$$\langle A \rangle = \frac{\sum w_k \cdot A_k}{\sum w_k}, \tag{4}$$

where w_k is the total beam current in the $k_t h$ window pair. Usually the whole data are divided in n samples where (4) is performed in order to obtain n independent measurements of the asymmetry $\langle A \rangle$, each with its own error $\delta\langle A \rangle$ estimated from the width of the distribution. The final value of the asymmetry (that we call "raw asymmetry" for reasons that will be clear later) is then calculated by performing the mean of the n $\langle A \rangle$ values given by (4) weighted by their errors $\delta\langle A \rangle$.

2˙3. *Corrections for beam position and energy correlations.* – Extreme care should be taken in PVES experiments in order to keep under control systematic effects that depend on beam helicity: the dependence on beam helicity of beam parameters like energy, position, direction, and intensity has to be kept as low as possible in order to avoid the so-called "false asymmetries". Because a certain degree of helicity-correlated systematic effects are unavoidable, to correct the value of the measured asymmetry for the false asymmeteries, a modulation on beam parameters like position, angle, and energy is usually performed periodically during the experiment. In this way one can determine the variations in the detector response caused by changes, with respect to the mean values, of the beam parameters and correct the measured raw asymmetry through the formula

$$\langle A\rangle_{\rm corr} = \langle A\rangle - \langle \Delta A\rangle, \tag{5}$$

with

$$\Delta\langle A\rangle = \sum \langle a_j\rangle \cdot \langle B_j\rangle, \tag{6}$$

where the index j points out one of the beam parameters (position, angle, energy), $\langle B_j\rangle$ is the average difference of the j-th parameter between positive and negative helicity electrons and a_j is defined as

$$a_j = \frac{\frac{\partial d}{\partial B_j}}{2\langle d\rangle}, \tag{7}$$

where $\langle d\rangle$ is the averaged normalized signal for the detector.

From the point of view of beam charge changes with the electron helicity, special effort has to be employed to minimize the so-called PITA (Polarization-Induced Transport Asymmetry) effect [3], due to a combination of imperfect alignment of the Pockels cell and small amounts of birefringence in other elements of the optical system. This effect makes small amount of linear polarization be retained by the circular polarized laser light that produces the electron beam by illuminating the photocatode. The linear component has different orientations for the two helicities. Any optical element which the beam passes through at non-normal incidence transmits in-plane and out-of-plane linear polarization with different efficiencies. Since the two helicities have their linear components oriented differently, they are transmitted differently, resulting in an intensity asymmetry. The PITA effect can be reduced changing the voltage applied to the Pockels cell after calculating the intensity asymmetry at fixed time intervals [4].

2˙4. *Corrections for background.* – Processes different from the one under study contribute generally to the value of $\langle A\rangle_{\rm corr}$ of eq. (5) too. These processes, that will be described with the experiments in the corresponding sections, constitute a background that has to be eliminated. The physics asymmetry is hence given by the formula

$$A_{\rm phys} = \frac{1}{P_b}\frac{\langle A\rangle_{\rm corr} - P_b\sum_i A_i f_i}{1-\sum_i f_i}, \tag{8}$$

with P_b the beam polarization, f_i the fraction of the i-th source of background and A_i the asymmetry of that source.

2˙5. *Correction for electronic crosstalk.* – Special care is taken, in PVES experiments, to ensure a very good ground isolation, from the rest of the experiment, of the circuit which controls the helicity sequence and timing structure of the polarization of the electron beam providing the Pockels cell with positive or negative high voltages. Very useful to cancel out some helicity-correlated systematic effects, like possible electronic crosstalk of the high voltage signals fed to the Pockels cells to the data taking system, is the insertion of devices like half-wave plates (along the optical path of the laser light) and Wien filters (along the electron beam path) which revert the electron beam helicity leaving the experimental apparatus untouched.

2˙6. *Correction for detector nonlinearities.* – Among the other issues PVES experiments have to deal with we can mention the nonlinearity of the detector response. If the detector response S is not perfectly linear, that is the ratio between it and the beam intensity I is given by the formula

$$\frac{S^{\pm}}{I^{\pm}} = b^{\pm} + cI^{\pm}, \tag{9}$$

where the coefficient c is a measure of the nonlinearity and the indices $+$ and $-$ refer to the quantities relative to positive and negative beam electron helicity, respectively, the measured asymmetry will be

$$\frac{\frac{S^+}{I^+} - \frac{S^-}{I^-}}{\frac{S^+}{I^+} + \frac{S^-}{I^-}} = A_{\mathrm{PV}} + A_n^f \approx \frac{b^+ - b^-}{b^+ + b^-} + \frac{c}{b} I A_I, \tag{10}$$

where A_n^f is the false asymmetry generated by the nonlinearity of the detector and A_I is the beam intensity asymmetry (that is the fractional difference of the beam intensty over window pairs). Extreme care should be taken hence to minimize the ratio $\frac{c}{b}$ and A_I.

2˙7. *Polarimetry.* – Polarimetry is another non-trivial issue of PVES experiments, whose importance was crucial especially in the most recent experiments that required measurements of the Parity Violating asymmetry with very high precision, as underlined by the fact that the polarimetry error is still the largest contribution to the systematic error budget. Several kinds of polarimeters were used in PVES. Mott polarimeters and transmission polarimeters are two examples. We limit ourselves here to the description of two kinds of polarimeters that have been used since (nearly) the beginning and that have emerged as the most effective, being continuously improved over the years: Møller polarimeters and Compton polarimeters.

A Møller polarimeter measures the beam polarization by measuring the asymmetry in $\mathrm{e}^- + \mathrm{e}^- \to \mathrm{e}^- + \mathrm{e}^-$ scattering, which depends on the beam and target polarizations P^{beam} and P^{target}. The Møller cross-section is proportional to

$$\sigma_{\mathrm{M\o ller}} \propto \left[\sum_{i=X,Y,Z} 1 + A_{ii} \cdot P_i^{\mathrm{beam}} \cdot P_i^{\mathrm{target}} \right], \tag{11}$$

where $i = X; Y; Z$ defines the projections of the polarizations (Z is parallel to the beam, while Z-X is the scattering plane). The analyzing powers A_{ii} depend on the scattering

angle in the center of mass frame (θ_{CM}) and are calculable in QED:

$$A_{ZZ} = \frac{\sin^2\theta_{CM}(7+\cos^2\theta_{CM})}{(3+\cos^2\theta_{CM})^2}; \quad A_{XX} = \frac{\sin^4\theta_{CM}}{(3+\cos^2\theta_{CM})^2}; \quad A_{YY} = -A_{XX}. \tag{12}$$

The absolute values of A_{ZZ} reach the maximum of $\frac{7}{9}$ at $\theta_{CM} = 90°$. At this angle the transverse analyzing powers are $A_{XX} = -A_{YY} = \frac{A_{ZZ}}{7}$.

A Møller polarimeter detects, through a magnetic spectrometer, the electrons Møller-scattered in a ferromagnetic foil magnetized in a magnetic field. At a given target angle, the helicity-driven fractional difference (asymmetry) of the counting rate will be equal to

$$A_{\text{Møller}} = \sum_{i=X,Y,Z} A_{ii} \cdot P_i^{\text{beam}} \cdot P_i^{\text{target}}. \tag{13}$$

The asymmetry can be measured at two opposite target angles and the average taken, which cancels transverse contributions and reduces the uncertainties of target angle measurements. At a given target angle two sets of measurements with oppositely signed target polarization can be made which cancel some false asymmetries such as beam current asymmetries. If the electron detector is split into two arms the two scattered electrons can be detected in coincidence, reducing the background. Up to recent times the principal limitation to a very high precision polarimetry with a Møller polarimeter was the poor knowledge of the target polarization. In fact, because of the use of Fe alloys as targets, the target had to be saturated at a low magnetic field (of order of 100 Gauss). Then a precise measurement of the target magnetization was needed as well as a comparison between the value of the magnetization at the edges and at the center of the target. Above all, because both spin and orbital movements of the electrons contribute to the magnetization, the spin polarization of the target electrons was not known better than 3%. This problem is being solved with the use, as targets, of pure iron saturated foils in very high magnetic fields (of the order of 4 T). In this case, the spin polarization is known at the level of 0.25% and the systematic error in the beam polarization measurement is consequently reduced.

Compton polarimeters use the spin dependence of the electron-photon scattering cross-section by colliding polarized (usually optical) photons with the electron beam and detecting the final-state photon and/or electron. In the case of a polarization-insensitive detector, the photon scattering cross-section is given by

$$\frac{\mathrm{d}\sigma(\vartheta,\varphi)}{\mathrm{d}\Omega} = \frac{\mathrm{d}\sigma_0(\vartheta)}{\mathrm{d}\Omega} + Q\frac{\mathrm{d}\sigma_1(\vartheta)}{\mathrm{d}\Omega} - VP_e^{\text{long}}\frac{\mathrm{d}\sigma_2^{\text{long}}(\vartheta)}{\mathrm{d}\Omega} - VP_e^{\text{trans}}\cos\varphi\frac{\mathrm{d}\sigma_2^{\text{trans}}(\vartheta)}{\mathrm{d}\Omega}, \tag{14}$$

where ϑ, φ are the polar and azimuthal photon scattering angles, respectively, P_e is the electron polarization, and Q, V are the "Stokes Parameters" describing the incident photon polarization (Q being the linear, V the circular component). The second term is a nuisance contribution usually eliminated by the use of purely circular light (*i.e.* $Q = 0$). The third and fourth term are those allowing the measurement of the electron polarization; however, since the cross-section is strongly peaked around the beam direction, the last term vanishes as the $\cos\varphi$ dependence is averaged out by photon detectors of commonly used sizes. Thus, switching the photon polarization between right- and

left-circular ($V = \pm P_\gamma$, where $P_\gamma > 0$) gives rise to a cross-section asymmetry

$$A^{\text{long}}_{\text{Compton}} = -P_\gamma P_e^{\text{long}} \left(\frac{\mathrm{d}\sigma_2^{\text{long}}}{\mathrm{d}\Omega}\right) \Big/ \left(\frac{\mathrm{d}\sigma_0}{\mathrm{d}\Omega}\right) = P_\gamma P_e^{\text{long}} \mathcal{A}^{\text{long}}, \tag{15}$$

from which the longitudinal electron polarization can be extracted if P_γ is known. Determination of P_e^{trans} is possible if a position-sensitive detector is used. Compton polarimeters are installed in magnetic chicanes in order to separate the outgoing electrons from the backscattered photons. The photon source is implemented by a laser that provides an intense, focused beam with a highly pure polarization. The output of a commercial laser is fed into a Fabry-Pérot cavity, wherein constructive interference between incident and recirculating light leads to a reasonant build-up of intensity, that increases the otherwise too small luminosity. The backscattered photon, which is boosted to gamma-ray energies, and, in modern polarimeters, the final-state electron are detected. Finally, a polarization measurement device for the laser beam is required in order to determine the photon P_γ and ensure the correct polarization state. With respect to Møller polarimeters, Compton polarimeters have the advantage to be non-invasive and to perform hence polarization measurements immediately in front of and at the same beam conditions as the experiment. On the other hand, a Compton polarimeter has a low analyzing power.

In the last experiments performed at JLab, the (sometimes combined) use of Compton polarimeters using a thresholdless integration of the photon signal, and of Møller polarimeters improved through the use of targets consisting of a pure Fe foil, brute-force polarized out of plane with a 3-4 T superconducting magnet accomplished a measurement of the electron beam polarization at the level of 1%. Even more precise polarization measurements, $< 0.5\%$, will be needed in future experiments and an effort is in progress to achieve this very challenging goal by improving Møller and Compton polarimeters techniques.

2˙8. *A PVES short history.* – When dealing with Parity Violating asymmetry measurements the first thing one has to consider is that the asymmetries concerned are very small. In fact, the scale of the Parity Violating asymmetry in electron scattering is (see eq. (1)) $\frac{|\mathcal{M}_Z|}{|\mathcal{M}_\gamma|} \sim \frac{Q^2}{M_Z^2}$, with Q^2 the square of the four-vector momentum transfer and M_Z the Z^0 boson mass. The experiment that for the first time measured the Parity Violation in electron scattering was the experiment SLAC E122 [5,6], that observed Parity Violation in electron-deuterium scattering with a statistical significance bigger than 10σ. This result unequivocally confirmed the parity-violating predictions of electroweak unification. For their work on electroweak unification and its implications, Sheldon Lee Glashow, Abdus Salam and Steven Weinberg received the physics Nobel prize in 1979. Because the experiment SLAC E122 aimed essentially to prove the Parity Violation in electron scattering, it performed a measurement at a relatively high value of Q^2, where the expected asymmetry was relatively big. To have a glance at the following history, one can look at table I and table II, that show the main features of PVES experiments performed so far. From table I it can be observed that the measured asymmetries as well as the percentage statistical and systematic errors decrease constantly with time. This is due to the use of electron beams of better and better quality and the use of more and more sophisticated technologies as can be guessed from table II. This table shows both the increase with time of the intensity of the beams used, that implied a decrease of the statistical error of the measurements, and the increase with time of the

TABLE I. – *Synoptic table of the measured asymmetries, in part per milion, of the experiments described in this paper. The first and the second error quoted beside the measured asymmetries are always the statistical and the systematic error, respectively. The E122 result quoted is the A/Q^2 value measured in the experiment with the deuterium target times the Q^2 average value this measurement was performed at. The G0_Backward systematic errors are the sum in quadrature of the point-to-point and global systematic errors reported in the relative paper. Q_{weak} result is obtained from an analysis of just 4% of the total data taken by the experiment.* A4 *has not published results relative to data collected after* 2006 *yet. The experiment MOLLER will run in the future. The asymmetry and the errors quoted in the corresponding row are the expected values. Q^2 values in* $(\mathrm{GeV/c})^2$.

Experiment	Laboratory	Year	Measured Asymmetry (ppm)
E122	SLAC	1978-1979	$-275 \pm 25 \pm 22$
Mainz	Mainz Linac	1986	$-9.4 \pm 1.8 \pm 0.5$
MIT 12C	MIT-BATES	1988	$0.60 \pm 0.14 \pm 0.02$
SAMPLE	MIT-BATES	1998	$-5.61 \pm 0.67 \pm 0.88$
SAMPLE-II	MIT-BATES	1999	$-7.77 \pm 0.73 \pm 0.62$
HAPPEX	JLAB	1998-1999	$-15.05 \pm 0.98 \pm 0.56$
SAMPLE-III	MIT-BATES	2000-2001	$-3.51 \pm 0.57 \pm 0.58$
A4_Forward	MAMI	2000-2003	$-5.44 \pm 0.54 \pm 0.26$ ($Q^2 = 0.230$) $-1.36 \pm 0.29 \pm 0.13$ ($Q^2 = 0.108$)
E158	SLAC	2000-2003	$-0.131 \pm 0.014 \pm 0.010$
G0_Forward	JLAB	2002 and 2004	see fig. 12
HAPPEX-II ^{4}He	JLAB	2004-2005	$6.72 \pm 0.84 \pm 0.21$ (2004) $6.40 \pm 0.23 \pm 0.12$ (2005)
HAPPEX-II H	JLAB	2004-2005	$-1.14 \pm 0.24 \pm 0.06$ (2004) $-1.58 \pm 0.12 \pm 0.04$ (2005)
A4_Backward	MAMI	2006	$-17.23 \pm 0.82 \pm 0.89$
G0_Backward H	JLAB	2006-2007	$-11.25 \pm 0.86 \pm 0.51$ ($Q^2 = 0.221$) $-45.9 \pm 2.4 \pm 1.3$ ($Q^2 = 0.628$)
G0_Backward ^{2}H	JLAB	2006-2007	$-16.93 \pm 0.81 \pm 0.46$ ($Q^2 = 0.221$) $-55.5 \pm 3.3 \pm 2.1$ ($Q^2 = 0.628$)
HAPPEX-III	JLAB	2009	$-23.80 \pm 0.78 \pm 0.36$
PVDIS	JLAB	2009	$-160.8 \pm 6.4 \pm 3.1$ ($Q^2 = 1.901$) $-91.1 \pm 3.1 \pm 3.0$ ($Q^2 = 1.085$)
PREX	JLAB	2010	$0.656 \pm 0.060 \pm 0.014$
Q_{weak}	JLAB	2010-2012	$-0.279 \pm 0.035 \pm 0.031$
MOLLER	JLAB	upcoming	$0.033 \pm 0.0007 \pm 0.0003$

TABLE II. – *Synoptic table of beam parameters and targets employed in the experiments described in this paper. Q^2 values in* $(\mathrm{GeV/c})^2$.

Experiment	Beam energy (GeV)	Beam polarization (%)	Beam intensity (μA)	Target
SLAC E122	16.2-22.2	$(37 \pm 0.9)\%$	2-8	Deuterium
	19.4	"	"	Hydrogen
Mainz	0.300	$(44.9 \pm 1.8)\%$	6.9	Beryllium
	"	$(43.8 \pm 1.8)\%$	7.5	"
MIT 12C	0.250	$(37 \pm 2)\%$	30-60	Carbon
SAMPLE	0.200	$(34.8 \pm 1.5)\%$	40	Hydrogen
SAMPLE-II	0.200	$(35.7 \pm 1.4)\%$	40	Deuterium
HAPPEX (1998)	3.356	$(38.8 \pm 2.7)\%$	100	Hydrogen
HAPPEX (1999)	3.3	$\approx (70 \pm 2.2)\%$	35	Hydrogen
SAMPLE-III	0.125	$(38.9 \pm 1.6)\%$	40	Deuterium
A4_forward ($Q^2 = 0.230$)	0.8543	$\approx (80 \pm 4.0)\%$	20	Hydrogen
A4_forward ($Q^2 = 0.108$)	0.5704	$\approx (80 \pm 4.0)\%$	20	Hydrogen
SLAC E158 (2002)	45.0	$(85 \pm 5)\%$	8-12	Hydrogen
	and			
	48.3		8-12	
SLAC E158 (2003)	45.0	$(89 \pm 4)\%$	8-12	Hydrogen
	and			
	48.3		8-12	
G0_forward	3.031	$(73.7 \pm 1.0)\%$	40	Hydrogen
HAPPEX-II_Hydrogen (2004)	3.03	$(81.3 \pm 1.6)\%$	35	Hydrogen
HAPPEX-II_Helium (2004)	3.03	$(86.9 \pm 1.7)\%$	35	^{4}He
HAPPEX-II_Hydrogen (2005)	3.18	$(87.1 \pm 0.9)\%$	35-55	Hydrogen
HAPPEX-II_Helium (2005)	2.75	$(84.4 \pm 0.8)\%$	35-55	^{4}He
A4_backward	0.3151	$(68.3 \pm 4.0)\%$	20	Hydrogen
G0_backward	0.359	$(85.8 \pm 2.1)\%$ (1.4)%	60	Hydrogen
	and			and
	0.684			Deuterium
HAPPEX-III	3.481	$(89.36 \pm 0.75)\%$	100	Hydrogen
PVDIS ($Q^2 = 1.085$)	6.067	$(88.18 \pm 1.76)\%$	100	Deuterium
PVDIS ($Q^2 = 1.901$)	6.067	$(89.29 \pm 1.19)\%$	100	Deuterium
PREX	1.06	$(89.2 \pm 1.0)\%$	50-70	Lead
Q_{weak}	1.155	$(89.0 \pm 1.8)\%$	145	Hydrogen

polarization of the beams used, associated with a decrease of the percentage statistical and systematic errors of the polarization measurements due to the improved polarimetry technologies. The history of polarimetry is just an example of the improvements that several technologies employed in PVES experiments underwent over the years. These improvements and the associated ability to measure ever smaller asymmetries made the experimentalists dealing with Parity Violating asymmetry more and more ambitious with respect to their goals. In fact, depending on the kinematics and targets employed, several different physical quantities can be measured through (2). The first PVES experiments measured tree-level parameters of the Standard Model. Taking them for granted, PVES experiments investigated then nucleon and nuclear physics questions, like strange form factors and neutron radius in heavy nuclei. These experiments required the ability to measure asymmetries of the order of 10^{-6}. The ability to measure even smaller asymmetries with very high precision is starting new series of experiments that go back to the original question. This time, however, PVES experiments are not aiming to test tree level, but rather to improve our understanding of the Standard Model. In fact, any measured deviation from Standard Model predictions can have two sources: electroweak radiative corrections or new physics beyond the Standard Model. In this respect a new effort is expected from theoreticians to decrease substantially the theoretical uncertainties. All the parity experiments performed so far (beside the early ones) relied heavily on the Standard Model by comparing the Parity Violating asymmetries measured with the corresponding values calculated by the Standard Model. Equations (20) and (28), for example, are calculated in the framework of the Standard Model. To derive from them the contribution of strange form factors to the ground-state charge and magnetization distributions of the nucleon, the values predicted by the Standard Model assuming the contributions of these strange form factors equal to zero were compared with the experimental results. In this comparison, the value of the weak mixing angle was assumed for granted as well as the values derived from Standard Model calculations of the axial form factors (especially of their small isoscalar component), of the electroweak radiative corrections, etc. In fact, the theoretical uncertainties on these values, as well as the experimental uncertainties on electromagnetic form factors, were small enough to not affect the measurements significantly more than the experimental statistical and systematic uncertainties and were included in the overall error. However, in the new series of PVES experiments, aimed at the extraction of the weak mixing angle value, the size and q-dependence of higher-order electroweak radiative corrections, etc., the expected experimental statistical and systematic errors will be so small to make the present theoretical uncertainties much more significant. Theoretical efforts are hence needed to improve our knowledge on the size of nuclear and nucleon structure effects involved, like, for example, when dealing with Parity Violation asymmetry in electron scattering from nuclei, the distortion of the electron wave function due to the Coulomb field created by the nuclear charge distribution, the isospin mixing in the nucleus due to the Coulomb interaction acting differently on protons and neutrons, the meson exchange currents among the nucleons that affect differently the isoscalar and the isovector nuclear responses, the strangeness content of the nucleons that modifies the isoscalar (but not the isovector) nuclear responses and possible nuclear inelastic transitions in the scattering process [7]. PVES experiments are not the only ones that will search for evidence of physics beyond the Standard Model. Atomic Parity Violation experiments, neutrino scattering experiments, experiments at colliders like LHC will pursue this goal as well. Nevertheless, rather than in competition among each other these different kinds of experiments will be complementary, employing completely different techniques. For example, while LHC will

perform a direct search for physics beyond the Standard Model, PVES experiments will seek signals of new dynamics in violations of symmetry at lower center-of-mass energies, focusing on processes where the Standard Model expectations are known to high accuracy or are predicted to be zero. Just to quote a specific case, LHC has discovered a scalar resonance with a mass of 126 GeV, consistent with precision electroweak measurements, and with branching ratios consistent (within available statistics) with that predicted for a Standard Model Higgs boson. Under the assumption of a Standard Model Higgs boson mass of 126 GeV, the theoretical prediction for the Parity Violation asymmetry in Møller scattering is known to better than 0.2 part per billion accuracy. The MOLLER experiment (see sect. **5**˙3) aims to measure this Parity Violation asymmetry with an error of 0.6 part per billion; any deviation at this level is a signature of new dynamics beyond the Standard Model. The importance of the goals pursued by the new generation of PVES experiments surely justifies the enormous financial budget allocated for them with the construction of very sophisticated apparatuses like SOLID (see sect. **5**˙1) and the one designed for the experiment MOLLER.

This paper will describe in the order: strange form factor measurements (sect. **3**), the measurement of the neutron radius in heavy nuclei (sect. **4**), the measurement of the weak couplings between the electrons and the up/down quarks and of the weak mixing angle (sect. **5**˙1), the measurement of the weak charge of the proton (sect. **5**˙2) and of the weak charge of the electron (sect. **5**˙3), and the measurement of the Parity Violating asymmetry in the nucleon resonance region (sect. **6**). In the following sections, the electron polarization referred to will always be implicitly the longitudinal polarization, unless otherwise specified. This review will not include the measurements of the asymmetry in the scattering of electrons with a polarization perpendicular with respect to the scattering plane (measurements of the transverse beam asymmetry). These measurements are a byproduct of the experiments measuring Parity Violating asymmetries because they are needed to understand the contribution to A_{corr} coming from a not 100% longitudinally polarized electron beam and from geometrical asymmetries of the experimental apparatus. The measurement of the transverse beam asymmetry has its own importance because time-reversal symmetry dictates that it is zero at the first Born approximation and it is hence a direct probe of the need of including higher-order photon exchange for the interpretation of precision data in electron scattering. Nevertheless, the measurement of the transverse beam asymmetry belongs to a physics field different from that of the Parity Violating asymmetry measurement and will not be treated here.

3. – Strange form factors

In the nucleon, in addition to valence quarks, *i.e. uud* for the proton and *udd* for the neutron, there is a sea of gluons and $q\bar{q}$ pairs that plays an important role at distance scales similar to that of the bound state ~ 1 fm and that contributes to the ground-state charge and magnetization distributions (*e.g.*, magnetic moment) of the nucleon. It is possible to extract the contributions of strange quarks to the ground-state charge and magnetization distributions of the nucleon measuring the neutral weak scattering of electrons from protons and neutrons. In fact, since the Z^0 boson couples to various quarks with different relative strengths compared to the photon, a combined analysis of proton and neutron electromagnetic form factor and proton neutral weak form factor measurements, along with the assumption of charge symmetry, allows the determination of the strange electric and magnetic form factors [8, 9]. The strange quark contributions to the charge and magnetization of the nucleon are encoded in the strange electric and

magnetic form factors, G_E^s and G_M^s analogs of the usual Sachs form factors G_E and G_M. Purely electromagnetic scattering at a given kinematics can measure only two linear combinations of the Sachs form factors:

$$G_{E,M}^{\gamma p} = \frac{2}{3}G_{E,M}^{u} - \frac{1}{3}G_{E,M}^{d} - \frac{1}{3}G_{E,M}^{s}, \tag{16}$$

$$G_{E,M}^{\gamma n} = \frac{2}{3}G_{E,M}^{d} - \frac{1}{3}G_{E,M}^{u} - \frac{1}{3}G_{E,M}^{s}, \tag{17}$$

where $G_{E,M}^{f}$ is the electric (E) or magnetic (M) form factor for quark flavor f. Charge symmetry between proton p and neutron n is assumed, so that for the quark form factors:

$$G_p^u = G_n^d; \qquad G_p^d = G_n^u; \qquad G_p^s = G_n^s. \tag{18}$$

Additional information is needed to determine whether or not there is a contribution from the strangeness form factors, $G_{E,M}^s$. This is provided by Parity Violation in the scattering from protons, measuring a new pair of linear combinations:

$$G_{E,M}^{Zp} = \left(1 - 4\sin^2\theta_W\right)\left(1 + R_V^p\right) G_{E,M}^{\gamma p} - \left(1 + R_V^n\right) G_{E,M}^{\gamma n} - \left(1 + R_V^{(0)}\right) G_{E,M}^{s}, \tag{19}$$

where Z stands for the Z^0 boson of the neutral weak interaction, θ_W is the Weinberg angle and R_V^p, R_V^n, and $R_V^{(0)}$ are the weak radiative corrections for the vector form factors. Thus by measuring these neutral weak form factors, in conjunction with the electromagnetic form factors, the strange quark contribution can be extracted. The explicit dependence of the Parity Violating asymmetry (2) on the strangeness content, in the elastic electron scattering on the unpolarized proton, is written as follows in terms of the form factors introduced above:

$$A_{\mathrm{PV}}^p = -\frac{G_F Q^2}{4\pi\alpha\sqrt{2}} \times \left[\frac{\epsilon G_E^{\gamma p} G_E^{Zp} + \tau G_M^{\gamma p} G_M^{Zp} - \epsilon'\left(1 - 4\sin^2\theta_W\right) G_M^{\gamma p} G_A^{Zp}}{\epsilon\left(G_E^{\gamma p}\right)^2 + \tau\left(G_M^{\gamma p}\right)^2}\right], \tag{20}$$

where G_F is the Fermi constant, α is the fine structure constant, Q^2 is the square of the four-vector momentum transfer ($Q^2 > 0$), $\tau = \frac{Q^2}{4M^2}$ where M is the proton mass, $\epsilon = [1+2(1+\tau)\tan^2(\theta/2)]^{-1}$ where θ is the scattering angle, $e' = \sqrt{\tau(1+\tau)(1-\epsilon^2)}$, and G_A^{Zp} is the proton axial form factor. The asymmetry (20) contains a term with the neutral weak axial form factor G_A^{Zp} that, as explained in [10], can be estimated by combining information from neutron beta decay [11], polarized deep inelastic scattering [12], and calculations of the axial radiative correction [13, 14].

It is interesting derive the equivalents of eqs. (19) and (20) for the neutron

$$G_{E,M}^{Zn} = \left(1 - 4\sin^2\theta_W\right)\left(1 + R_V^n\right) G_{E,M}^{\gamma n} - \left(1 + R_V^p\right) G_{E,M}^{\gamma p} - \left(1 + R_V^{(0)}\right) G_{E,M}^{s}, \tag{21}$$

$$A_{\mathrm{PV}}^n = -\frac{G_F Q^2}{4\pi\alpha\sqrt{2}} \times \left[\frac{\epsilon G_E^{\gamma n} G_E^{Zn} + \tau G_M^{\gamma n} G_M^{Zn} - \epsilon'\left(1 - 4\sin^2\theta_W\right) G_M^{\gamma n} G_A^{Zn}}{\epsilon\left(G_E^{\gamma n}\right)^2 + \tau\left(G_M^{\gamma n}\right)^2}\right] \tag{22}$$

and the expressions for G_A^{Zp} and G_A^{Zn} as well

$$G_A^{Zp} = -\left(1 + R_A^{T=1}\right) G_A + \sqrt{3} R_A^{T=0} G_A^{(8)} + (1 + R_A^{(0)}) G_A^s, \tag{23}$$

$$G_A^{Zn} = \left(1 + R_A^{T=1}\right) G_A + \sqrt{3} R_A^{T=0} G_A^{(8)} + (1 + R_A^{(0)}) G_A^s. \tag{24}$$

Equations (23) and (24) can be expressed in compact way

$$G_A^e = -\left(1 + R_A^{T=1}\right) G_A \tau_3 + \sqrt{3} R_A^{T=0} G_A^{(8)} + (1 + R_A^{(0)}) G_A^s, \tag{25}$$

with G_A^e the nucleon axial form factor, $\tau_3 = +1(-1)$ for the proton(neutron), $G_A \equiv G_A^u - G_A^d$, $G_A^u \equiv G_A^{u,p} = G_A^{d,n}$, $G_A^d \equiv G_A^{d,p} = G_A^{u,n}$, $G_A^s \equiv G_A^{s,p} = G_A^{s,n}$ ($G_A^{q,p(n)}$ the contribution of the q quark to the proton (neutron) neutral weak axial form factor), T the total isospin quantum number, $R_A^{T=1}$ the isovector part of the nucleon axial radiative correction, $G_A^{(8)}$ the $SU(3)$ isoscalar octet form factor (usually neglected), and $R_A^{(0)}$ the $SU(3)$ singlet axial radiative corrections. The notation G_A^e for the nucleon axial form factor in electron scattering is used to distinguish the form factor as seen by electron scattering from that seen by neutrino scattering where the higher-order diagrams involving a photon are absent. The very poorly known corrections $R_{V,A}^{(0)}$ in eq. (19) and eq. (25) are usually absorbed in the corresponding strange form factors.

In case of an unpolarized deuterium target, the Parity Violating asymmetry is dominated by the Quasi-Elastic scattering (QE), and can be written, in the static approximation, as an incoherent sum of contributions from the proton and neutron weighted by the unpolarized cross-sections

$$A_{\rm PV}^d \approx A_{QE} \approx \frac{\sigma_p A_{\rm PV}^p + \sigma_n A_{\rm PV}^n}{\sigma_d}, \tag{26}$$

where $\sigma_p = \epsilon (G_E^{\gamma p})^2 + \tau (G_M^{\gamma p})^2$ and $\sigma_n = \epsilon (G_E^{\gamma n})^2 + \tau (G_M^{\gamma n})^2$ are terms proportional to the unpolarized elastic proton and neutron cross-sections respectively, $A_{\rm PV}^p$ and $A_{\rm PV}^n$ are the contributions to the asymmetry from the proton and neutron respectively, and $\sigma_d = \sigma_p + \sigma_n$.

This approximation must be corrected for Final-State Interactions between the nucleons and in addition there is a small contribution from the elastic scattering cross-section from the deuteron to be taken into account. A more exact expression for the Parity Violating asymmetry in case of an unpolarized deuterium target is hence

$$A_{\rm PV}^d = \frac{A_{QE}\sigma_{QE} + A_E \sigma_E}{\sigma_{QE} + \sigma_E}, \tag{27}$$

where A_{QE} and σ_{QE} are the asymmetry and the cross-section for QE scattering of the electron from the deuteron and A_E and σ_E are the asymmetry and the cross-section for elastic scattering of the electron from the deuteron. The correction for Final-State Interactions is small and can be made with little uncertainty.

In case of an unpolarized ^{4}He target, the elastic electron scattering is an isoscalar $0^+ \to 0^+$ transition and therefore allows no contributions from magnetic or axial-vector currents. The Parity Violating asymmetry at tree level is given in this case by [13]

$$A_{\rm PV}^{\rm He} = \frac{G_F Q^2}{4\pi\alpha\sqrt{2}} \times \left(4\sin^2\theta_W + \frac{G_E^s}{G_E^{\gamma T=0}}\right). \tag{28}$$

TABLE III. – *Synoptic table of the kinematic parameters and main results of the experiments described in sect.* **3**. *For the sake of homogeneity, the errors of the results reported are the sums in quadrature of all the errors quoted by the relative papers. The results of* A4 *at* $Q^2 = 0.23$ $(\mathrm{GeV/c})^2$ *are those determined without considering the* G0 *result at the same* Q^2 *value.*

Experiment	Average scattering angle	Average Q^2 $(\mathrm{GeV/c^2})$	Result
SAMPLE	146.1°	0.100	$G_M^s = 0.37 \pm 0.34$
SAMPLE-II	146.1°	0.091	$G_M^s = 0.23 \pm 0.54$; $G_A^{e(T=1)} = -0.53 \pm 0.76$
SAMPLE-III	146.1°	0.038	see fig. 3
HAPPEX	12.3°	0.477	$G_E^s + 0.392 G_M^s = 0.014 \pm 0.022$
HAPPEX-II_Hydrogen (2004)	6°	0.099	$G_E^s + 0.080 G_M^s = 0.030 \pm 0.028$
HAPPEX-II_Hydrogen (2005)	6°	0.109	$G_E^s + 0.09 G_M^s = 0.007 \pm 0.013$
HAPPEX-II_Helium (2004)	6°	0.091	$G_E^s = -0.038 \pm 0.043$
HAPPEX-II_Helium (2005)	6°	0.077	$G_E^s = 0.002 \pm 0.016$
HAPPEX-III	13.7°	0.624	$G_E^s + 0.517 G_M^s = 0.003 \pm 0.014$
A4_Forward	35°	0.230	$G_E^s + 0.224 G_M^s = 0.020 \pm 0.033$
	35°	0.108	$G_E^s + 0.106 G_M^s = 0.071 \pm 0.036$
A4_backward	145°	0.220	$G_E^s = 0.050 \pm 0.042$ $G_M^s = -0.14 \pm 0.16$
G0_forward	$\approx 60°$–$\approx 75°$	0.12–1	see fig. 12
G0_backward	108°	0.221 and 0.628	see fig. 15

with $G_E^{\gamma T=0} = \frac{(G_E^{\gamma p} + G_E^{\gamma n})}{2}$ is the isospin-zero electric form factor. Knowing $G_E^{\gamma T=0}$ from other experiments eq. (28), that is valid at the Q^2 values where meson-exchange current contributions are negligible [15], allows the measurement of G_E^s not in combination with G_M^s as in eq. (20).

Several experiments, at different Q^2 values, different electron beam parameters and different experimental apparatuses were performed in the past to measure the contributions of strange quarks to the ground-state charge and magnetization distributions of the proton. Table III summarizes their kinematic settings and their results.

The experiments of the SAMPLE series (SAMPLE, SAMPLE-II and SAMPLE-III) were performed at the MIT-Bates Linear Accelerator Center. They measured the Parity

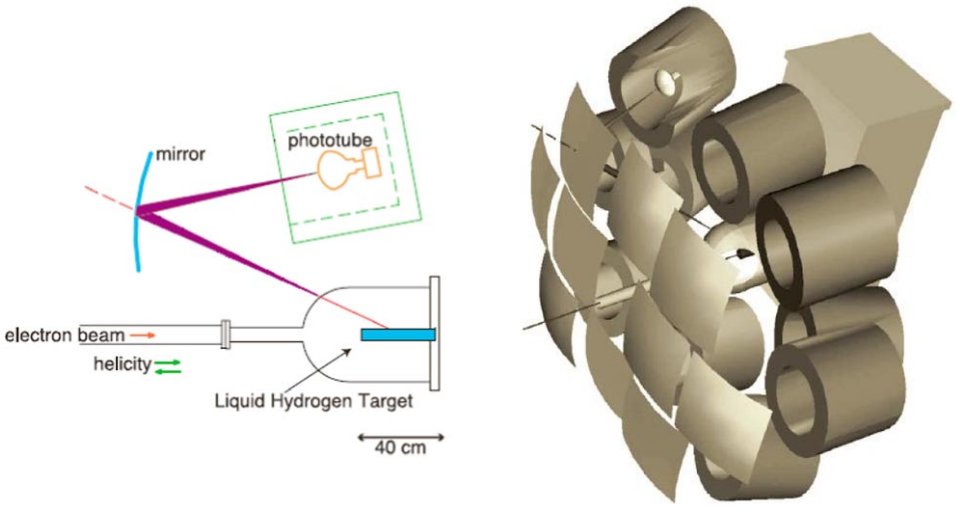

Fig. 2. – Left (from ref. [16]): the experimental principle of the experiments of the SAMPLE series: the electrons, scattered by the target, were detected in a large solid angle air Čerenkov detector covering angles between 130° and 170°. All backward-scattered electrons with energies above 20 MeV traveled faster than the speed of light in air and generated Čerenkov light that was focused onto a photomultiplier tube by an ellipsoidal mirror. The integrated photomultiplier current was proportional to the scattered electron rate. Right (from ref. [17]): schematic of the SAMPLE apparatus. Portions of the scattering chamber and lead shielding have been cut away for clarity.

Violating asymmetry in the elastic *e-p* (SAMPLE) and quasielastic *e-d* (SAMPLE-II and SAMPLE-III) scattering through the detection of the Čerenkov light produced in a large solid angle ($\sim 1.5\,\mathrm{sr}$) air Čerenkov detector by backward-scattered electrons. The detector (see fig. 2) covered the angular region $130° < \theta < 170°$ and the average electron scattering angle was $\theta = 146.1°$. The Čerenkov light was detected by an array of ten photomultiplier tubes after reflection from ellipsoidal mirrors.

The beam current was $40\,\mu$A and the beam polarization was $34.8 \pm 1.5\%$ (SAMPLE) $35.7 \pm 1.4\%$ (SAMPLE-II) and $38.9 \pm 1.6\%$ (SAMPLE-III). Four lucite Čerenkov counters (luminosity monitors) downstream of the target at the forward angles ($\sim 12°$) detected low-Q^2 scattering which has negligible Parity Violating asymmetry, thus serving as monitors for false asymmetries. A remotely controlled light shutter could cover each photomultiplier tube for background measurements. In the experiment SAMPLE-III an additional measurement of the shutter closed asymmetry was made with a plate of plastic scintillator placed in front of each PMT to enhance the statistics. The main source of background in the experiment was soft electromagnetic (bremsstrahlung) radiation (a thin Pb shield eliminated it) and arose from showering in the target plus additional scattering from downstream of the apparatus. Another source of background was the scintillation light due to the interaction of the residual flux of X-rays and low-energy gamma rays from the target with the air in the detector. This background, that generates events with only one photoelectron, was determined at low beam intensity with conventional pulse counting (instead of integrating) techniques and in runs performed covering the mirrors. Electromagnetic background generated by soft bremsstrahlung

and background from scintillation had negligible helicity dependence (the Parity Violating asymmetry is proportional to the squared momentum transfer to the proton). A third source of background was due to pions generated close to the production threshold. The pion production has a negligible Parity Violating asymmetry but contributed to the detector yield through decay products. The π^0 and π^+ yields and generated background were calculated through Monte Carlo simulations, that in the case of π^+ yield, where consistent with the measurement of the rate of delayed signals from muon decays. Monte Carlo simulations were performed also in order to take in account the electron energy loss due to ionization and collisions in the aluminum entrance window to the target, and in the thickness of liquid hydrogen upstream of the interaction point. The experiment SAMPLE [18-20] used a 40 cm liquid-hydrogen target and an electron beam of 200 MeV. The average Q^2 value was 0.1 $(\mathrm{GeV/c})^2$. At the backward-angle kinematics of the SAMPLE experiment, the *e-p* asymmetry (20) is dominated by the contribution from the magnetic neutral weak form factor, G_M^Z. For the SAMPLE experiment, as established by Monte Carlo simulations performed to determine the appropriate theoretical asymmetry to which the data should be compared and by averaging over detector and target length acceptance effects, eq. (20) is expressed by the formula

$$A(Q^2 = 0.1) = -5.56 + 3.37 G_M^s + 1.54 G_A^{e(T=1)} \text{ ppm}, \tag{29}$$

where $G_A^{e(T=1)}$ is the isovector nucleon axial form factor (see the term $-(1+R_A^{T=1})G_A\tau_3$ in eq. (25)). To obtain (29), the small isoscalar component of G_A^e has been absorbed into the first term, and dipole form factors for $G_{E,M}^p$ and G_M^n and the Galster parametrization [21] for G_E^n were used.

The measured asymmetry was equal to

$$A(Q^2 = 0.1) = -5.61 \pm 0.67 \text{ (stat)} \pm 0.88 \text{ (syst) ppm}, \tag{30}$$

where the first error is statistical and the second error is systematic.

To determine G_M^s from (29) and (30) the theoretical expectation of

$$G_A^{e(T=1)} = -0.83 \pm 0.26 \tag{31}$$

[22] was used. This because the computation of $G_A^{e(T=1)}$ in [22] predicted values of Parity Violating asymmetries in electron scattering on deuterium that agreed with the measurements performed by the SAMPLE-II and SAMPLE-III experiments with a D_2 target (see below, the electron scattering on deuterium is relatively insensitive to the strange vector matrix elements, but provides information about the nucleons neutral weak axial form factor as seen by an electron probe).

From (29), (30) and (31) a value

$$G_M^s(Q^2 = 0.1) = 0.37 \pm 0.20 \text{ (stat)} \pm 0.26 \text{ (syst)} \pm 0.07 \text{ (Elec. Rad. Corr.)} \tag{32}$$

(where the third error is the uncertainty due to electroweak radiative corrections) was obtained.

The experiment SAMPLE-II [16] was identical to the experiment SAMPLE with the exception of the use of a 40 cm long deuterium target instead of the hydrogen target used in SAMPLE, and of the installation of a borated polyethylene shielding around the

target to reduce background from low-energy neutrons knocked out of the deuterium, that were an additional source of background with respect to the experiment SAMPLE. The electron beam energy was 200 MeV. The average Q^2 value was 0.091 $(\mathrm{GeV/c})^2$. SAMPLE-II measured the asymmetry (26) in quasielastic scattering from deuterium at the same SAMPLE kinematics, where the axial term contributes approximately the same amount to the asymmetry as in the proton, but the contribution from the term proportional to G_M^s is greatly reduced because the proton and neutron contributions add incoherently and nearly cancel. The measured asymmetry was [23]

$$A(Q^2 = 0.091) = -7.77 \pm 0.73 \text{ (stat)} \pm 0.62 \text{ (syst) ppm}, \tag{33}$$

where the first error is statistical and the second error is systematic.

Because of the lack of energy resolution of the SAMPLE detector for the scattered electrons, this measured asymmetry contained contributions not only from quasielastic scattering but also from elastic scattering and threshold breakup. In order to construct the theoretical expression of the asymmetry as a function of G_M^s and G_A^e, a full nuclear calculation according to ref. [24] to obtain the parity-conserving and parity-violating response functions for the total inelastic processes (quasielastic scattering and threshold breakup) for selected kinematics was performed, explicitly keeping track of the dependence on G_M^s and G_A^e and including electroweak radiative corrections. In particular, the isoscalar axial radiative correction was taken to be $R_A^0 = \sqrt{3} R_A^{T=0} G_A^8 = 0.03 \pm 0.05$. The Parity Violating asymmetry was computed on an event-by-event basis through simulations performed with the Monte Carlo GEANT, separately for the elastic (from ref. [25]) and inelastic (using the above obtained response functions) processes. The resulting asymmetry distributions represented an average over the detector acceptance and incident electron energies. The physics asymmetry was then computed as a combined average of the elastic and inelastic distributions weighted by the appropriate cross-sections. The resulting theoretical asymmetry (in ppm) was [23]

$$A(Q^2 = 0.091) = -7.06 + 0.77 G_M^s + 1.66 G_A^{e(T=1)} \text{ ppm}, \tag{34}$$

where the small isoscalar component of G_A^e is absorbed into the first term. The dependence on the nuclear model of this result is small. From the experiments SAMPLE and SAMPLE-II the following values of G_M^s and $G_A^{e(T=1)}$ were derived:

$$G_M^s = 0.23 \pm 0.36 \pm 0.40; \qquad G_A^{e(T=1)} = -0.53 \pm 0.57 \pm 0.50. \tag{35}$$

The experiment SAMPLE-III [23] was identical to SAMPLE-II with the exception of the electron beam energy (125 MeV) and the average Q^2 value (0.038 $(\mathrm{GeV/c})^2$). The measured asymmetry was

$$A = -3.51 \pm 0.57 \text{ (stat)} \pm 0.58 \text{ (syst) ppm}. \tag{36}$$

With the same procedure described above for the experiment SAMPLE-II, the resulting theoretical asymmetry was

$$A(Q^2 = 0.038) = -2.14 + 0.27 G_M^s + 0.76 G_A^{e(T=1)} \text{ ppm}. \tag{37}$$

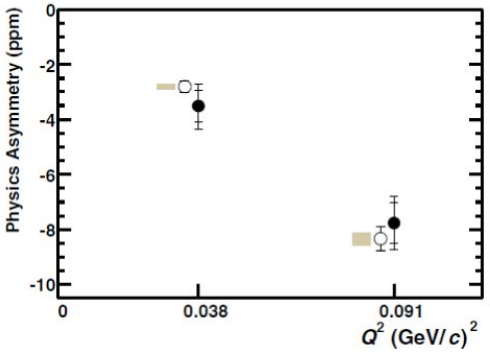

Fig. 3. – From ref. [23]. The physics asymmetries measured in SAMPLE-II and SAMPLE-III plotted as a function of Q^2 (solid circles). Also plotted (with offset Q^2 for visibility) are the theoretical predictions with the value of G_A^e taken from ref. [22], and $G_M^s = 0.15$ (open circles). The height of the gray rectangles represents the change in the physics asymmetry corresponding to a 0.6 change in G_M^s.

The asymmetries (33) and (36) are shown in fig. 3 together with the theoretical predictions with the values of $G_A^e(Q^2 = 0.038) = -0.91 \pm 0.28$ and $G_A^e(Q^2 = 0.091) = -0.84 \pm 0.26$ from ref. [22] and $G_M^s = 0.15$. Theoretical predictions and measured asymmetries agree within the uncertainties.

The series of experiments HAPPEX (see fig. 4) measured the contributions of strange form factors in the nucleon using the beam of the CEBAF accelerator at Jefferson Lab (JLab). The first HAPPEX experiment [27,28] measured the Parity Violating asymmetry in two runs performed in 1998 and 1999, respectively. 3.2 GeV electrons were scattered from a 15 cm long unpolarized liquid-hydrogen target at a scattering angle $\theta_{\rm lab} = 12.3°$. The average Q^2 value was 0.477 $(\mathrm{GeV/c})^2$. The elastically scattered electrons were focused by two High Resolution Spectrometers (HRS) onto detectors consisting of lead-lucite sandwich calorimeters. The HRS pair had sufficient resolution to spatially separate the elastic electrons from inelastic electrons at the π^0 threshold. In the 1998 run, where a bulk GaAs photocathode was used, the electron beam intensity was 100 μA and the beam polarization was equal to $\sim 38\%$. In 1999 run, a strained GaAs photocathode was used that produced a 35 μA electron beam with a polarization of $\sim 70\%$.

The measured asymmetry, multiplied by a factor that converted the measured acceptance (Q^2) averaged asymmetry to the asymmetry from point scattering at the effective kinematics ($Q^2 = 0.477$ $(\mathrm{GeV/c})^2$ was

$$A = -15.05 \pm 0.98\ (\mathrm{stat}) \pm 0.56\ (\mathrm{syst})\ \mathrm{ppm}. \tag{38}$$

From (38) and (20), assuming for G_A^{Zp} the value derived by [22] that produces an asymmetry equal to 0.56 ± 0.23 ppm, for $G_M^{\gamma p}/(\mu_p G_D)$ the value 0.9934 (G_D being the dipole form factor $= [1 + Q^2/0.71\ (\mathrm{GeV/c})^2]^{-2}$), for $G_E^{\gamma p}$ the value $0.98 \times G_M^{\gamma p}/\mu_p$, for $G_E^{\gamma n}$ the value $0.161 \times G_M^{\gamma p}/\mu_p$ and for $G_M^{\gamma n}$ the value $1.004 \times G_M^{\gamma p}\mu_n/\mu_p$ (μ_p and μ_n the proton and neutron magnetic moments) the value

$$G_E^s + \beta G_M^s = 0.014 \pm 0.020\ (\mathrm{exp}) \pm 0.010\ (\mathrm{FF}) \tag{39}$$

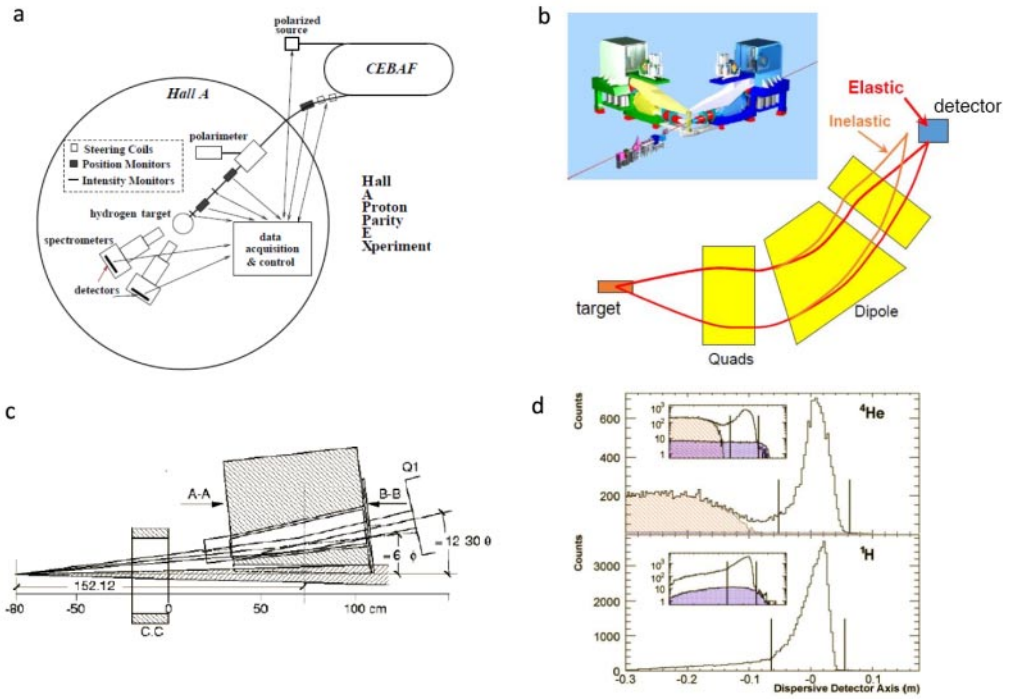

Fig. 4. – a) (from ref. [4]). Schematic Overview of the HAPPEX Experiment. b) The experimental principle of the experiments of the HAPPEX series: the electrons, scattered by the target, were detected in the two nearly identical focusing High Resolution Spectrometers (HRS). The HRS pair had sufficient resolution to spatially separate the elastic electrons from inelastic electrons at the π^0 threshold. c) During the experiment HAPPEX-II, two septum magnets were added to HRS spectrometers, which were not able to detect particle scattered at angles less than 12.5°, in order to make them able to accept very forward scattered electrons with $\langle\theta_{\rm lab}\rangle = 6°$. d) (from ref. [26]) Single-particle spectra obtained in dedicated low-current runs during the experiment HAPPEX-II. The insets show the same spectra on a logarithmic scale. The vertical lines delineate the extent of the detectors. Inelastic scattering from ^{4}He is entirely contained in the hatched area. The shaded regions, visible only in the log plots, show the contribution from target windows.

with $\beta = \frac{\tau G_M^{\gamma p}}{\epsilon G_E^{\gamma p}} = 0.392$, was obtained. In (39) the first error is the total experimental error (statistical and systematic errors added in quadrature) and the second error is the error due to the ordinary electromagnetic form factors and is dominated by $G_M^{\gamma n}$

The experiment HAPPEX-II was very similar to the 1999 first HAPPEX experiment with the exception of a higher beam polarization (75-85%) and the addition of septum magnets to HRS spectrometers to make them able to accept very forward scattered electrons with $\langle\theta_{\rm lab}\rangle = 6°$. Radiation-hard focal plane detectors which could survive the increased scattered electron rate were introduced.

Two targets were used in the HAPPEX-II experiment: a 20 cm long liquid-hydrogen target [29] and a 20 cm long cryogenic high-pressure ^{4}He gas target [30]. Two runs were performed. With the hydrogen target, the asymmetry, after correction for beam polarization, backgrounds (mainly due to quasielastic scattering from the aluminum windows of

the target), and finite acceptance was equal for the first run ($Q^2 = 0.099$ (GeV/c)^2) [29] to

$$A = -1.14 \pm 0.24 \text{ (stat)} \pm 0.06 \text{ (syst) ppm.} \tag{40}$$

Assuming at $Q^2 \sim 0.1$ (GeV/c)^2 the following values for the electromagnetic form factors: $G_E^{\gamma p} = 0.754$ ($\pm 2.5\%$), $G_M^{\gamma p} = 2.144\,(\pm 1.5\%)$, $G_E^{\gamma n} = 0.035$ ($\pm 30\%$), and $G_M^{\gamma n} = -1.447$ ($\pm 1.5\%$) (all values derived by a phenomenological fit to world data at low Q^2 [31]) and evaluating the contribution to the asymmetry from axial form factor (assumed to be a dipole form) at HAPPEX-II first run kinematics to be equal to -0.026 ± 0.008 ppm, the following value was obtained:

$$G_E^s + 0.080 G_M^s = 0.030 \pm 0.025 \text{ (stat)} \pm 0.006 \text{ (syst)} \pm 0.012 \text{ (FF)}, \tag{41}$$

where the third error is due to the uncertainties on form factors, mainly $G_E^{\gamma n}$.

For HAPPEX-II second run ($Q^2 = 0.109$ (GeV/c)^2) the asymmetry mesasured was [26]

$$A = -1.58 \pm 0.12 \text{ (stat)} \pm 0.04 \text{ (syst) ppm.} \tag{42}$$

Assuming now a value for the neutron electric form factor $G_E^{\gamma n} = 0.037$ ($\pm 10\%$) derived from data from the BLAST experiment [32,33]), and evaluating the contribution to the asymmetry from axial form factor at HAPPEX-II second run kinematics be equal to -0.037 ± 0.018 ppm [22], the following value was obtained (at $Q^2 = 0.109$ (GeV/c)^2):

$$G_E^s + 0.09 G_M^s = 0.007 \pm 0.011 \text{ (stat)} \pm 0.004 \text{ (syst)} \pm 0.005 \text{ (FF)}. \tag{43}$$

With the helium target, the asymmetry, after the usual corrections for beam polarization, background, and finite acceptance, was equal for the first run ($Q^2 = 0.091$ (GeV/c)^2) [30] to

$$A = 6.72 \pm 0.84 \text{ (stat)} \pm 0.21 \text{ (syst) ppm,} \tag{44}$$

with a consequent value for G_E^s, derived from (28), of

$$G_E^s = -0.038 \pm 0.042 \text{ (stat)} \pm 0.010 \text{ (syst)}, \tag{45}$$

while for the second run ($Q^2 = 0.077$ (GeV/c)^2) [26] a value

$$A = 6.40 \pm 0.23 \text{ (stat)} \pm 0.12 \text{ (syst) ppm} \tag{46}$$

for the asymmetry was obtained with a consequent value for G_E^s of

$$G_E^s = 0.002 \pm 0.014 \text{ (stat)} \pm 0.007 \text{ (syst)}. \tag{47}$$

In deriving (45) and (47), the value of $G_E^{\gamma T=0}$ was derived by the phenomenological fit to the world data at low Q^2 already used for deriving (41) and (43) [31].

Assuming in the range $0.077 \leq Q^2 \leq 0.109$ (GeV/c)^2 $G_E^s \propto Q^2$ and G_M^s constant, extrapolating the results (41), (43), (45) and (47) to $Q^2 = 0.1$ (GeV/c)^2, the results shown

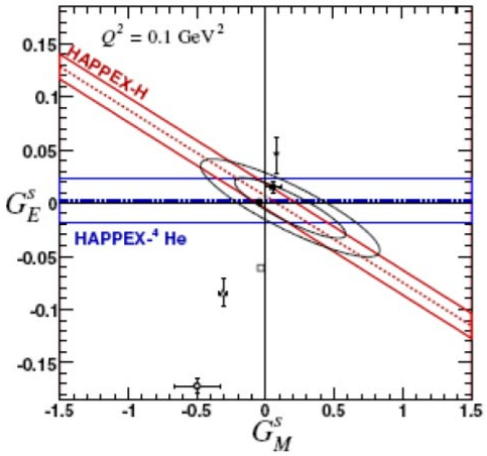

Fig. 5. – Adapted from ref. [26]. 68 and 95% C.L. constraints in the G_E^s and G_M^s plane from HAPPEX-II data. Various theoretical predictions are plotted with published uncertainty estimates: ref. [34] (empty square), ref. [35] (empty triangle), ref. [36] (empty circle), ref. [37](filled triangle), ref. [38] (filled square) and ref. [39] (filled circle).

in fig. 5 were obtained that correspond to the following values at $Q^2 = 0.1$ (GeV/c)^2 for the strange form factors

$$G_E^s = -0.005 \pm 0.019; \qquad G_M^s = 0.18 \pm 0.27 \tag{48}$$

(correlation coefficient $= -0.87$).

The result of (48), consistent with null strange form factors, is quite insensitive to variations in the axial form factor.

The HAPPEX-III experiment [40] was very similar to the other HAPPEX experiments: a 100 μA continuous electron beam of longitudinally polarized electrons at 3.481 GeV was incident on a 25 cm long liquid-hydrogen target. The experimental apparatus and techniques did not change substantially with respect to the other HAPPEX experiments. The elastically scattered electrons were detected at $\langle\theta_{\rm lab}\rangle = 13.7^\circ$ and the average Q^2 was 0.624 (GeV/c)^2.

The asymmetry measured was

$$A = -23.80 \pm 0.78 \text{ (stat)} \pm 0.36 \text{ (syst) ppm} \tag{49}$$

that, after parametrizations of the electromagnetic form factors which incorporate two photon exchange corrections to published form factor data [41] and standard electroweak corrections [42], gave the result

$$G_E^s + 0.517 G_M^s = 0.003 \pm 0.010 \text{ (stat)} \pm 0.004 \text{ (syst)} \pm 0.009 \text{ (theor)}, \tag{50}$$

where the last error comes from the theoretical uncertainties on the value of the asymmetry for zero contribution of the strange form factors due to uncertainties in the electromagnetic form factors and in radiative corrections in the axial term of the asymmetry (20)

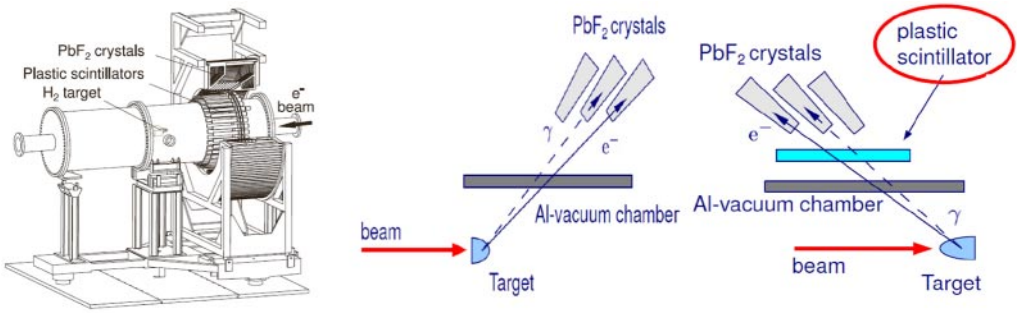

Fig. 6. – a) (from ref. [43]). Drawing of the PbF_2 calorimeter of the experiment A4. The system is mounted on a rotatable platform. b) and c) The principle of the experiment A4. The beam electrons were scattered by the target and detected by the total absorption calorimeter of lead fluoride crystals. With respect to the forward mode (b), in backward mode (c) scintillators were placed between the scattering chamber and the lead fluoride crystals. The coincidence between the scintillators and the calorimeter allowed the separation between charged from neutral particles and hence to distinguish between scattered electrons and photons from π^0 decay.

involving Parity Violating multiquark interactions. The importance of the latter are, however, reduced for forward-angle kinematics as in HAPPEX-III.

The experiment A4 (see fig. 6) took place at the Mainzer Mikrotron accelerator facility (MAMI). It measured the asymmetry (20) at $Q^2 = 0.108$ [44] and at $Q^2 = 0.230$ $(\mathrm{GeV/c})^2$ [45] at forward electron scattering angles ($30^\circ < \theta_e < 40^\circ$), and at $Q^2 = 0.22$ $(\mathrm{GeV/c})^2$ at backward electron scattering angles ($140^\circ < \theta_e < 150^\circ$) [43].

Its systematic uncertainties were of a different nature with respect to the ones of the experiments of the series SAMPLE and HAPPEX because, differently from these experiments, it used counting and not analogue integrating measuring techniques. When detecting scattered electrons at forward angles, the primary electron beam had an intensity of 20 μA, a polarization of about 80%, and an energy of 570.4 MeV (for the measurement at $Q^2 = 0.108$ $(\mathrm{GeV/c})^2$), and of 854.3 MeV (for the measurement at $Q^2 = 0.230$ $(\mathrm{GeV/c})^2$). For the measurement with electrons scattered at backward angles the energy of the primary beam was 315.1 MeV, its intensity was 20 μA and its polarization was about 70%. The helicity of the beam was selected with a frequency of 20 ms. 10 and 23.4 cm liquid-hydrogen targets were used for the measurements at forward and backward electron scattering angles, respectively. The target density for each beam helicity state was determined measuring, for each 20 ms time window in which the beam helicity was fixed, the response of eight water Čerenkov detectors that detected scattered particles symmetrically around the electron beam for small scattering angles in the range of 4°–10°, where the Parity Violating asymmetry is negligible. The scattered electrons were detected, in the scattering angle range, by a total absorption calorimeter consisting of 1022 individual lead fluoride (PbF_2) crystals, arranged in 146 rows and 7 rings. In the measurement at $Q^2 = 0.230$ $(\mathrm{GeV/c})^2$ at forward electron scattering angles, only half of the crystal were operational and the detector modules were located in two sectors, covering an azimuthal angle interval $\Delta\Phi$ of $\sim 90^\circ$ symmetrically around the beam axis. The signals from each cluster of nine crystals were summed and integrated for 20 ns. The number of elastically scattered electrons for each helicity state was determined by summing over the inner 345 detector channels, which were the centers of a full 3×3

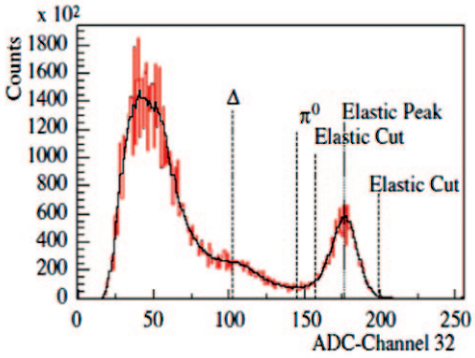

Fig. 7. – From ref. [45]. Raw energy spectrum of accepted particles from the hydrogen target as read directly from the hardware memory of the readout electronics of the lead fluoride calorimeter used in the A4 experiment when detecting forward-angle scattered particles (dashed histogram). The solid black curve shows the raw spectrum corrected for the differential nonlinearity of the ADC. The lower and the upper cut positions for the extraction of the number of elastically scattered electrons are shown.

crystal matrix. In the other measurements all the crystals were operational and the detector covered the full azimuthal range. The number of elastically scattered electrons for each helicity state was in these cases determined summing up over all 730 channels of the inner five rings of the calorimeter. The detected particle energy resolution was $\frac{3.9\%}{\sqrt{E}}$ with E the particle energy. A typical energy spectrum for forward electron scattering angle measurements is shown in fig. 7, which shows that the elastic scattering peak is clearly isolated at the high end of the spectrum. The number of elastic scattered electrons was determined for each detector channel by integrating the number of events in the interval corresponding to the elastic peak in each helicity histogram. At forward electron scattering angles the background from produced π^0 was estimated negligible through Monte Carlo simulations. The largest background source were electrons from quasielastic scattering at the thin aluminum entrance and exit windows of the target cell. In the measurement at backward electron scattering angles 72 plastic scintillators in front of the PbF_2 crystals were added to the apparatus to be used in coincidence with the calorimeter in order to separate charged from neutral particles and hence distinguish between scattered electrons and photons from π^0 decay. For this measurement a not negligible background was caused by high-energy photons converting into e^+e^- pairs in the aluminum wall of the vacuum chamber and in the scintillator. The contribution to the asymmetry of this background was measured through non-coincidence detector spectra and was eliminated scaling these spectra with the conversion probability of a γ to convert and trigger the scintillator and shifting them by the energy loss of the generated e^+e^- pairs as evaluated through Monte Carlo simulations. The same procedure was used to eliminate the contribution to the background arising from aluminum events from the target entrance and exit windows, that was determined by a measurement with an empty target and was about 4.5%. Figure 8 shows the measured energy spectra at backward electron scattering angles and the contributions from the different processes.

The measured asymmetries were the following: at $Q^2 = 0.108$ (GeV/c)^2 the measured asymmetry was

$$A = -1.36 \pm 0.29 \text{ (stat)} \pm 0.13 \text{ (syst) ppm}, \tag{51}$$

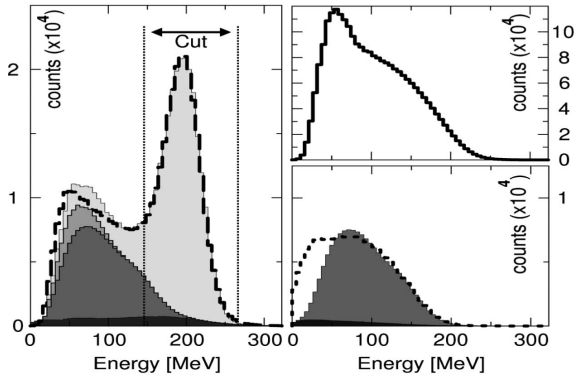

Fig. 8. – From ref. [43]. Detector response in the A4 experiment when detecting backward scattered electrons. Left panel: the measured energy spectrum of coincidence events (dashed line). The peak of the elastic scattered electrons is clearly identified. The contributions of the different processes are shown from bright to dark: i) the elastically scattered electrons, ii) the inelastically scattered electrons, iii) the converted photons from π^0 decay, and iv) empty target background. Upper right panel: a measured energy spectrum of non-coincidence events. Lower right panel: the dotted line shows the background contribution to the coincidence spectrum estimated from the non-coincidence events by applying the shifting and scaling method in comparison with the photon background obtained from the simulation (gray) together with the shifted and scaled non-coincidence events from an empty target measurement (dark).

which corresponded, after calculating the difference between this value and the theoretical prediction in the framework of the Standard Model with the form factors $G_{E,M}^{p,n}$ given by the parameterization of ref. [31], assuming an experimental error of 3% to G_E^p and G_M^p, 5% to G_M^n and 10% to G_E^n, to a value of

$$G_E^s + 0.106 G_M^s = 0.071 \pm 0.036. \tag{52}$$

At $Q^2 = 0.230$ (GeV/c)^2 (forward electron scattering angles) the measured asymmetry was

$$A = -5.44 \pm 0.54 \text{ (stat)} \pm 0.26 \text{ (syst) ppm} \tag{53}$$

that, after calculating the difference between this value and the theoretical prediction in the framework of the Standard Model, taking the electromagnetic form factors $G_{E,M}^{p,n}$ from a Monte Carlo based analysis of the world data [46], corresponded to a value of

$$G_E^s + 0.224 G_M^s = 0.020 \pm 0.029 \text{ (exp)} \pm 0.016 \text{ (FF)}, \tag{54}$$

where the first error comes from the measurement and the second from the uncertainty in the axial and electromagnetic form factors of the nucleon.

At $Q^2 = 0.220$ (GeV/c)^2 (backward electron scattering angles), the measured asymmetry was

$$A = -17.23 \pm 0.82 \text{ (stat)} \pm 0.89 \text{ (syst) ppm} \tag{55}$$

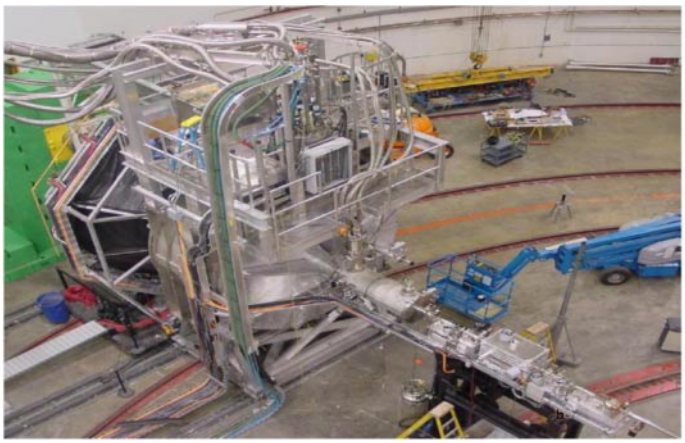

Fig. 9. – From ref. [47]. A view of G0 experimental set up in the forward configuration. The electron beam travels from lower right to upper left. The superconducting magnet is seen just to the left of the center of the frame; the target is centered inside the magnet.

from which, following the same procedure utilized to derive eq. (54) from eq. (53), the following expression was derived:

$$G_M^s + 0.26 G_E^s = -0.12 \pm 0.11\ (\text{exp}) \pm 0.11\ (\text{FF}). \tag{56}$$

Combining forward and backward electron scattering measurements at $Q^2 \sim 0.23$ $(\text{GeV/c})^2$, the following values were obtained:

$$G_E^s = 0.050 \pm 0.038\ (\text{exp}) \pm 0.019\ (\text{FF}); \tag{57}$$

$$G_M^s = -0.14 \pm 0.11\ (\text{exp}) \pm 0.11\ (\text{FF}). \tag{58}$$

Data from the experiment A4 are waited for measurements at $Q^2 = 0.23$ $(\text{GeV/c})^2$, performed at backward electron scattering angles with a deuterium target, at $Q^2 = 0.62$ $(\text{GeV/c})^2$, performed at forward electron scattering angles with an hydrogen target and at $Q^2 = 0.1$ $(\text{GeV/c})^2$, performed at backward electron scattering angles both with an hydrogen target and a deuterium target.

The experiment G0 [47] took place in Hall C of JLAB. It used a superconducting toroidal magnet that focused scattered particles through collimators onto a focal plane array of scintillators. The magnet contained eight superconducting coils splitting the magnet and detector system into octants. Each octant, as defined by collimators near the cryogenic target, accepted 20° in azimuthal angle. Combined with the polar angle acceptance, defined by the momentum defining collimators, the device had a total solid angle of about 0.9 sr. The experiment operated in two running modes: "forward mode" and "backward mode". In its forward mode (see fig. 9 and fig. 10), the apparatus detected and counted recoiling protons from forward-angle electron scattering. The protons were ejected at angles between $\sim 60°$ and $\sim 75°$ and a simultaneous measurement for all Q^2 values (0.12–1.0 $(\text{GeV/c})^2$) was made. For a given Q^2 the magnet focused protons from any point along the target length, at least at the center of each octant. The Focal Plane Detectors (FPD) for each octant consisted of 16 pairs of scintillation detectors, placed

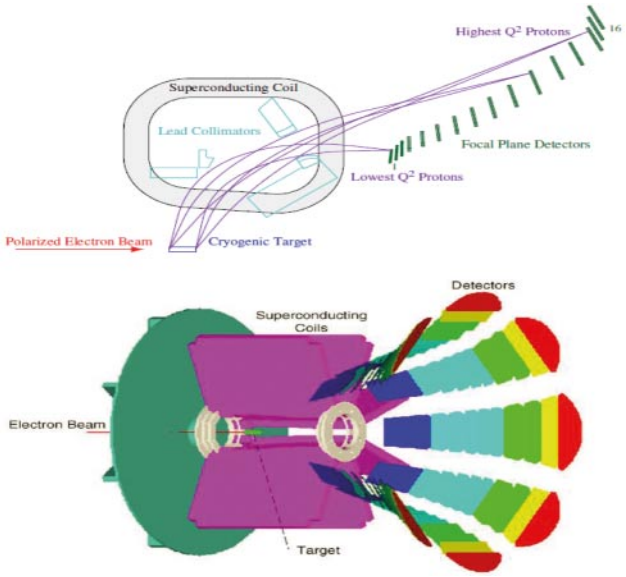

Fig. 10. – The principle of the experiment G0 in forward mode. Top: from ref. [47]. Protons of the same Q^2 originating from any location in the target were focused to a common detector. The highest Q^2 protons appeared in FPD14 (see text for details). A superconducting coil outline and one octant of collimators, line-of-sight shielding, and focal plane detectors are pictured. Bottom: from ref. [17]. Schematic of the G0 apparatus used in the forward configuration. Each detector color corresponds to a different value of momentum transfer Q^2, ranging from 0.12 to 1 $(\mathrm{GeV/c})^2$.

at, or near, the focal plane of the magnet and shaped and segmented to detect protons corresponding to a limited band of Q^2 and to limit the e-p elastic count rate to less than approximately 750 kHz. FPD 1-14 (smallest detector number corresponding to the lowest momentum transfer) accepted relatively narrow bands of Q^2, whereas FPD 15 accepted a broad band of Q^2 at the end of the range of acceptance ($0.44 \leq Q^2 \leq 0.88$ $(\mathrm{GeV/c})^2$). No elastic scattering events were recorded by FPD 16, and it was used as a monitor of background and magnet current. The use of pairs of scintillators suppressed the background from neutral particles. To separate elastic protons from inelastic protons and pions the flight time of the particles detected was measured using a signal associated with the beam arrival on target. A typical Time-Of-Flight spectrum is shown in fig. 11. Elastic protons arrived about 20 ns after the passage of the electron bunch through the target. The large range of momentum transfers accepted by FPD 15 was divided into three Time-Of-Flight bins with average momentum transfers of 0.51, 0.63, and 0.79 $(\mathrm{GeV/c})^2$. FPD 14 had two elastic peaks separated in TOF with momentum transfers of 0.41 and 1.0 $(\mathrm{GeV/c})^2$.

In "forward mode" an electron beam of 40 μA and 3.031 ± 0.001 GeV and a 20 cm liquid-hydrogen target were employed. The beam polarization was $73.7 \pm 1.0\%$. Beside the "usual" corrections for helicity-correlated beam current, position, angle, and energy, a further correction was needed because a small ($\sim 10^{-3}$) fraction of the beam current with a 2 ns structure existed due to tails of beams from the other operating halls at JLab (the beam requested by G0 had a 32 ns structure to allow Time-Of-Flight measurements). The

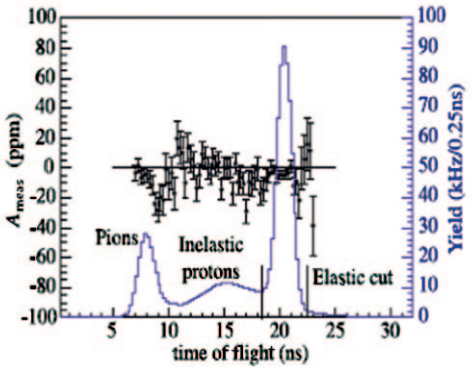

Fig. 11. – From ref. [48]. Example of the raw asymmetry, $A_{\rm meas}$ (data points), and yield (histogram) as a function of TOF for detector 8 of the experiment G0 in "forward mode".

fraction of the beam current with a 2 ns structure was measured in otherwise forbidden regions of the Time-Of-Flight spectra and the correction applied to take into account it was of the order of 0.71 ± 0.14 ppm on average to the asymmetries in all detectors ($\sim 5\%$ variation from detector to detector). Great care was employed to take into account the background generated by quasielastic protons from the aluminum target windows and inelastic protons from both the hydrogen and the aluminum. This background extended on both sides of the elastic proton peak in the Time-Of-Flight spectrum. To determine the contribution to the measured asymmetry of this background Time-Of-Flight fits to the yield and asymmetry in the region of the elastic peak were used. The yield was typically modeled with a Gaussian elastic peak and a polynomial background. The asymmetry model comprised a quadratic background and a constant for the elastic (see fig. 11). The uncertainties from the background correction dominated the systematic uncertainties. Figure 12 shows, as function of Q^2, the quantity

$$G_E^s + \eta G_M^s = \frac{4\sqrt{2}\pi\alpha}{G_F Q^2} \times \frac{\epsilon \left(G_E^{\gamma p}\right)^2 + \tau \left(G_M^{\gamma p}\right)^2}{\epsilon G_E^{\gamma p}} \times \left(A_{\rm Phys} - A_{\rm NS}\right), \tag{59}$$

with $\eta(Q^2) = \frac{\tau G_M^{\gamma p}}{\epsilon G_E^{\gamma p}}$ and $A_{\rm NS}$ the value calculated from eq. (20) with $G_E^s = G_M^s = 0$ for all values of Q^2, and using the electromagnetic form factors of Kelly [49]. The error bars include the statistical uncertainty (inner) and statistical plus point-to-point systematic uncertainties added in quadrature (outer). The error bands represent, for the G0 experiment, the global systematic uncertainties: from the measurement (upper) and from the uncertainties in the quantities entering $A_{\rm NS}$ (lower). These quantities are the calculated value of the axial-vector form factor normalization [22] (differing from $\frac{g_A}{g_V}$, the ratio of the axial-vector to vector weak coupling, by electroweak radiative corrections), the same dipole momentum transfer dependence for $G_A^e(Q^2)$ as is deduced for $G_A(Q^2)$ [50], the axial-vector strangeness contribution Δs [51], and the electroweak radiative corrections [13]. The sensitivity of the result to electromagnetic form factors is shown separately in the lower panel, where the effective $A_{\rm NS}$ is shown for the alternative form factor parameterizations of Friedrich and Walcher (FW) [31] (dashed line) and the combination Arrington Rosenbluth [52] proton, and Kelly [49] neutron (dotted

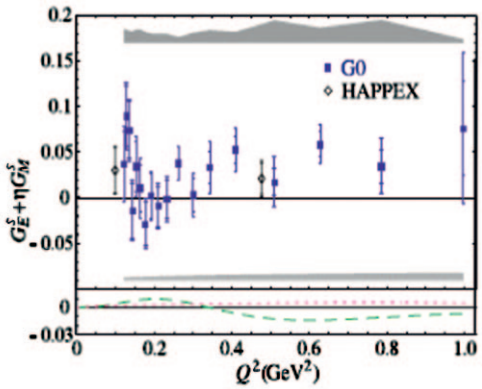

Fig. 12. – From ref. [48]. The combination $G_E^s + \eta G_M^s$ measured by the G0 experiment in "forward mode". The gray bands indicate systematic uncertainties (to be added in quadrature); the lines in the lower panel correspond to different electromagnetic nucleon form factor models. See text for details.

line). *E.g.*, for the FW parameterization, the value of $G_E^s + \eta G_M^s$ at $Q^2 = 0.63$ (GeV/c)^2 increases from 0.059 to 0.072. Alternately, the uncertainties in the Kelly form factor fits would increase the width of the uncertainty band (lower) for $A_{\rm NS}$ at each Q^2 by about 25% if included there. The agreement with the HAPPEX measurements made at nearly the same kinematic points (with small corrections to the asymmetries, less than 0.2 ppm, to adjust them to the G0 beam energy) was excellent. Combining the G0 result at $Q^2 = 0.23$ (GeV/c)^2 with the two measurements at $Q^2 \sim 0.23$ (GeV/c)^2 performed in the A4 experiment when detecting forward and backward scattered electrons respectively (see eq. (54), eq. (56), and eq. (57) above), the following value for G_E^s was obtained:

$$G_E^s = 0.035 \pm 0.030\ (\text{exp}) \pm 0.019\ (\text{FF}). \tag{60}$$

In backward mode [53] (see figs. 13 and 14) G0 operated with the magnet detector system rotated by 180°. In this mode the experiment detected scattered electrons and not recoil protons. The optics of the magnet were such that the scattered electrons were at an average angle of 108° ± 10°, corresponding to a single value of Q^2 for each beam energy. Therefore, measurements were performed with two different incident energies: 359 and 684 MeV corresponding to two different Q^2 values: 0.221 and 0.628 (GeV/c)^2. In backward mode each focal plane detector (FPD) collected both elastically and inelastically scattered electrons. To separate elastic and inelastic electrons, a second scintillator array (labeled the Cryostat Exit Detectors or CEDs) was mounted near the magnet cryostat exit window for each octant. The CED array consisted of 9 arch-shaped scintillators, similar in shape to the FPDs but smaller, since they lied closer to the target. By recording all possible combinations of coincidences between the 9 CEDs and 14 FPDs, elastic and inelastic events were separated (see fig. 14). The particle identification needed to distinguish electrons from pions was performed by an aerogel Čerenkov detector with a pion threshold of 570 MeV, used in coincidence with the scintillators.

The beam maximum intensity was 60 μA and the beam polarization was 85.8 ± 2.1(1.4)% at the lower (higher) incident energy. Two targets for two different goals were used: one 20 cm liquid-hydrogen target and one 20 cm deuterium target. Comparing

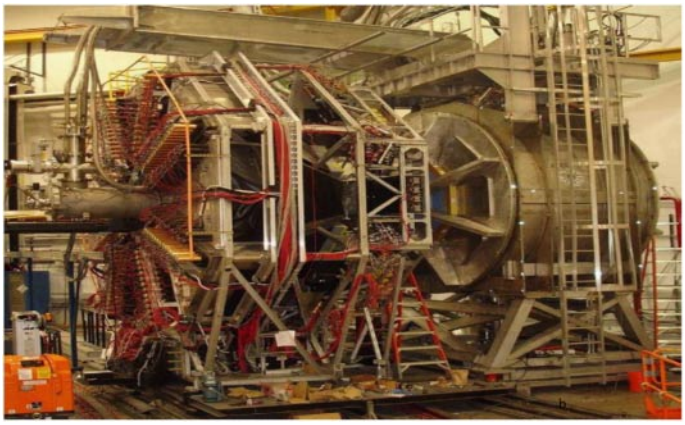

Fig. 13. – From ref. [47]. A view of G0 experimental set up in the backward configuration. The beam enters from the left. The superconducting magnet is on the right of the frame; the target is centered within it. The detector system is shown retracted from its normal position by about 1 m. The photomultiplier tubes for Octant 3 are closest to the camera on the left. Detector supports added for the backward measurement, holding the Čerenkov and cryostat exit detectors (CEDs) are visible just to the right of center.

the G0 results in "forward mode" with those of the G0 in "backward mode" with the liquid-hydrogen target, the measurements of the asymmetry (20) at two different angles were obtained. From these measurements it was possible to extract G_E^{Zp} and G_M^{Zp} and hence to determine separately the values of G_E^s and G_M^s. The measurement of the Parity Violating asymmetry in quasielastic scattering from the deuterium target provided

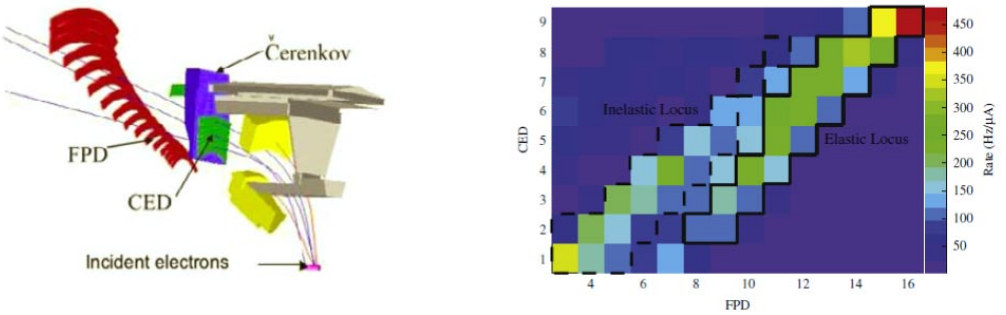

Fig. 14. – The principle of the experiment G0 in backward mode. Left (from ref. [54]): to separate elastic and inelastic electrons, a second array of scintillators, labeled CED, was added to FPD scintillators and mounted near the magnet cryostat exit window for each octant. By recording all possible combinations of coincidences between the CEDs and FPDs, elastic and inelastic events were separated. This is shown in the right part of the figure (from ref. [47]), which reports coincidence rates for the various combinations of CEDs and FPDs for backward angle measurement of scattered electrons from the LH2 target at 684 MeV incident energy. The elastically scattered electrons appear in a band toward the upper right, the inelastically scattered electrons in a band toward lower left. An aerogel Čerenkov detector with a pion threshold of 570 MeV, used in coincidence with the scintillators, provided the particle identification needed.

the third measurement needed to determine the effective axial form factor, G_A^e, using a complete model of the electroweak deuteron response [55]. G_A^e can be expressed as the sum of an isovector part ($G_A^{e,T=1}$) and an isoscalar part ($G_A^{e,T=0}$)

$$G_A^e = G_A^{e,T=1} + G_A^{e,T=0} = G_{A,\mathrm{cc}}^{(0)} + R_{\mathrm{ana}} + G_A^{e,T=0}, \tag{61}$$

with $G_{A,\mathrm{cc}}^{(0)}$ the axial form factor measured in charged current neutrino scattering [50, 56, 57] and R_{ana} the radiative correction. The experiment G0 focused above all in the determination of $G_A^{e,T=1}$.

In "backward mode" the background corrections were small because the background asymmetries generally have values close to those of the elastic asymmetry. With the exception of the run with the deuterium target at 684 MeV, the background was mainly generated in the aluminum target windows and its yield was measured in runs with gaseous hydrogen in the target. The aluminum asymmetry was assumed to be the same as that of the deuteron (both effectively quasielastic scattering only) with an additional uncertainty of 5% for nuclear effects. In the run with the deuterium target at 684 MeV, the main source of background were misidentified π^-. The measured asymmetries were corrected for the dead time, for the accidentals from pion signals in the scintillators in coincidence with random signals from the Čerenkov (especially high in the run with the deuterium target at 684 MeV), for electromagnetic radiative corrections [58], and for two boson exchange effects [59].

Figures 15a and b show the values of G_E^s and G_M^s obtained combining the results of the G0 experiment in "backward mode" with the corresponding values as determined by a linear fit of $A_{\mathrm{phys}} - A_{\mathrm{NS}}$ measurements of the G0 experiment in "forward mode" in the range $0.177 < Q^2 < 0.997$ (GeV/c)^2. In the fit the uncertainty of the interpolated values was assumed to be 70% of the statistical uncertainty at the nearest measured point. In extracting G_E^s and G_M^s from the measured asymmetries, the nucleon form factors of ref. [49] were used. For the determination of $G_A^{e,T=1}$ (fig. 15c) the isoscalar contributions to G_A^e were taken from refs. [22, 63]. The systematic uncertainties in the measurements of G_E^s, G_M^s and $G_A^{e,T=1}$ are due to uncertanties on incident energies, four-momentum transfers, electromagnetic form factors, deuteron model and electroweak radiative corrections.

Combining the results of HAPPEX-III and G0-forward and G0-backward experiments, the constraints on the 2D space spanned by G_E^s and G_M^s at Q^2 near 0.62 (GeV/c)^2 shown in fig. 16 are obtained. The experimental constraints at 1σ are represented by the shaded bands indicating the combined statistical and experimental systematic error bars. The contours, representing the 68% and 95% uncertainty boundaries as indicated, combine all three measurements and also account for the uncertainties in the value of the asymmetry for zero contribution of the strange form factors. The independently separated values resulting from this fit are

$$G_E^s = 0.047 \pm 0.034; \qquad G_M^s = -0.070 \pm 0.067, \tag{62}$$

with a correlation coefficient of -0.93. This result is consistent with $G_E^s = 0$ and $G_M^s = 0$.

Figure 17 shows all published data on the net strangeness contribution $G_E^s + \eta\, G_M^s$ in forward-angle scattering measurements from the proton *versus* Q^2. $\eta(Q^2) = \frac{\tau G_M^{\gamma p}}{\epsilon G_E^{\gamma p}}$ is approximately numerically equal to Q^2 (in (GeV/c)^2) over the range of the plot. On

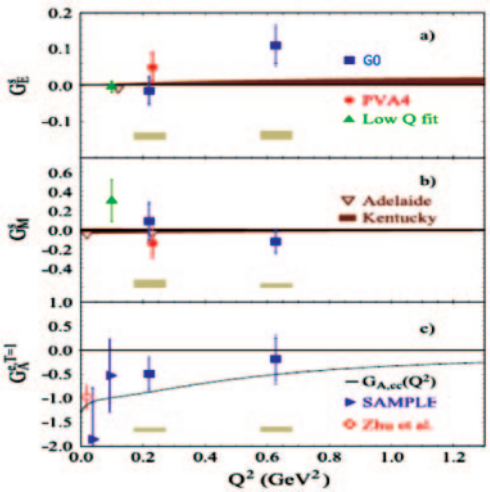

Fig. 15. – Adapted from ref. [53]. The form factors (a) G_E^s, (b) G_M^s and (c) $G_A^{e,T=1}$ determined by the G0 experiment forward- and backward-angle measurements. Error bars show statistical and statistical plus point-to-point systematic uncertainties (added in quadrature); shaded bars below the corresponding points show global systematic uncertainties (for G0 points). For G_E^s and G_M^s the extraction from ref. [60] as well as the results of the PVA4 experiment are shown. Calculations from Adelaide [61] and Kentucky [62] groups are also shown; for the former the uncertainties are smaller than the symbols. For $G_A^{e,T=1}$ results from the SAMPLE experiment together with the calculation of Zhu *et al.* [22] are shown.

each data point, the error bars indicate both the statistical error and the quadrature sum of statistical and uncorrelated systematic error. For the G0 data, some systematic uncertainties are correlated between points with a magnitude indicated by the shaded region at the bottom of the plot. A shaded region around the zero net strangeness line represents the uncertainties in $A_{\rm NS}$ at 1σ; this uncertainty is not also included in the individual data points.

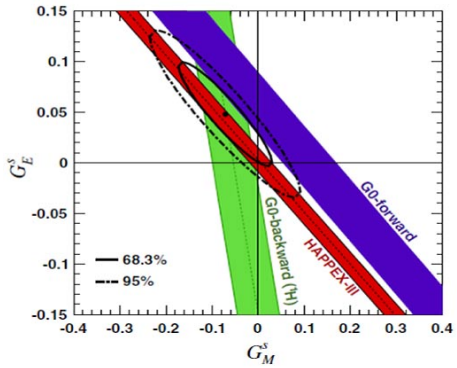

Fig. 16. – From ref. [40]. Constraints on G_E^s and G_M^s at $Q^2 \sim 0.62$ (GeV/c)^2 as derived from the results of the HAPPEX-III and G0-forward and G0-backward experiments.

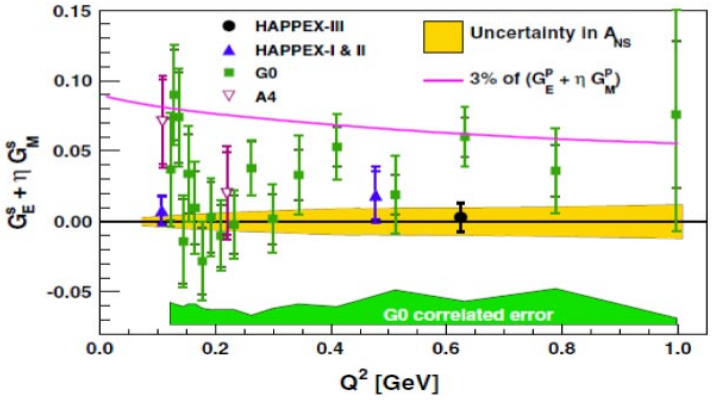

Fig. 17. – From ref. [40]. Results of strange-quark vector form factors for all measurements of forward-angle scattering from the proton. The solid curve represents a 3% contribution to the comparable linear combination of proton form factors.

All the results of the experiments described in this section (see table III) as well as a systematic study of the relevant radiative corrections [64-67] and a careful global analysis [68] show that the strange magnetic form factor is at most a few percent of the proton magnetic form factor at low Q^2 and the strange electric radius is also at most a few percent of the proton charge radius. This result substantially disagrees with the first calculations of nucleon vector form factors in lattice QCD that instead predicted a large contribution of the strange quarks to the charge and magnetization distributions of the proton. As pointed out by ref. [69], the disagreement between theoretical predictions and experimental results disappears if one takes into account in the calculations the finite size of the hadron, which suppresses meson loops when the corresponding Compton wavelength is smaller than the size of the hadron emitting or absorbing the meson. For this reason, because typically a hadron size is 1 fm and the Compton wavelength of a meson of mass of 0.4 GeV is 0.5 fm, the contribution of strange quarks to nucleon properties are suppressed because the mass of the kaon is 0.5 GeV.

4. – Neutron radius in heavy nuclei

The measurement of the Parity Violating asymmetry in electron scattering is a powerful tool to determine neutron densities in nuclei. In fact, when measuring the Parity Violating asymmetry in electron scattering on nuclei, the contribution of the electromagnetic part of the potential electron-nucleus, mostly sensitive to the proton distribution in the nucleus, disappears because it is parity conserving. The Parity Violating asymmetry is hence proportional to the interference between the axial and the electromagnetic part of the potential and the contribution of the axial part of the potential electron-nucleus can be detect despite the fact that it is negligible with respect to the electromagnetic part. Because the axial part of the potential electron-nucleus is sensitive to the weak charge in the nucleus and because the weak charge of the neutron is much larger than that of the proton, the measurement of the the Parity Violating asymmetry in electron scattering on nuclei is a method to determine the neutron densities. This method is conceptually equivalent to the measurement of nuclear charge densities through electron

scattering performed in the past. When measuring the nuclear weak charge density (and hence the neutron density) through electron scattering all the properties which made so successful the measurements of nuclear charge densities through electron scattering apply. In other words the measurement is performed with a clean, non-strong interacting, probe and we can use the Perturbation Theory in the interpretation of the data. Despite this, although the possibility to measure neutron densities through Parity Violating asymmetry was outlined several years ago [70], only in 2010 the first measurement of a neutron radius in a nucleus was performed with this technique [71]. The reason of that is that the asymmetries involved are so small (of the order of half part of a million) that a whole series of other experiments measuring bigger asymmetries, like the ones concerning the contribution of strange quarks to the properties of the nucleon described in sect. **3**, had to be performed in order to ensure that the technical difficulties involved had been overcome. Up to few years ago, neutron densities were hence measured through hadron scattering experiments involving, for example, pions [72], protons [73-75] or antiprotons [76,77], whose interpretation required model-dependent descriptions of the non-perturbative strong interaction.

In the Born approximation A_{PV}, the Parity Violating cross-section asymmetry for longitudinally polarized electrons elastically scattered from an unpolarized nucleus, is expressed as

$$A_{\mathrm{PV}} \approx \frac{G_F Q^2}{4\pi\alpha\sqrt{2}} \frac{F_W(Q^2)}{F_{\mathrm{ch}}(Q^2)}, \tag{63}$$

where G_F is the Fermi constant, α is the fine structure constant, and $F_W(Q^2)$ and $F_{\mathrm{ch}}(Q^2)$ are the Fourier transforms of the weak charge density and of the known charge density respectively. The Fourier transform of the weak charge density is closely related to the neutron density, and therefore, the neutron density and the related value of the neutron radius can be extracted from an electroweak measurement. For heavy nuclei the Born approximation is not valid and Coulomb distortion effects must be included. These have been accurately calculated [78] because the charge density is well known.

The experiment PREX [71] measured for the first time a neutron radius of a nucleus through electron scattering. The nucleus chosen was ^{208}Pb because it is a doubly-magic nucleus with 44 more neutrons than protons. Some of these extra neutrons are expected to be found in the surface, where they form a neutron-rich skin. The difference between the neutron radius R_n and proton radius R_p, which is the thickness of this neutron skin, is hence expected to be enhanced in lead with respect to other nuclei. The thickness of the neutron skin is sensitive to nuclear dynamics and its measurement provides fundamental nuclear structure information, is an important check of fundamental neutron matter calculations and constrains three-neutron forces [79, 80]. Besides, the measurement of the neutron radius of ^{208}Pb has important implications in astrophysics. Measuring R_n constrains the equation of state (EOS), the pressure as a function of density, of neutron matter. A larger pressure P will push neutrons out against surface tension increasing R_n. There is a correlation between R_n and the neutron star radius r_{NS} [81]. In general we can say that a larger value of R_n implies a stiffer EOS, with a larger pressure. A large value of R_n would suggest that r_{NS} is large too. A precise measurement of R_n would hence solve the disagreement between contradictory measurements of r_{NS} which have produced consequently contradictory prediction of the EOS at high densities [82, 83]. The EOS of neutron-rich matter is closely related to the symmetry energy S, which is the energy cost paid for having different numbers of neutrons an protons. There is a

strong correlation between R_n and the density dependence of the symmetry energy $\frac{\mathrm{d}S}{\mathrm{d}\rho}$, with ρ the baryon density. The symmetry energy S helps determine the composition of a neutron star. A large S at high density would imply a large proton fraction, which would allow the direct Urca process of rapid neutrino cooling [84] through the two reactions: $\mathrm{n} \to \mathrm{p} + \overline{\nu_\mathrm{e}}$; $\mathrm{p} + \mathrm{e}^- \to \mathrm{n} + \nu_\mathrm{e}$. If $R_n - R_p$ in ^{208}Pb were large, it is likely that massive neutron stars would cool quickly by direct Urca. In addition, the transition density from a solid neutron star crust to the liquid interior is strongly correlated with $R_n - R_p$ [85]. A large value of $R_n - R_p$ would imply that the EOS is stiff. This would not favor phase transitions and would imply that the neutron star crust is thin. The measurement of the neutron radius of ^{208}Pb has connections also with the heavy-ion physics, because the symmetry energy can be probed in heavy-ion collisions [86], and in atomic physics because of the sensitiveness to R_n of the Atomic Parity Violation (APV) experiments aiming to test the Standard Model at low energies [87, 88].

The experiment PREX took place in the experimental HALL A at JLab. The experimental apparatus was very similar to the ones of the experiments of the HAPPEX series (see sect. **3**). The experiment employed a 1.06 GeV electron beam of 50–70 μA. The beam polarization, as measured by a Compton and by a Moller polarimeter, was equal to $89.2 \pm 1.0\%$. The Q^2 value was 0.00880 ± 0.00011 $(\mathrm{GeV/c})^2$. The target consisted in a 0.55 mm thick isotopically pure ^{208}Pb target foil. The use of a 4×4 mm square beam raster prevented the target from melting. The lead foil was sandwiched between two 150 μm diamond foils to improve its thermal conductance to a copper frame cooled to 20 K with cryogenic helium. The elastically scattered electrons were focused by two equal High Resolution Spectrometers (HRS) onto thin quartz detectors. Figure Of Merits required the detection of the scattered electrons at very forward angles. A pair of dipole septum magnets between the target and the HRSs were hence added in order to detect electrons scattered at a scattering angle $\theta_\mathrm{lab} \sim 5^\circ$ (minimum scattering angle of the particles detectable by the HRSs without the septa: 12.5°). The HRS high momentum resolution ensured that only elastic events (and a negligible fraction of inelastic events from the 2.6 MeV first excited state) were accepted by the quartz detectors (see fig. 18). Čerenkov light from each quartz bar traversed air light guides and were detected by 2-inch quartz-window photomultipliers (PMT). One source of noise experienced by the experiment was the presence of non-uniformities in the target thickness due to thermal damage and was eliminated by locking the raster pattern frequency to a multiple of the helicity frequency. Low-current calibration data, triggered on individual scattered electrons, were regularly collected to evaluate the thickness of lead relative to diamond. Sensitivity of the measured asymmetry to a transverse component of the beam polarization, coupled to the vector analyzing powers (A_T) for ^{208}Pb and ^{12}C, was studied using special runs with fully transverse beam polarization. The only non-negligible background was the fraction of electrons from ^{12}C and was on average equal to $6.3 \pm 0.6\%$. The asymmetry of this background was determined using the e-N weak neutral isoscalar coupling with standard electroweak corrections [42] and the measured kinematics.

After all the corrections the measured asymmetry was

$$A = 656 \pm 60 \text{ (stat)} \pm 14 \text{ (syst) ppb.} \tag{64}$$

To determine R_n from this result, the Parity Violating asymmetries from seven non-relativistic and relativistic mean-field models were calculated. For each model the calculation was performed solving the Dirac equation [78] for an electron scattering from

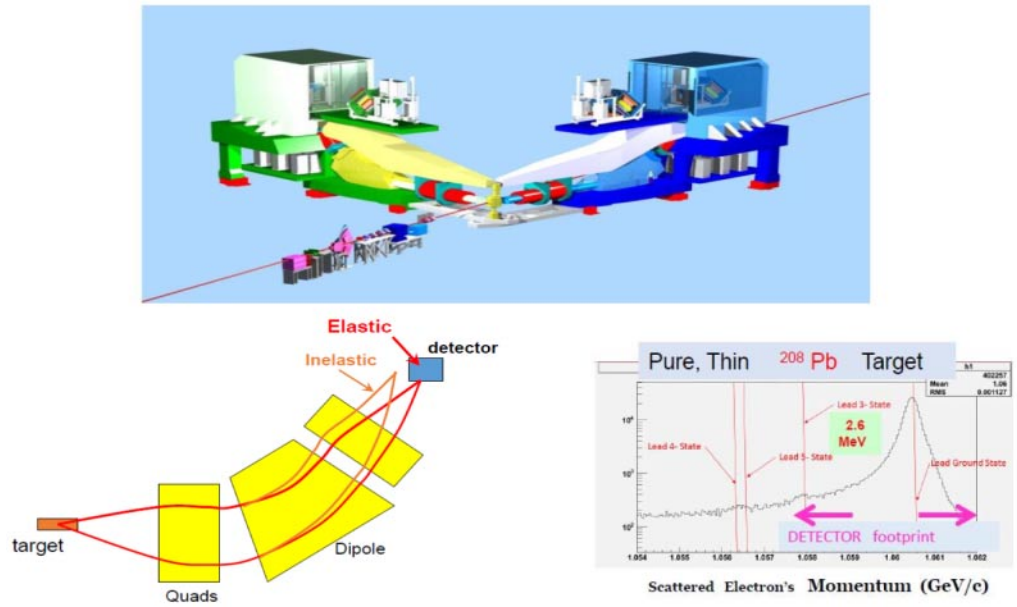

Fig. 18. – From ref. [89]. Top: the High Resolution Spectrometer pair used to discriminate between elastically and inelastically scattered electrons in the experiment PREX. Bottom: the HRS high momentum resolution ensured that only elastic events (and a negligible fraction of inelastic events from the 2.6 MeV first excited state) were accepted by the quartz detectors.

the model weak charge density ρ_w and from the experimental charge density ρ_{ch}. ρ_w was calculated from the model point proton and neutron densities. The resulting Parity Violating asymmetry, that was dependent on the electron scattering angle, was then integrated over the acceptance of the experiment. The results of these calculations are shown in fig. 19 and can be fitted with the fuction

$$R_n \approx 6.156 + 1.675\langle A\rangle - 3.420\langle A\rangle^2 \,\mathrm{fm}, \tag{65}$$

with $\langle A\rangle$ in ppm.

Figure 19 show also the results from plane-wave calculations, which are not valid for heavy nuclei and are not all contained within the vertical axis range of the figure.

From eq. (64) and eq. (65), the following value R_n for ^{208}Pb was obtained:

$$R_n = 5.78^{+0.16}_{-0.18}\,\mathrm{fm}. \tag{66}$$

Assuming a point-proton radius of 5.45 fm [96], corresponding to the measured charge radius of 5.50 fm [97], this result implies that the neutron distribution is 1.8σ larger than that of the protons

$$R_n - R_p = 0.33^{+0.16}_{-0.18}\,\mathrm{fm}. \tag{67}$$

This was the first time, although only at 1.8σ confidence level, that the neutron skin in ^{208}Pb was detected in a model-independent way.

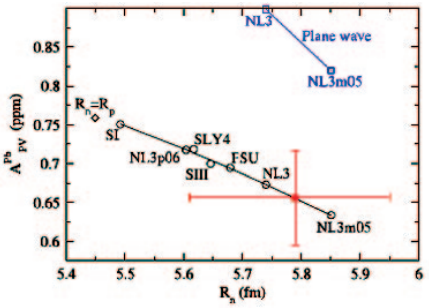

Fig. 19. – From ref. [71]. Result of the PREX experiment (red square) *vs.* neutron point radius R_n in ^{208}Pb. The circles show Parity Violating asymmetry ($A_{\rm PV}$) values for electron scattering on ^{208}Pb as predicted by distorted-wave calculations for seven mean-field neutron densities. The line passing through the circles is a least squares fit of R_n as a function of $A_{\rm PV}$ (eq. (65)). The $A_{\rm PV}$ value expected for $R_n = R_p$ is also shown (diamond) [90]. References: NL3m05, NL3, and NL3p06 from [91], FSU from [92], SIII from [93], SLY4 from [94], SI from [95]. The blue squares show plane-wave impulse approximation results.

From eq. (64) the following value of the weak form factor $F_W(q)$ defined as the Fourier transform of the weak charge density $\rho_w(r)$ was obtained [98]:

$$F_W(\overline{q}) = 0.204 \pm 0.028\ (\text{exp}) \pm 0.001\ (\text{mod}), \tag{68}$$

with $\overline{q} = \langle Q^2 \rangle^{\frac{1}{2}} = 0.475 \pm 0.003\,\text{fm}^{-1}$.

In eq. (68) the first error is the experimental error obtained by adding the statistical and systematic errors in eq. (64) in quadrature. The second error is the error due to the model dependence of $\rho_w(r)$. The fact that this second error is so small shows that the result reported in eq. (68) is all but independent of the assumed shape of the weak charge density.

From eq. (68), in a slightly more model-dependent way, the value of the weak radius R_W, that is the root-mean-square (rms) radius of the weak charge density, can be derived

$$R_W = 5.826 \pm 0.181\ (\text{exp}) \pm 0.027\ (\text{mod})\,\text{fm}. \tag{69}$$

As shown by the second error, the value of R_W is a little model-dependent because depends on (modest) assumptions about the nucleus surface thickness.

From eq. (69), neglecting, for the weak charge density, meson exchange and spin-orbit currents (being ^{208}Pb a spin-zero nucleus) we obtain for the ^{208}Pb neutron radius the value

$$R_n = 5.751 \pm 0.175\ (\text{exp}) \pm 0.026\ (\text{mod}) \pm 0.005\ (\text{str})\,\text{fm}, \tag{70}$$

with the third (str) error coming from possible strange quark contributions, and for the ^{208}Pb neutron skin the value

$$R_n - R_p = 0.302 \pm 0.175\ (\text{exp}) \pm 0.026\ (\text{mod}) \pm 0.005\ (\text{str})\,\text{fm}. \tag{71}$$

TABLE IV. – *Synoptic table of the kinematic parameters and main result of the experiment PREX.*

Experiment	Average scattering angle	Average Q^2 ($\mathrm{GeV/c^2}$)	Results
PREX	5°	0.00880	$R_n - R_p = 0.33^{+0.16}_{-0.18}\,\mathrm{fm}$

The value of eq. (70) and consequently the value of eq. (71) are smaller than the corresponding values of eq. (66) and eq. (67) because of the dependent model assumptions about the surface thickness used to derive eq. (70) and eq. (71). However eq. (70) agrees with eq. (66) (and consequently eq. (71) with eq. (67)) within the model error.

A future run (called PREX-II) is planned at JLab which will reduce the PREX uncertainties by a factor of 3 [99]. This will discriminate between models that still agree within the errors with PREX result and allow predictions relevant for the description of neutron stars and Parity Violation in atomic systems. The reduction of PREX (mainly statistical) uncertainties will be accomplished by PREX-II by eliminating the sources of downtime that plagued PREX. The main downtime source was the failure of a soft O-Ring that was part of the vacuum coupling of the scattering chamber to the exit beam pipe. This section will be redesigned so that the seals are all-metal. Collimators and shields will reduce in PREX-II the radiation load in Hall A to an acceptable level to avoid the failure of electronic equipment that was another important source of downtime during PREX. Table IV reports the kinematic parameters and the main result of the experiment PREX.

After PREX-II a new experiment called CREX will take place in the experimental Hall A at JLab. CREX [100] aims to measure the neutron skin of the nucleus ^{48}Ca through the measurement of the Parity Violating asymmetry in the elastic scattering of electrons of 2.2 GeV scattered at 4° ($Q^2 = 0.022$ $(\mathrm{GeV/c})^2$). The ^{48}Ca neutron radius will be measured with an accuracy of ± 0.02 fm. The experimental apparatus will be essentially the same of the experiment PREX-II with the exception of new septum magnets that will make the HRS spectrometers able to detect electrons scattered at 4°. Combined with the measurement of the ^{208}Pb neutron radius performed by the experiments of the PREX series, the measurement of the ^{48}Ca neutron radius will have a significant impact on nuclear theory, providing a new and unique input into the isovector sector of nuclear theories. In fact, ^{48}Ca is a nucleus that is enough light to be described by the chiral effective field theory, that, coupled with improved *ab initio* many-body calculations, describes the structure of light to medium-mass nuclei in terms of Nucleon-Nucleon (NN) and three-Nucleon (3N) forces [101], and enough heavy to be described by the nuclear density functional theory (DFT) that works best in medium and heavy nuclei where the concept of a nuclear mean field is more appropriate [102]. DFT is based on energy density functionals (EFD) whose minimization yields the exact ground-state energy and density of a nucleus. While the isoscalar contribution to EFD is relatively well established, thanks to the measurements of basic observables of stable nuclei, such as binding energies and charge radii, that constrain the dependence of the functional on the isoscalar density $\rho_0(r) = \rho_p(r) + \rho_n(r)$ ($\rho_p(r)$ and $\rho_p(r)$ the proton and neutron density respectively) and its gradient $\Delta\rho_0(r)$, there are up to now not many well-measured isovector observables to accurately constrain how the functional depends on the isovector density $\rho_1(r) = \rho_n(r) - \rho_p(r)$ and its gradient $\Delta\rho_1(r)$. Isovector fields predicted by various

functionals hence differ and the predicted values for the neutron skin vary significantly. The functional dependence on the isovector density and its gradient cannot be determined by the experiments of the PREX series alone because the measurement of the ^{208}Pb neutron radius is sensitive, in a model independent way, to the density dependence of the symmetry energy, particularly the slope of the symmetry energy at saturation density, and will be hence on its own not able to provide stringent constraints on nuclear structure models. However, once the slope of the symmetry energy at saturation density has been determined by the experiments of the PREX series, DFT predicts a correlation between the ^{208}Pb and the ^{48}Ca neutron radii. Measuring the neutron radius of ^{48}Ca and comparing it with the ^{208}Pb neutron radius, CREX will be able hence to check how good density functionals model isovector contributions. This will be enhanced by the fact that in ^{48}Ca the role of electromagnetic effects due to the Coulomb interaction is much reduced with respect to ^{208}Pb, thus allowing a cleaner study of nuclear isovector properties. Above all CREX will be sensitive to isovector contributions to the nuclear surface energy because ^{48}Ca has a larger ratio of surface to volume than ^{208}Pb. Being ^{48}Ca a medium mass nucleus, its features, like proton, neutron, charge and weak densities, can also be described by *ab initio* coupled cluster calculations (preliminary results in [103]), that used recently optimized chiral N2LO NN interactions [104] augmented by 3N forces. The effects of 3N forces on the neutron density is significant [105-107]. The measurement of the ^{48}Ca neutron radius performed by CREX will provide hence a useful test of *ab initio* theory and relate DFT results to underlying NN and 3N interactions.

5. – Parity Violating Electron Scattering and Standard Model tests

Because Parity Violating asymmetry measurements in electron scattering enhances the contribution of the weak part of the electroweak potential to the measurement and because Standard Model provides precise predictions on the values of the effective weak couplings as well as on the weak charges of the proton and of the electron that are sensitive to the weak part of the electroweak potential, and because all these physics quantities can be expressed in term of $\sin^2\theta_W$, with θ_W the weak mixing angle, Parity Violation in electron scattering can be employed to test the Standard Model and to search for physics Beyond the Standard Model. A measurement of the values of the physics quantities quoted above in agreement with the Standard Model predicted values will confirm the Standard Model. On the contrary, new interactions will manifest themselves in a disagreement between Standard Model and measured values.

This section will be split in three subsections, dealing respectively with the the measurement of the weak couplings between the electron and the quarks, with the proton weak charge measurement, and with the electron weak charge measurement. Table V reports the kinematic parameters and main results of the experiments described in this section.

5˙1. *Weak couplings between the electron and the quarks.* – The effective weak couplings are known as C_{1q} and C_{2q}. The subscripts 1 and 2 refer to whether the coupling to the electron or quark is vector or axial-vector in nature: $C_{1u(d)}$ is the (AV) combination of the electron axial-vector weak charge and the quark vector weak charge, that is, it probes Parity Violation caused by the difference in the Z^0 coupling between left- and right-handed electron chiral states; $C_{2u(d)}$ is the (VA) combination of the electron vector weak charge and the quark axial-vector weak charge that is sensitive to Parity Violation due to the different quark chiral states. According to the Standard Model the values of

TABLE V. – *Synoptic table of the kinematic parameters and main results of the experiments described in sect.* **5**. *For sake of homogeneity, the errors of the results reported are the sums in quadrature of all the errors quoted by the relative papers.*

Experiment	Average scattering angle	Average Q^2 (GeV/c^2)	Results
MIT C12	$\approx 35^\circ$	0.0225	$C_{1u} + C_{1d} = 0.136 \pm 0.033$
SAMPLE-II	146.1°	0.091	$C_{2u} - C_{2d} = -0.042 \pm 0.057$
SAMPLE-III	146.1°	0.038	$C_{2u} - C_{2d} = -0.12 \pm 0.074$
Mainz	130°	0.20	$2.68C_{1u} - 0.64C_{1d} +$ $2.16C_{2u} - 2.00C_{2d} = -0.94 \pm 0.21$
SLAC E122	4°	1.39	$2C_{1u} - C_{1d} = -0.90 \pm 0.17$; $2C_{2u} - C_{2d} = 0.62 \pm 0.81$; $\sin^2\theta_W = 0.224 \pm 0.020$
PVDIS	12.9 and 20.0	1.085 and 1.901	$(2C_{2u} - C_{2d})\vert_{Q^2=0} = -0.145 \pm 0.068$; $\sin^2\theta_W(Q^2 = M_Z^2)_{\overline{MS}} = 0.2299 \pm 0.0043$
Q_{weak}	7.9°	0.025	$C_{1u} = -0.1835 \pm 0.0054$ $C_{1d} = 0.3355 \pm 0.0050$ $Q_W^p = 0.063 \pm 0.012$ $Q_W^n = -0.975 \pm 0.010$
SLAC E158	0.34°	0.026	$\sin^2\theta_W(Q^2 = M_Z^2)_{\overline{MS}} = 0.2330 \pm 0.0015$

the effective weak couplings are

$$
\begin{aligned}
C_{1u} &= -\frac{1}{2} + \frac{4}{3}\sin^2\theta_W, \\
C_{1d} &= +\frac{1}{2} - \frac{2}{3}\sin^2\theta_W, \\
C_{2u} &= -\frac{1}{2} + 2\sin^2\theta_W, \\
C_{2d} &= +\frac{1}{2} - 2\sin^2\theta_W.
\end{aligned} \tag{72}
$$

In testing the Standard Model it is important to determine all four $C_{1u,1d,2u,2d}$ as accurately as possible.

We can divide the experiments that determine the weak couplings between the electron and the quarks through the measurement of the Parity Violating asymmetry in electron scattering into three categories: the experiments that measure these asymmetries in elastic electron scatterings, the experiments that perform these measurements in quasielastic electron scatterings, and the experiments that perform these measurements in Deep Inelastic Scattering regime. We describe first the experiments that determined the weak couplings through elastic electron scatterings.

At the MIT-Bates Linear Accelerator Center, the Parity Violating asymmetry in the

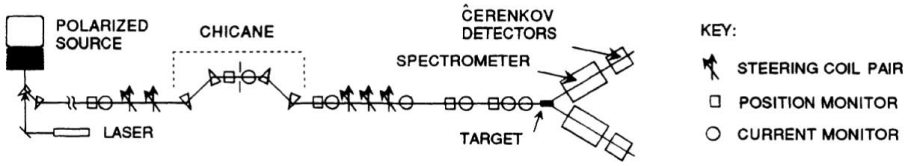

Fig. 20. – From ref. [108]. Schematic diagram of the apparatus utilized to measure the Parity Violating asymmetry in elastic electron scattering from a ^{12}C target at MIT. The beam electrons, whose energy was measured in the chicane, were scattered by the target and detected, at a scattering angle of about 35°, by focusing them by a pair of single-quadrupole spectrometers onto lucite Čerenkov detectors.

elastic scattering of electrons on ^{12}C nuclei [108] was measured. The use of a target of ^{12}C has the advantage that the relevant nuclear physics may be described by a single form factor which cancels in the asymmetry, since ^{12}C is spinless and isoscalar. At energies where a phenomenological four-fermion interaction is appropriate, the Parity Violating asymmetry may be expressed at the tree level as [109, 110]

$$A_{\mathrm{PV}} = \frac{G_F Q^2}{\sqrt{2}\pi\alpha}\frac{3}{2}\overline{\gamma}, \tag{73}$$

where G_F and α are, as usual, the Fermi coupling constant and the fine structure constant, and $\overline{\gamma}$ is the Parity Violating coupling constant for an axial-vector coupling to the electron and an isoscalar coupling to the hadronic constituents. In the Standard Model $\overline{\gamma}$ is given by $C_{1u} + C_{1d} = \frac{2}{3}\sin^2\theta_W$. The experiment used electrons of 250 MeV and a carbon target 5 g/cm^2 long. The beam current was 30–60 μA, the beam polarization 37%. The Q^2 value was 0.0225 (GeV/c)^2. The scattered electrons were detected at a scattering angle of about 35° by focusing them by a pair of single-quadrupole spectrometers onto lucite Čerenkov detectors (see fig. 20).

The measured asymmetry was equal to

$$A = 0.60 \pm 0.14\ (\mathrm{stat}) \pm 0.02\ (\mathrm{syst})\ \mathrm{ppm}, \tag{74}$$

where the first error is statistical and the second is systematic. From eq. (74), applying various scale factors, including the backgrounds due to inelastic nuclear levels and neutrons, the following value of $\overline{\gamma} = C_{1u} + C_{1d}$. was obtained:

$$\overline{\gamma} = 0.136 \pm 0.032 \pm 0.009, \tag{75}$$

in agreement with the Standard Model expected value $\overline{\gamma} = 0.155$.

Other experiments that measured, always at the MIT-Bates Laboratory and through elastic electron scattering, some of the weak couplings between the electron and the quarks, were the experiments SAMPLE-II and SAMPLE-III already described in sect. **3**. The asymmetry measurements performed by these experiments were sensitive to the isovector nucleon axial form factor $G_A^{e(T=1)}$ (see eq. (34) and eq. (37)). Assuming that a determination of nucleon form factors can ultimately be related to electron quark

couplings, the axial form factor can be recast in terms of the parameters C_{2u} and C_{2d} [17]

$$C_{2u} - C_{2d} = -\frac{G_A^{e(T=1)}(1 - 4\sin^2\theta_W)}{G_A(Q^2)} \tag{76}$$

(about $G_A(Q^2)$ see eq. (25)). Equation (76) is modified by the one-quark radiative corrections. These corrections, in which the electron interacts only with a single quark in the nucleon, can be calculated in the Standard Model. The one-quark radiatively corrected values of the couplings within the context of the Standard Model are $C_{2u} = -0.0360$ and $C_{2d} = 0.0265$ with a consequent expected value $C_{2u} - C_{2d} = -0.0624$. Equation (76) is modified, in the case of elastic electron-nucleon scattering, by multi-quark corrections too [22]. These corrections are more uncertain, and although their contribution is small, they dominates the uncertainty in the radiative corrections. Because they concern electron-nucleon elastic scattering, they have to be removed from the data of the experiments SAMPLE-II and SAMPLE-III, in order to compare them with those of the experiments measuring the weak couplings through Deep Inelastic Scattering (see below). After this removal, extrapolating in eq. (76) $G_A(Q^2)$ by using a dipole parameterization, the following values were obtained for C_{2u} and C_{2d}:

in the experiment SAMPLE-II (beam energy equal to 200 MeV, $Q^2 = 0.091$ (GeV/c)^2)

$$C_{2u} - C_{2d} = -0.042 \pm 0.040\ (\text{stat}) \pm 0.035\ (\text{syst}) \pm 0.02\ (\text{Rad. Corr.}), \tag{77}$$

where the third uncertainty is that due to the multi-quark radiative corrections. In the experiment SAMPLE-III (beam energy equal to 125 MeV, $Q^2 = 0.038$ (GeV/c)^2)

$$C_{2u} - C_{2d} = -0.12 \pm 0.05\ (\text{stat}) \pm 0.05\ (\text{syst}) \pm 0.02\ (\text{Rad. Corr.}) \pm 0.01(G_M^s), \tag{78}$$

where the last uncertainty corresponds to variation of G_M^s by ± 0.6, because it was undetermined at the momentum transfer of the SAMPLE-III experiment. It should be noted, however, that the determination of C_{2u} and C_{2d} from the nucleon axial form factor is model-dependent.

The analysis of the experiment Q_{weak} [111] provided another measurement of the weak couplings between the electron and the quarks through elastic electron scattering. The main goal of the Q_{weak} experiment is the measurement of the weak charge of the proton and for this reason the experiment is described in detail in sect. **5**˙2. We mention here that the experiment is providing (the analysis of the data is still in progress) the value of the weak charge of the proton through a fit of the data from the experiment Q_{weak} itself and from the experiments of the series SAMPLE, HAPPEX, A4, and G0 (see sect. **3**). Among the free parameters to be determined by the fit there are C_{1u} and C_{1d}. A preliminary analysis performed on 4% of the Q_{weak} data provided values for these two variables that combined in a fit with the most recent correction to the ^{133}Cs Atomic Parity Violation results [112], determined the following values for C_{1u} and C_{1d}:

$$C_{1u} = -0.1835 \pm 0.0054, \tag{79}$$

$$C_{1d} = 0.3355 \pm 0.0050, \tag{80}$$

with a correlation coefficient equal to -0.980. Figure 21 shows the results of this fit.

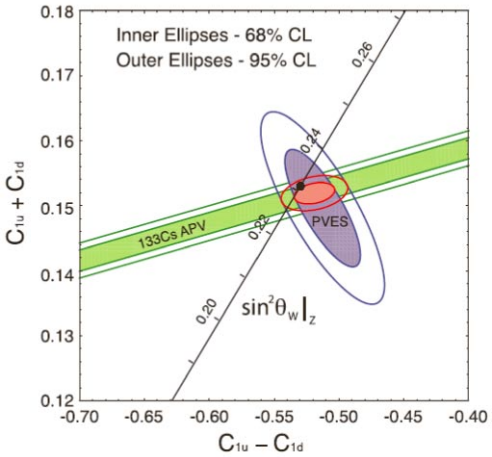

Fig. 21. – From ref. [111]. The constraints on the neutral-weak quark coupling constants $C_{1u} - C_{1d}$ (isovector) and $C_{1u} + C_{1d}$ (isoscalar). The more horizontal (green) APV band (shown at $\Delta\chi^2$ 2.3) provides a tight constraint on the isoscalar combination from ^{133}Cs data. The more vertical (blue) ellipse represents the global fit of the existing $Q^2 < 0.63$ Parity Violating Electron Scattering data including the new result from the Q_{weak} experiment at $Q^2 = 0.025$ (GeV/c)^2. The smaller (red) ellipse near the center of the figure shows the result obtained by combining the Atomic Parity Violation and Parity Violating Electron Scattering information. The Standard Model (SM) prediction [113] as a function of $\sin^2\theta_W$ in the modified minimal subtraction scheme $\overline{MS}$ is plotted (diagonal black line) with the SM best fit value indicated by the (black) point at $\sin^2\theta_W = 0.23116$.

An experiment was performed, in 1986, at the Linac of Mainz, that measured the Parity Violating asymmetry in electron quasielastic scattering from a ^{9}Be target [114]. It was the first experiment that measured asymmetries of the order of 10^{-6} in electron scattering. Consequently, with respect to the previous experiments, the need to contain both the statistical and the systematic error at the level of 10^{-7} called for special care in the design of the electron source in order to fulfill precise requirements concerning its life time, the pulse shape, and the emission asymmetry. Similarly, the procedures to control false asymmetries generated by helicity-correlated changes in beam parameters, nonlinearities of the detector signals, electronic crosstalk, etc. (see sect. **2**) had to be developed at an unprecedented level if not, in some cases, applied for the first time. The experiment utilized electrons of 300 MeV. The beam average current was 7 μA, the beam polarization was 44.9 (first run) and 43.8 (second run). The ^{9}Be target length was 2.4 g cm^{-2}. Four forward lucite Čerenov detectors mounted symmetrically at a scattering angle of 15°, where the Parity Violating asymmetry is very small, were used to control the beam and to normalize the scattered intensity. The experiment detected electrons, scattered by a ^{9}Be target at angles between 115° and 145°, at a Q^2 average value of 0.20 (GeV/c)^2, through a system of 12 ellipsoidal gas Čerenkov counters positioned with axial symmetry around the beam axis and covering the full azimuth (see fig. 22). Each of the twelve ellipsoidal mirrors focused the Čerenkov light onto a separate 2 inch photomultiplier cathode with the target placed in the other focus. Because the Čerenkov photons emitted in air by relativistic electrons are nearly parallel to their momenta, the Čerenkov light detected could be employed for imaging particle vertexes too, allowing background

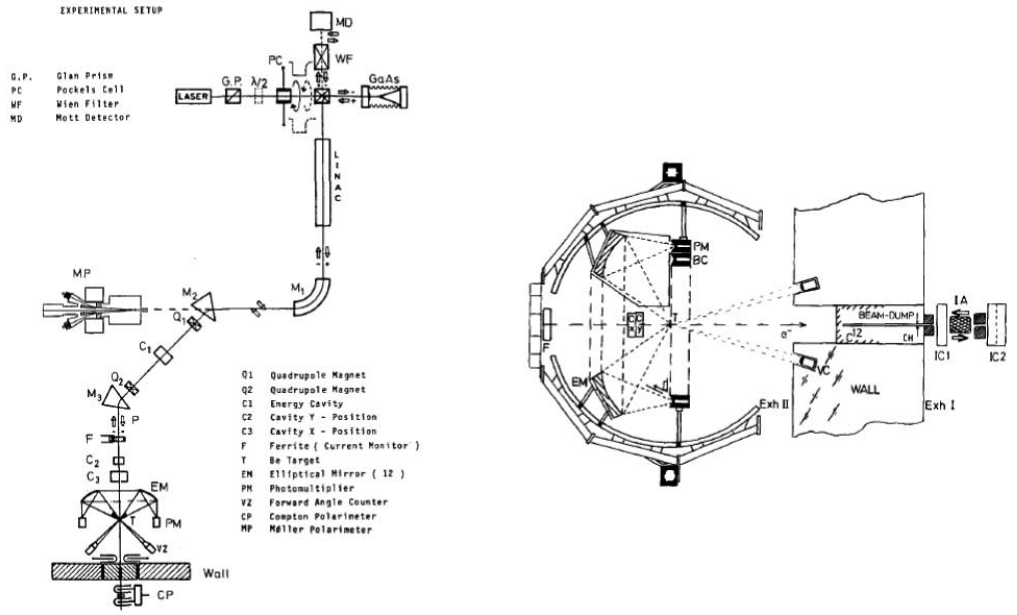

Fig. 22. – From ref. [114]. The parity experiment performed at the Linac of Mainz. Left: the general arrangement of the experiment. Right: the principle of the experiment. The scattered electrons were detected by a system of 12 ellipsoidal gas Čerenkov counters positioned with axial symmetry around the beam axis and covering the full azimuth. Each of the twelve ellipsoidal mirrors focused the Čerenkov light onto a separate 2 inch photomultiplier cathode with the target placed in the other focus. EM = elliptical mirrors. PM = photomultipliers. BC = background counters. VC = forward-angle lucite Čerenkov detectors. T = target.

rejection and subtraction. The effective radiator length varied from 74 cm at a scattering angle of 145° to 116 cm at a scattering angle of 115°. Large parts of the intense radiation tail at low electron scattering energies, as well as the background from any other, heavier particle, were cut off by the threshold of 25 MeV for Čerenkov light production in air by electrons. The electron detection efficiency $T(E', \theta, \phi)$ (E', θ, and ϕ the energy and the scattering angles of the detected electron) and the analog signal height $\Lambda(E', \theta, \phi)$ of the Čerenkov counters were measured and in the analysis the mirrors were divided up into 5 zones of scattering angle θ, where the average values of $T(E', \theta, \phi)$ and $\Lambda(E', \theta, \phi)$ were evaluated. The Λ-values and the knowledge of the electron double differential scattering cross-section enabled a detailed analysis of the composition of the integral analog signal measured. The photomultipliers were shielded against direct background radiation from the target and the beam dump region by 5 cm of lead. However, they were exposed to the halo background produced upstream. The signal-to-background ratio was measured for each detector unit tilting, between subruns, its mirror by remote control so that the target image was scanned over the photocathode. It was found that, in focus, the signal reached a level five times higher than the background. During runs, the background was measured simultaneously by 4 additional photomultipliers units out of the focus, distributed symmetrically over the focus. Further studies on the origin and nature of the background were performed between subruns by removing the target from the beam and by shutters mounted in front of the 12 pohotocathodes of the gas Čerenkov counters

and of the 4 pohotocathodes for background detection. It was found that about 1% of the total signal originated from the halo background. Fake asymmetries generated by Moller scatterings of halo electrons from the poles of the magnets for the beam transport were evaluated to be very small by comparing the signal measured with and without the ^{9}Be target. Fake asymmetries generated by Mott scatterings, expected to be in any case strongly suppressed by the axially symmetric arrangement of the 12 Čerenkov detectors, were evaluated to be very small too.

Taking into account the beam polarization and the background to signal ratio the following value of Parity Violating asymmetry was measured:

$$A = -9.4 \pm 1.8\ (\text{stat}) \pm 0.5\ (\text{syst})\ \text{ppm}. \tag{81}$$

Several processes contribute to this result. The dominant one at the energies and the kinematics of the experiment was the quasielastic scattering that had a maximum at an energy of the scattered electron of about 200 MeV. Contributed to the result quoted in eq. (81) also electrons from radiative tail, electrons produced in scatterings in the dip region and pions from electroproduction. Expressing the cross-sections of these processes in terms of the weak couplings, eq. (81) transforms into

$$2.68C_{1u} - 0.64C_{1d} + 2.16C_{2u} - 2.00C_{2d} = -0.94 \pm 0.21, \tag{82}$$

where the coefficient of C_{1u}, C_{1d}, C_{2u}, and C_{2d} come from the integration of the cross-sections of the processes concerned over the kinematic variables of the experiment. The result quoted in eq. (82) has to be compared with the expected Standard Model value of -0.8544.

In Deep Inelastic Scattering (DIS) from nuclear targets the electron interacts with a single quark, almost independent of the surrounding quarks and gluons. Parity Violating asymmetry measurement in DIS is hence a powerful method to perform precise measurements of the effective weak couplings between the electron and the up (down) quarks. The Parity Violating asymmetry of electron Deep Inelastic Scattering (DIS) off a nuclear target is

$$A_{\text{PV}}^{\text{DIS}} \equiv \frac{\sigma^R - \sigma^L}{\sigma^R + \sigma^L} = \frac{G_F Q^2}{4\sqrt{2}\pi\alpha}\left[2g_A^e Y_1(y)\frac{F_1^{\gamma Z}}{F_1^\gamma} + g_V^e Y_3(y)\frac{F_3^{\gamma Z}}{F_1^\gamma}\right] \tag{83a}$$

$$= \frac{G_F Q^2}{4\sqrt{2}\pi\alpha}[a_1(x)Y_1(y) + a_3(x)Y_3(y)], \tag{83b}$$

where G_F is the Fermi constant, α is the fine structure constant, x is the Bjorken scaling variable, ($x \equiv \frac{Q^2}{2M\nu}$), $F_{1,3}^{\gamma,\gamma Z}$ are structure functions, $y = 1 - E'/E$ is the fractional energy loss with $E(E')$ the incident (outgoing) electron energy, and $g_{A(V)}^e$ is the electron axial (vector) neutral weak coupling [42]. The kinematic factors Y are given by

$$Y_1 = \left[\frac{1+R^{\gamma Z}}{1+R^\gamma}\right]\frac{1+(1-y)^2 - y^2\left[1 - \frac{r^2}{1+R^{\gamma Z}}\right] - xy\frac{M}{E}}{1+(1-y)^2 - y^2\left[1 - \frac{r^2}{1+R^\gamma}\right] - xy\frac{M}{E}}, \tag{84a}$$

$$Y_3 = \left[\frac{r^2}{1+R^\gamma}\right]\frac{1-(1-y)^2}{1+(1-y)^2 - y^2\left[1 - \frac{r^2}{1+R^\gamma}\right] - xy\frac{M}{E}}, \tag{84b}$$

where $\nu = E - E'$, M is the nucleon mass, $r^2 = 1 + \frac{Q^2}{\nu^2}$ and $R^{\gamma,(\gamma Z)}$ is the ratio of the longitudinal to transverse virtual photon electromagnetic absorption($\gamma - Z^0$ interference) cross-sections.

In the quark parton model,

$$a_1(x) = 2g_A^e \frac{F_1^{\gamma Z}}{F_1^Z} = 2\frac{\sum C_{1i} Q_i q_i^+(x)}{\sum Q_i^2 q_i^+(x)}; \qquad a_3(x) = g_V^e \frac{F_3^{\gamma Z}}{F_1^Z} = 2\frac{\sum C_{2i} Q_i q_i^-(x)}{\sum Q_i^2 q_i^+(x)}, \tag{85}$$

where the sum is over the quark flavor $i = u, d, s \ldots$, Q_i is the corresponding quark electric charge, $q_i^{\pm}(x)$ are defined from the Parton Distribution Functions (PDF) $q_i(x)$ and $\bar{q}_i(x)$ as $q_i^+(x) \equiv q_i(x) + \bar{q}_i(x)$, $q_i^-(x) \equiv q_{i,V}(x) \equiv q_i(x) - \bar{q}_i(x)$, and $C_{1i} \equiv 2g_A^e g_V^i$, $C_{2i} \equiv 2g_V^e g_A^i$ with $g_{A(V)}^i$ the quark axial (vector) neutral weak coupling [42].

For an isoscalar target such as the deuteron

$$a_1(x) = \frac{6[2C_{1u}(1+R_c) - C_{1d}(1+R_s)]}{5 + R_s + 4R_c}; \qquad a_3(x) = \frac{6(2C_{2u} - C_{2d})R_v}{5 + R_s + 4R_c}. \tag{86}$$

Neglecting effects from heavier quark flavors and assuming that $u^p = d^n$, $d^p = u^n$ ($u, d^{p(n)}$ are the up and down quark PDF in the proton (neutron)), $s = \bar{s}$, and $c = \bar{c}$, one has

$$R_c \equiv \frac{2(c+\bar{c})}{u + \bar{u} + d + \bar{d}}; \qquad R_s \equiv \frac{2(s+\bar{s})}{u + \bar{u} + d + \bar{d}}; \qquad R_v \equiv \frac{u - \bar{u} + d - \bar{d}}{u + \bar{u} + d + \bar{d}}. \tag{87}$$

With good approximation at high x it can be assumed that

$$a_1 = \frac{6}{5}(2C_{1u} - C_{1d}); \qquad a_3 = \frac{6}{5}(2C_{2u} - C_{2d}). \tag{88}$$

Thanks to eq. (83) and eq. (88) Parity Violating asymmetry of electron Deep Inelastic Scattering (DIS) off a deuterium target is a powerful method to precisely determine the values of $2C_{1u} - C_{1d}$ and $2C_{2u} - C_{2d}$. Experimentally, one could extract both $2C_{1u} - C_{1d}$ and $2C_{2u} - C_{2d}$ by measuring asymmetries at different $Y_{1,3}$ values in the DIS regime. However, a precise determination of $2C_{2u} - C_{2d}$ is usually difficult because of its small value in the Standard Model.

The first measurements of Parity Violating asymmetry in Deep Inelastic Scattering of electrons were performed in the historical experiment E122 at SLAC [5,6] (see fig. 23). The experiment utilized electrons of four energies in the range 16.2–22.2 GeV. The beam polarizations was 37%. The targets used were a 30 cm liquid-deuterium and a 30 cm liquid-hydrogen. The experiment detected the scattered electrons utilizing spectrometers at 4° and gas Čerenkov and lead glass detectors that detected electrons with independent integrating methods. The Q^2 value ranged between 1 and 1.9 $(\mathrm{GeV/c})^2$.

A check of the result was performed measuring the asymmetry for a series of runs using the unpolarized beam from the regular SLAC gun. This asymmetry, divided by 0.37, the average value of the polarization of the beam from the GaAs source used to generate polarized electrons, was equal to $(-2.5 \pm 2.2) \times 10^{-5}$, showing that the apparatus was able to measure asymmetries to a level of about 10^{-5}.

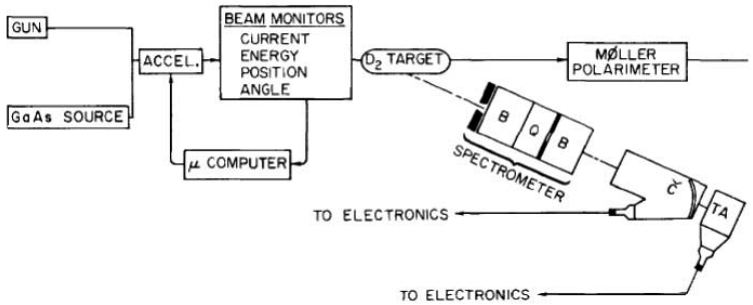

Fig. 23. – From ref. [5]. Schematic layout of the experiment E122 at SLAC. Electrons from the GaAs source or the SLAC regular gun were accelerated by the linac. After momentum analysis in the beam transport system the beam passed through a liquid-deuterium target. Particle scattered at 4° were analyzed in the spectrometer (dipole-quadrupole-dipole) and detected in two separate counters (a gas Čerenkov counter, and a lead-glass shower counter).

The asymmetry measured in the scattering of electrons of 19.4 GeV on proton was

$$\frac{A}{Q^2} = (-9.7 \pm 2.7) \times 10^{-5}\ (\mathrm{GeV/c})^{-2}. \tag{89}$$

For the measurement of the Parity Violating asymmetry in the electron scattering on deuteron, the data obtained with a beam energy of 16.2 GeV, containing fairly strong elastic and resonance contributions, were not employed in the analysis. The same applied for the data obtained with a beam energy of 17.8 GeV, because for that energy the asymmetry was, as expected, negligible due to the fact that the electron spin was transverse because of the electron g - 2 spin precession, relative to the momentum direction, in the transport magnets which deflected the beam before reaching the target (this precession made the beam helicity dependent on beam energy). The Parity Violating asymmetry measurement was performed hence with the data obtained with a beam energy of 19.4 GeV and 22.2 GeV.

The asymmetry measured in the electron scattering on deuteron was

$$\frac{A}{Q^2} = (-9.5 \pm 1.6) \times 10^{-5}\ (\mathrm{GeV/c})^{-2}. \tag{90}$$

This result unequivocally confirmed the parity-violating predictions of electroweak unification, allowing Glashow, Salam and Weinberg to receive the physics Nobel prize. The error $\pm 1.6 \times 10^{-5}$ in eq. (90) originates from statistics ($\pm 0.86 \times 10^{-5}$), beam polarization ($\pm 5\%$), beam ($\pm 3.3\%$), π contamination ($\pm 2\%$), and radiative corrections ($\pm 3\%$).

SLAC E122 was the first experiment that established the value of the Standard Model weak mixing angle too, that was determined using the y-dependence of the asymmetry. The following value of this physics quantity was measured:

$$\sin^2 \theta_W = 0.224 \pm 0.020. \tag{91}$$

From the electron-deuteron data, SLAC E122 determined the following values for the

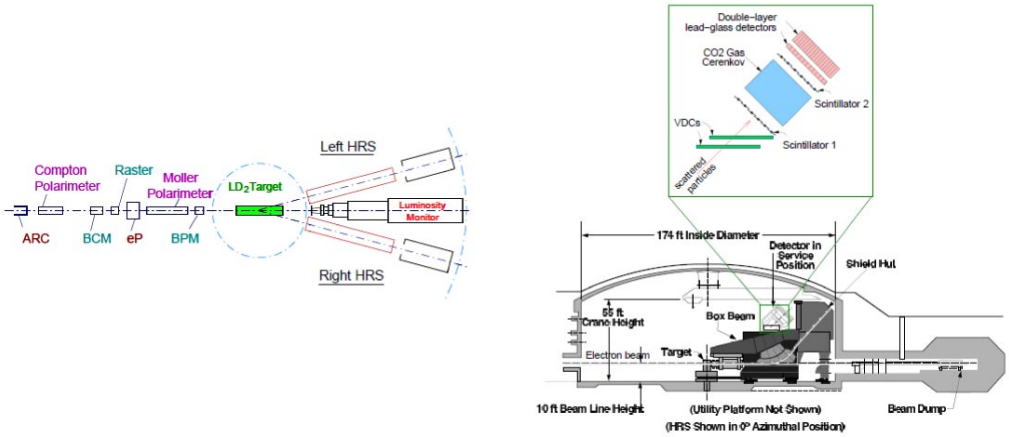

Fig. 24. – From ref. [116] and ref. [117]. Left: schematic diagram of the PVDIS experiment. The electrons (entering from the left) scattered from a liquid-deuterium target in the middle of the hall and were detected in the HRS pair in inclusive mode. Bottom Right: HRS schematic diagram. Top right: zoom-in view of the detector package in the HRS.

weak couplings at $Q^2 = 1.39$ (GeV/c)^2:

$$2C_{1u} - C_{1d} = -0.90 \pm 0.17 \tag{92}$$

(expected Standard Model value: -0.7185) and

$$2C_{2u} - C_{2d} = 0.62 \pm 0.81 \tag{93}$$

(expected Standard Model value: -0.0983).

After about thirty years the experiment PVDIS [115] (see fig. 24) in the experimental Hall A at JLab made a new measurement of the Parity Violating asymmetry of $\vec{e} - {}^2\mathrm{H}$ Deep Inelastic Scattering. The beam current was $100\,\mu$A and the beam polarization nearly 90%. The liquid-deuterium target was 20 cm long. The experiment used the same High Resolution Spectrometers (HRS) utilized by the experiments of the HAPPEX series (see sect. **3**) and by the experiment PREX (see sect. **4**). With respect to these experiments, PVDIS measured asymmetries larger by 1-2 orders of magnitude. The control of beam-related systematic uncertainties, which was the major challenge to the experiments of the HAPPEX series and to the experiment PREX, was hence less of a concern for PVDIS. In contrast, because of the high pion background typical to Deep Inelastic Scattering measurements, the traditional integration method to measure the scattered electron flux could not be used and a specially designed trigger and fast counting Data Acquisition system (DAQ) were used, in order to distinguish pions from electrons and to cope with the high electron event rate. In each HRS, the CO_2 gas Čerenkov detector and the double-layered lead-glass shower counter were used for particle identification at the hardware level and both electron and pion triggers were formed and counted by scalers. The deadtime correction from the DAQ was challenging. The deadtime of the DAQ consisted of three parts: the path deadtime caused by summing and discriminating the preshower and shower signals to form preliminary electron and pion triggers; the veto

deadtime caused by combining the preshower/shower triggers with the HRS trigger and Čerenkov signals; and the "final OR" deadtime caused by taking the logical OR of the paths to form the final electron and pion triggers for the HRSs. A full scale simulation package was developed to study specifically the timing performance of the DAQ and the results of the simulations were checked against data from the pre-installed tagger system, data from flash-ADCs and first-order calculations.

The data were taken at two kinematical settings. At a scattering angle of 12.9°, $E = 6.067\,\text{GeV}$, $x = 0.241$, $Y_1 = 1$, $Y_3 = 0.44$ and $Q^2 = 1.085\ (\text{GeV/c})^2$ the measured Parity Violating asymmetry was equal to

$$A = -91.1 \pm 3.1\ (\text{stat}) \pm 3.0\ (\text{syst})\ \text{ppm} \tag{94}$$

to be compared with the Standard Model expectation of

$$A_{\text{SM}} = -87.7 \pm 0.7\,\text{ppm}, \tag{95}$$

with the uncertainty dominated by the uncertainty in the Parton Distribution Functions (PDFs). Using the MSTW2008 leading-order PDF parametrization [118], A_{SM} is expressed as function of C_{1u}, C_{1d}, C_{2u}, and C_{2d} as

$$A_{\text{SM}} = 1.156 \times 10^{-4}[(2C_{1u} - C_{1d}) + 0.348(2C_{2u} - C_{2d})], \tag{96}$$

with relative uncertainties of the coefficients for the $2C_{1u} - C_{1d}$ and $2C_{2u} - C_{2d}$ terms equal to 0.5% and 5%, respectively.

At a scattering angle of 20.0°, $E = 6.067\,\text{GeV}$, $x = 0.295$, $Y_1 = 1$, $Y_3 = 0.69$ and $Q^2 = 1.901\ (\text{GeV/c})^2$ the measured Parity Violating asymmetry was equal to

$$A = -160.8 \pm 6.4\ (\text{stat}) \pm 3.1\ (\text{syst})\ \text{ppm}, \tag{97}$$

with the Standard Model expected value equal to

$$A_{\text{SM}} = -158.9 \pm 1.0\,\text{ppm} \tag{98}$$

and the asymmetry expressed as function of C_{1u}, C_{1d}, C_{2u}, and C_{2d} through the use of the MSTW2008 leading-order PDF parametrization equal to

$$A_{\text{SM}} = 2.022 \times 10^{-4}[(2C_{1u} - C_{1d}) + 0.594(2C_{2u} - C_{2d})], \tag{99}$$

with relative uncertainties of the coefficients for the $2C_{1u} - C_{1d}$ and $2C_{2u} - C_{2d}$ terms equal to 0.5% and 5%, respectively.

Using the data for the couplings C_{1u} and C_{1d} obtained by the Q_{weak} experiment analysis fit to determine the weak charge of the proton (see above), and from caesium Atomic Parity Violation experiments [112,119-121], a simultaneous fit of $2C_{1u} - C_{1d}$ and $2C_{2u} - C_{2d}$ to the measured Parity Violating asymmetries of the experiments PVDIS and SLAC E122 yielded for $2C_{2u} - C_{2d}$ the value

$$(2C_{2u} - C_{2d})|_{Q^2=0} = -0.145 \pm 0.066\ (\text{exp}) \pm 0.011\ (\text{PDF}) \pm 0.012\ (\text{HT}), \tag{100}$$

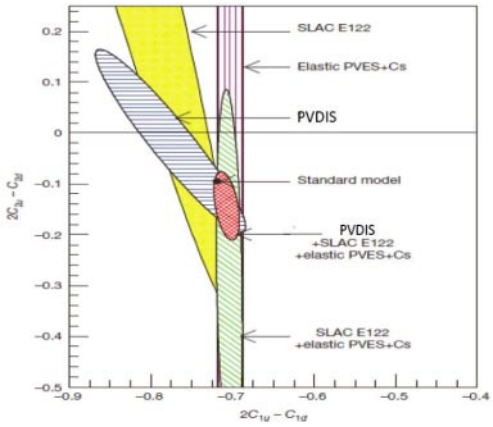

Fig. 25. – From ref. [115]. Values of $(2C_{1u} - C_{1d})|_{Q^2=0}$ and $(2C_{2u} - C_{2d})|_{Q^2=0}$ from the PVDIS experiment (ellipse with blue horizontal hatching) compared with those of SLAC E122 (yellow ellipse) [5,6]. The data on C_{1q} from the Q_{weak} experiment analysis to determine the weak charge of the proton [111] and from atomic Cs [112,119-121] are shown as the band with magenta vertical hatching. The ellipse with diagonal green hatching shows the combined result of SLAC E122 and the C_{1q} from the Q_{weak} experiment analysis and from atomic Cs, while the ellipse with red cross-hatching shows the combined result of SLAC E122, the experiment PVDIS, and the C_{1q} from the Q_{weak} experiment analysis and from atomic Cs. The Standard Model value (with negligible uncertainty) is shown as the black dot, where the size of the dot is for visibility.

where the first error is the total experimental uncertainty, given by the statistical and the systematic uncertainties of the asymmetry results added in quadrature, the second error is the uncertainty in the Parton Distribution Functions (PDF) and the third error is due to the higher-twist (HT) effects. Equation (100) is the first direct measurement of the coupling combination $2C_{2u} - C_{2d}$ that deviates from zero and is in good agreement with the Standard Model prediction

$$(2C_{2u} - C_{2d})|_{Q^2=0} = -0.0950 \pm 0.0004. \tag{101}$$

Figure 25 compares the PVDIS results with those of earlier experiments and predictions of the Standard Model.

From eq. (94) and (97) the value of the weak mixing angle θ_W could be determineed. The result, evolved to the mass of the Z boson in the modified minimal subtraction ($\overline{MS}$) scheme, was $\hat{s}^2_Z \equiv \sin^2\theta_{W(Q^2=M_Z^2,\overline{MS})} = 0.2299 \pm 0.0043$, in agreement with the latest Standard Model fit to world data, $\hat{s}^2_Z = 0.23126 \pm 0.00005$. About the search for new physics, a comparison of the PVDIS results with the Standard Model predictions set mass limits Λ below which new interactions are unlikely to occur. For the cases of electron and quark compositeness and contact interactions, using the convention of ref. [122] and the procedure of ref. [123], the limit for the constructive (destructive) interference contribution to the Standard Model is

$$\Lambda^{\pm} = v\left[\frac{8\sqrt{5}\pi}{\left|(2C_{2u} - C_{2d})_{Q^2=0}\right|^{\pm}}\right]^{\frac{1}{2}}, \tag{102}$$

with $|(2C_{2u} - C_{2d})_{Q^2=0}|^{\pm}$ the difference between the Standard Model value and the

TABLE VI. – *The dependence of "New Physics", CSV and higher-twist on the kinematic variables.*

	x	Y	Q^2
New Physics	No	Yes	No
CSV	Yes	No	No
Higher twist	Yes	No	Yes

upper (lower) confidence bound of the data, $v = \sqrt{\frac{\sqrt{2}}{2G_F}} = 246.22\,\text{GeV}$ the Higgs vacuum expectation value setting the electroweak scale, and $\sqrt{5}$ a normalization factor that takes into account the coefficients of the $C_{2u,2d}$ in the denominator. For a 95% confidence level, from eq. (102) the following values for the limits for constructive and destructive interference from Beyond-the-Standard Model physics were extracted:

$$\Lambda^+ = 5.8\,\text{TeV}; \qquad \Lambda^- = 4.6\,\text{TeV}. \tag{103}$$

Taking advantage of the fact that the JLab maximum electron beam energy was upgraded from 6 to 12 GeV, a new experiment PVDIS [124] will be performed in the experimental Hall A at JLab. With respect to the old PVDIS experiment, in the new PVDIS experiment, thanks to the higher beam energies available, a significantly increased phase space for Deep Inelastic Scattering measurements will become available. The first goal of the new PVDIS experiment is, as in the case of the previous PVDIS experiment, the search for new interactions Beyond the Standard Model. This will be performed enhancing the precision of the measurement of $C_{2u,2d}$ achieved by the old experiment PVDIS, thus increasing the sensitiveness to new physics contributions to the $C_{2u,2d}$ and providing a precision measurement of $\sin^2\theta_W$ at an intermediate value of Q^2. Other important goals of the new PVDIS experiment, achievable thanks to the increased phase space available with the higher maximum energy, are the search for higher-twist (HT) effects in the Parity Violating asymmetry and the search for Charge Symmetry Violation (CSV) at the quark level. In fact, the interpretation of the Parity Violating asymmetry in terms of the $C_{1u,1d,2u,2d}$ couplings given by eq. (83) with a_1 and a_3 coefficients given, for an isoscalar target such as the deuteron, by eq. (86) is based on an assumption of electron-quark scattering. With high Q^2 and W^2, and moderate x this assumption is valid. Outside of these kinematics, additional terms in the higher-twist expansion may also contribute. Significant higher-twist effects are observed in Deep Inelastic Scattering cross-sections, but in PVDIS large higher-twist contributions can only be due to quark-quark correlations [125]. There is currently no experimental information on the contribution of higher-twist to PVDIS. Theoretical works have shown that the effects of higher-twist on the Parity Violating asymmetry are small, but possibly not negligible [126,127]. Current extractions of Parton Distributions assume no Charge Symmetry Violation, but non-zero CSV effects have been allowed in some Parton Distribution fits. These fits tend to favor a small amount of CSV [128]. In addition, recent models of CSV also tend to favor a similar, small CSV [129]. Based on these, the size of the effect on Parity Violating asymmetry should be between 0.25% and 0.5%. Any CSV would change the Parity Violating asymmetry and would likely be seen as an x-dependent but Q^2-independent difference in the Parity Violating asymmetry from the predictions of eq. (83) with a_1 and a_3 coefficients given by eq. (86) and eq. (87). The dependence of the Parity Violating asymmetry changes due to New Physics, CSV and higher-twist on kinematics is shown in table VI.

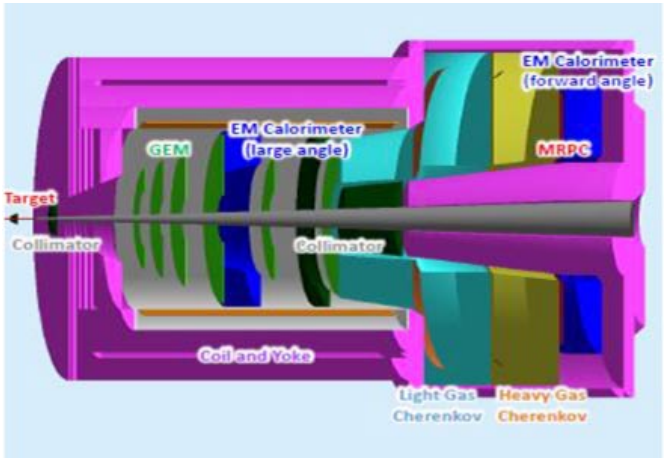

Fig. 26. – From ref. [130]. The SOLID present design. See text for details.

With the kinematic coverage provided by the SOLID spectrometer (see below), the differences between CSV, higher-twist and electroweak physics can be separated by fitting to the functional form:

$$A_{\rm PV}^{\rm DIS} = A_{\rm PV}^{\rm EW}\left[1+\beta_{\rm HT}\frac{1}{(1-x)^3Q^2}+\beta_{\rm CSV}x^2\right], \tag{104}$$

where $A_{\rm DIS}^{\rm EW}$ is the Parity Violating asymmetry due to electroweak physics.

All the goals of the new PVDIS experiment described above will be achieved using a deuterium target. With the use of a proton target, that is not isoscalar, and for which the structure functions do not cancel in the expression for $a_{1,3}(x)$, the new PVDIS will provide a clean measurement of the d-quark over u-quark ratio in the high-x region without nuclear effects.

To address the need for a wide acceptance in both x and Q^2, required by the new PVDIS experiment as well as other experiments scheduled in the experimental Hall A at Jlab, a new, solenoidal spectrometer, named SOLID (Solenoidal Large Intensity Device) [130], (see fig. 26) is being constructed. The kinematic acceptance of this spectrometer will be $0.2 < x < 0.8$ and $2 < Q^2 < 12$ (GeV/c)^2. The spectrometer design is based on a large solenoid, that, for the PVDIS experiment, will be equipped with a series of "baffles". These baffles select the scattered electrons with the appropriate momenta to spiral through them. Tracks are detected in a series of GEM chambers with particle identification given by a threshold gas Čerenkov counter and an electromagnetic calorimeter. The GEM chambers will be divided into two groups, with one group placed in front of the gas Čerenkov counter and the other group behind it. Such configuration will maximize the detector resolution, leading to about 2% momentum and 1 mr polar angle resolutions. In the azimuthal angle, the entire detector system will be divided into 30 independent sectors. The new PVDIS experiment will run with a deuterium target and an hydrogen target and with a 50 μA beam.

The measurements will be performed at two beam energies: 6.6 GeV and 11 GeV. The expected statistical sensitivity of the SOLID spectrometer as a function of x and Q^2 is shown in fig. 27.

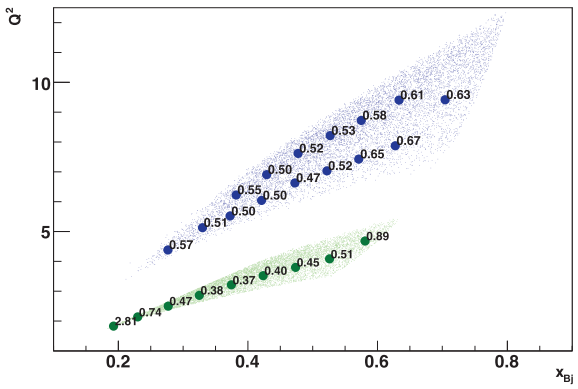

Fig. 27. – From ref. [130]. The expected statistical precision in $A_{\rm PV}^{\rm DIS}$ achieved with the SOLID spectrometer for bins in x and Q^2 for two runs of 120 days at 11 GeV and 60 days at 6.6 GeV with a 50 μA beam and 85% polarization. The dots indicate the bin centers with the statistical precision in percent (%).

5˙2. *The weak charge of the proton.* – The weak charge of the proton Q_W^p is the neutral current analog to the proton electric charge. It is precisely predicted in the Standard Model as

$$Q_W^p = -2(2C_{1u} + C_{1d}), \tag{105}$$

with $C_{1u,1d}$ given by eq. (72). The measurement of Q_W^p is hence a good candidate for an indirect search or new Parity Violating physics between electrons and light quarks and can be performed through the measurement of Parity Violating asymmetries in elastic electron scattering. In fact, eq. (20) can be recast as [131]

$$\frac{A_{\rm PV}}{A_0} = Q_W^p + Q^2 B(Q^2, \theta), \tag{106}$$

with $A_0 = -\frac{G_F Q^2}{4\pi\alpha\sqrt{2}}$.

Equation (106) can be used to determine Q_W^p.

The experiments of the series SAMPLE, HAPPEX, A4, and G0 (see sect. **3**) provided a set of measurements of $A_{\rm PV}$ at different Q^2 values on hydrogen, deuterium, and ^{4}He targets from which Q_W^p can be determined through eq. (106). However, for a precise measurement of Q_W^p, a measurement of $A_{\rm PV}$ at a very small Q^2 value was still lacking. This is being provided by the experiment $Q_{\rm weak}$ [111], that took place in Hall C at JLab. The experiment (see fig. 28) used a 34.4 cm long liquid-hydrogen target and a 145 μA, 89% polarized electron beam whose energy was 1.155 GeV. The averaged Q^2 value was 0.025 $({\rm GeV/c})^2$. The effective scattering angle was $\theta = 7.9°$. The azimuthal angle ϕ covered 49% of 2π. The solid angle was 43 msr. The elastically scattered electrons were focused by a toroidal magnet onto eight quartz Čerenkov detectors, made up by two rectangular bars glued together into 2 m long bars each. The Čerenkov detectors were arrayed symmetrically about the beam axis, 5.7 m downstream of the magnet center and 3.3 m from the beam axis. Azimuthal symmetry was a crucial aspect of the experiment

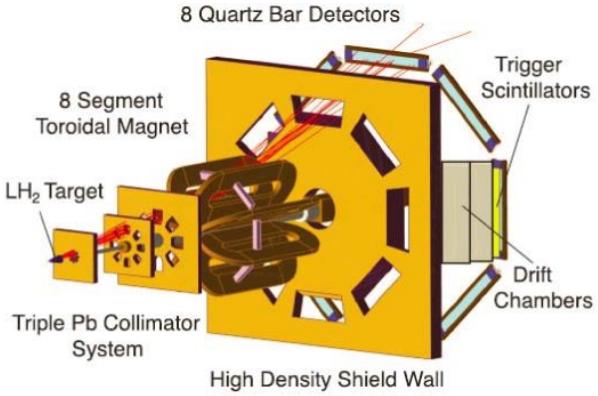

Fig. 28. – From ref. [111]. Q_{weak} basic experimental design. The elastically scattered electrons (red tracks) were focused by a toroidal magnet onto eight quartz Čerenkov detectors while inelastically scattered electrons (not shown), were swept away from the detectors (to larger radii). The acceptance of the experiment was defined by three Pb collimators, each with eight sculpted openings (each opening corresponding to one detector). The distance along the beam line from the target center to the center of the quartz bar detector array was 12.2 m.

design, minimizing systematic errors from helicity-correlated changes in the beam trajectory and contamination from residual transverse asymmetries. The detectors were equipped with 2 cm thick Pb preradiators that amplified the electron signal and suppressed soft backgrounds. The acceptance of the experiment was defined by three Pb collimators, each with eight sculpted openings (each opening corresponding to one detector). A symmetric array of four luminosity monitors was placed on the upstream face of the middle collimator. The detector region was heavily shielded. The beam line inside the detector hut was surrounded with 10 cm of Pb. The response of the detectors was measured in integrating mode except during calibration runs performed at lower beam currents (0.1–200 nA). During these runs, the response of each detector was measured, in a counting mode, using a system of drift chambers and trigger scintillators positioned in front of two detectors at a time and removed during the main measurement. The results of Q_{weak} commissioning run, constituting approximately 4% of the data collected in the experiment, have been already reported [111]. The raw asymmetry, that is the asymmetry measured without applying any corrections, was $A_{\text{raw}} = -169 \pm 31$ ppb. This asymmetry was corrected for potential nonlinearity in the response of the photomultiplier tubes reading the Čerenkov light from the detector bars, and for transverse polarization in the nominally longitudinally polarized beam, whose contribution to the asymmetry was determined from dedicated measurements with the beam fully polarized vertically and horizontally. To the value of the asymmetry determined after these corrections, the contributions of the backgrounds were subtracted. The main source of background was the background from the aluminum windows of the target cell, whose asymmetry was measured in dedicated runs with dummy targets and whose fraction with respect to the total signal was determined from radiatively corrected measurements with the target cell evacuated. Another source of background was due to scatterings in the beam line. The asymmetry and the fraction with respect to the total signal of this background was measured by blocking two of the eight openings in the first of the three Pb collimators with 5.1 cm of tungsten. The asymmetry measured in the detectors associated with the

blocked octants was correlated to that of several background detectors located outside the acceptance of the main detectors for scaling during the primary measurement. A third source of background was generated by soft neutral backgrounds not accounted for in the blocked octant studies and arising from secondary interactions of scattered electrons in the collimators and magnet. The fraction of this background with respect to the total signal was obtained by subtracting the blocked octant background from the total neutral background measured by the main detector after vetoing charged particles using thin scintillators. The asymmetry of the soft neutral backgrounds was considered equal to zero but with an uncertainty of 100% of the e-p elastic asymmetry. A fourth and final source of background arose from the $N \to \Delta(1232)$ transition. Its asymmetry was explicitly measured at low spectrometer magnetic fields and its fraction with respect to the total signal was estimated from simulations. The asymmetry value derived from the background subtraction was corrected for radiative correction deduced from simulations with and without bremsstrahlung, for the measured light variation and non-uniform Q^2 distribution across the detector bars, for the precision in calibrating the central Q^2 value and for the transition, in the determination of the asymmetry, from the average of the measured asymmetries in the Q^2 range covered by the experiment to the asymmetry at the average Q^2 value of the experiment. The fully corrected asymmetry measured by Q_{weak} was

$$A(Q^2 = 0.025) = -279 \pm 35 \text{ (stat)} \pm 31 \text{ (syst) ppb.} \tag{107}$$

Following the procedure outlined in [132, 68], a global fit of asymmetries measured by Q_{weak} and by the experiments of the series SAMPLE, HAPPEX, A4, and G0 on hydrogen, deuterium, and ^{4}He targets was used to extract Q_W^p from eq. (106). Prior to the fitting procedure, the data used in the extraction of Q_W^p were corrected for the $\gamma - Z$ box diagram arising from the axial-vector coupling at the electron vertex, that is the dominant energy-dependent radiative correction [14] to eq. (106) that contributes to Parity Violating Electron Scattering in the forward limit. This correction included the energy dependence of the $\gamma - Z$ box diagram, as calculated in ref. [133], and (for the points above $Q^2 = 0.025$ (GeV/c)^2), the smaller additional correction for the Q^2 dependence of the the $\gamma - Z$ box diagram, calculated using the prescription in ref. [67] with EM form factors from [49]. The fit, that used EM form factors from [49], had effectively five free parameters: C_{1u} and C_{1d}, the strange charge radius ρ_s, the strange magnetic moment μ_s, and the isovector axial form factor $G_A^{e(T=1)}$. The value and uncertainty of the isoscalar axial form factor, $G_A^{e(T=0)}$ (which vanishes at tree level), was constrained by the calculation of [22]. In order to make use of data up to $Q^2 = 0.63$ (GeV/c)^2, a conventional dipole form [62] $G_D = \frac{1}{(1+\frac{Q^2}{\lambda^2})^2}$, with $\lambda = 1$ (GeV/c)^2, was used for the strange quark form factors $G_E^s = \rho_s Q^2 G_D$ and $G_M^s = \mu_s G_D$ as well as for $G_A^{e(T=1)}$.

The values of ρ_s and μ_s obtained in the fit were consistent with an earlier determination [68] but with uncertainties about 4 times smaller (for C_{1u} and C_{1d} see sect. **5**˙1). The fit determined the unknown parameters Q_W^p and B of the function $Q_W^p + Q^2 B(Q^2, \theta)$ of eq. (106) and the measured weak charge of the proton, given by the intercept of this function at $Q^2 = 0$, was

$$Q_W^p = 0.064 \pm 0.012. \tag{108}$$

This result agrees with the Standard Model value $Q_W^p = 0.0710 \pm 0.0007$ [113]. The

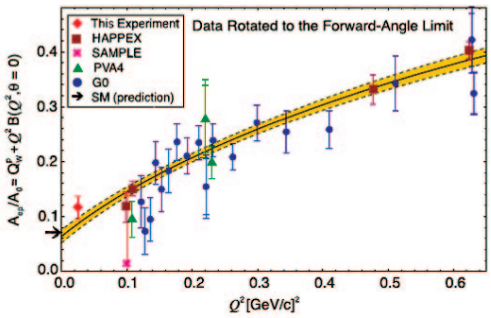

Fig. 29. – From ref. [111]. Global fit result of eq. (106) (solid line) presented in the forward-angle limit as reduced asymmetries derived from the $Q_{\rm weak}$ experiment as well as other Parity Violating Electron Scattering experiments up to $Q^2 = 0.63$ (GeV/c)^2 (see text for details). The additional uncertainty arising from this rotation is indicated by outer error bars on each point. The yellow shaded region indicates the uncertainty in the fit. Q_W^p is the intercept of the fit. The Standard Model prediction [113] is also shown (arrow).

result of eq. (108) is not affected significantly by varying the maximum Q^2 or θ of the data included in the fit as long as the data set is truncated at Q^2 above ~ 0.25 (GeV/c)^2. Truncating the data set at lower Q^2 values tends to destabilize the fit, and enhances the sensitivity to the underlying statistical fluctuations in the data set, as reported in [68]. The effect of varying the dipole mass in the strange and axial form factors is small, with variation in Q_W^p less than ± 0.001, for 0.7 (GeV/c)^2 $< \lambda^2 <$ 2 (GeV/c)^2. Smaller values of λ are disfavored by lattice QCD calculations of strange form factors [62], and the results quickly plateau for larger values. Figure 29 shows the fit result. In order to illustrate the two-dimensional global fit (Q^2, θ) in a single dimension (Q^2), instead of the measured experimental asymmetries, fig. 29 shows the reduced asymmetries obtained from a forward-angle rotation of all the data used in the global fit. This rotation removed the angle dependence of the strange and axial form-factor contributions and was performed by subtracting $A_{\rm calc}(\theta, Q^2) - A_{\rm calc}(0^\circ, Q^2)$ from the measured asymmetries, with the calculated asymmetries $A_{\rm calc}$ determined from eq. (20) using the results of the fit.

As seen in sect. **5**˙1, the values of C_{1u} and C_{1d} derived from the fit of eq. (106) were used, together with the most recent correction to the ^{133}Cs Atomic Parity Violation results, to derive the values of eq. (79) and eq. (80) for C_{1u} and C_{1d}. With these results, from eq. (105) the following value for the weak charge of the proton was derived:

$$Q_W^p = 0.063 \pm 0.012 \tag{109}$$

The result of eq. (109), that takes into account both Parity Violating Electron Scattering and Atomic Parity Violation data, pretty agrees with the result of eq. (108), that was derived from Parity Violating Electron Scattering data only. From the same set of C_{1u} and C_{1d} values used to derive eq. (109), the weak charge of the neutron Q_W^n that, according to the Standard Model, is equal to

$$Q_W^n = -2(C_{1u} + 2C_{1d}), \tag{110}$$

was derived. The following value for the weak charge of the neutron was obtained:

$$Q_W^n = -0.975 \pm 0.010 \tag{111}$$

that agrees pretty well with the Standard Model value of $Q_W^n = -0.9890 \pm 0.0007$ [113].

The analysis of all the data of the experiment Q_{weak} has not ended yet. The final result will provide an asymmetry value with an uncertainty about 5 times smaller than that of eq. (107).

In the future, taking advantage of the construction of the Mainz Energy recovering Superconducting Accelerator (MESA) at Mainz, the experiment P2 [134] will measure the weak charge of the proton with even a smaller uncertainty than Q_{weak}. Equation (20) can be recast as (see eq. (19))

$$A_{\text{PV}}^p = -\frac{G_F Q^2}{4\sqrt{2}\pi\alpha}\rho'(1 - 4k' \sin^2\theta_W - F(Q^2)) = a\rho'(Q_W^p - F(Q^2)), \tag{112}$$

with ρ' and k' arising from electroweak radiative corrections, $a = -\frac{G_F Q^2}{4\sqrt{2}\pi\alpha}$, and

$$\begin{aligned} F(Q^2) &= F_{\text{EM}}(Q^2) + F_{\text{Axial}}(Q^2) + F_{\text{Strange}}(Q^2), \\ F_{\text{EM}}(Q^2) &= \frac{\epsilon G_E^{\gamma p} G_E^{\gamma n} + \tau G_M^{\gamma p} G_M^{\gamma n}}{\epsilon (G_E^{\gamma p})^2 + \tau (G_M^{\gamma p})^2}, \\ F_{\text{Axial}}(Q^2) &= -\frac{(1 - 4\sin^2\theta_W)\sqrt{(1-\epsilon^2)\tau(1+\tau)}\, G_M^{\gamma p} G_A^{Z p}}{\epsilon (G_E^{\gamma p})^2 + \tau (G_M^{\gamma p})^2}, \\ F_{\text{Strange}}(Q^2) &= \frac{\epsilon G_E^{\gamma p} G_E^{s} + \tau G_M^{\gamma p} G_M^{s}}{\epsilon (G_E^{\gamma p})^2 + \tau (G_M^{\gamma p})^2}. \end{aligned} \tag{113}$$

The contribution to A_{PV}^p of $F(Q^2)$ with respect to that of Q_W^p decreases when $\theta \to 0$. P2 will run at a beam energy of 200 MeV, where the total uncertainty has its minimum value. In fact, the total uncertainty includes uncertainties due to statistic and beam systematic that decrease with the beam energy, and uncertainties on electromagnetic form factors (and hence on $F_{\text{EM}}(Q^2)$), and on axial form factors ($F_{\text{Axial}}(Q^2)$) that vice versa increase with the beam energy. The beam polarization will be 85% and the beam intensity 150 μA. The experiment will make use of a 60 cm long liquid-hydrogen target. The Q^2 value will be 0.0029 $(\text{GeV/c})^2$, the average scattering angle of the detected elastically scattered electrons 20°. The elastically scattered electrons will be separated from the background and focused on a detector plane by a magnet. The detector plane will be segmented and will have a full azimuthal coverage. The polarization of the beam will be measured with a precision smaller than 0.5% by a Hydro Møller polarimeter. The expected Parity Violating asymmetry measured by P2 will be −20.55 ppb with a total uncertainty (statistic + systematic) of 0.34 ppb. With this result and thanks to a theoretical effort in progress to calculate two-loop-contribution, box-graphs, electromagnetic radiative corrections, hadronic contributions, $\sin^2\theta_W$ running etc., the total uncertainty on $\sin^2\theta_W$ ($\Delta \sin^2\theta_W$) will be 3.6×10^{-4}. The design of the experiment is still in progress.

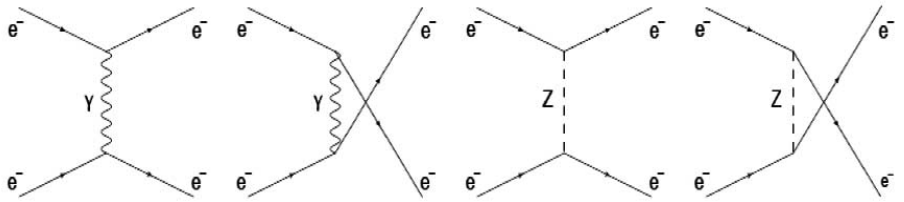

Fig. 30. – Feynman diagrams for Møller scattering at tree level (reproduced from ref. [136]).

5˙3. *The weak charge of the electron.* – In polarized electron scattering from atomic electrons (Møller scattering), at four-momentum transfers much smaller than the mass of the Z^0 boson, $Q^2 \ll M_Z^2$, the Parity Violating asymmetry $A_{\rm PV}$ is dominated by the interference between photon and Z^0 boson exchange [135]. The leading order Feynman diagrams relevant for Møller scattering involve both direct and exchange diagrams that interfere with each other (see fig. 30).

The resulting asymmetry is given by [137]

$$A_{\rm PV}^{\rm Moll} = mE\frac{G_F}{\sqrt{2}\pi\alpha}\frac{4\sin^2\theta}{(3+\cos^2\theta)^2}Q_W^e = mE\frac{G_F}{\sqrt{2}\pi\alpha}\frac{2y(1-y)}{1+y^4+(1-y)^4}Q_W^e, \tag{114}$$

where α is the fine structure constant, G_F the Fermi constant, E the incident beam energy, m the electron mass, θ the scattering angle in the center of mass frame, $y \equiv 1 - E'/E$, where E' is the energy of one of the scattered electrons, and Q_W^e is the weak charge of the electron.

Within the Standard Model the weak charge of the electron, Q_W^e, is proportional to the product of the electron's vector and axial-vector couplings to the Z^0 boson, and the weak neutral current amplitudes are functions of the weak mixing angle $\sin^2\theta_W$. As a consequence, a measurement of Q_W^e determines the value of $\sin^2\theta_W$ too. The electroweak theory prediction at tree level in terms of the weak mixing angle is $Q_W^e = -(1-4\sin^2\theta_W)$; this is modified at the 1-loop level [136,138,139] and becomes dependent on the energy scale at which the measurement is carried out ($\sin^2\theta_W$ "runs"). It increases by approximately 3% compared to its value at the scale of the Z^0 boson mass, M_Z; this and other radiative corrections reduce Q_W^e to -0.0469 ± 0.0006, with about a 40% change with respect to its tree-level value of about -0.075 (when evaluated at M_Z).

Equation (114) can be recast in terms of the analyzing power $A(Q^2, y)$

$$A_{\rm PV}^{\rm Moll} = A(Q^2, y)Q_W^e, \tag{115}$$

where

$$A(Q^2, y) = \frac{G_F Q^2}{\sqrt{2}\pi\alpha(Q)}\frac{1-y}{1+y^4+(1-y)^4}F_{\rm QED}, \tag{116}$$

with $F_{\rm QED}$ a QED radiative correction factor that includes kinematically weighted hard initial and final-state radiation effects and y-dependent contributions from $\gamma\gamma$ and γZ and vertex diagrams.

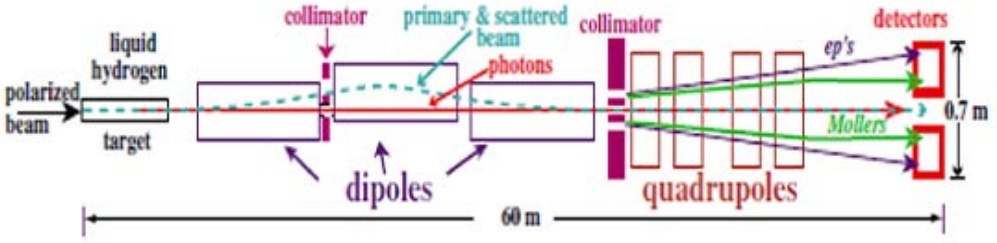

Fig. 31. – From ref. [140]. Schematic plan view of the experimental configuration in SLAC end station A when the experiment E158 took place.

Equation (114) and (115) can be cast as [138]

$$A_{\mathrm{PV}}^{\mathrm{Moll}} = -A(Q^2, y)\rho^{(e;e)}[1 - 4\sin^2\theta_W^{\mathrm{eff}}(Q) + \Delta], \tag{117}$$

with $\rho^{(e;e)}$ the low-energy ratio of the weak neutral and charge current couplings and Δ a term that contains residual $O(\alpha)$ electroweak corrections.

The measurement of the Parity Violating asymmetry in the Møller scattering, providing a measurement of $\sin^2\theta_W^{\mathrm{eff}}$, whose value is predicted by the Standard Model, is a powerful test of the Standard Model itself. As a consequence, it is a powerful tool to search for physics Beyond the Standard Model too. New neutral current interactions are best parameterized model-independently at low energies by effective four-fermion interactions. Focusing on vector and axial-vector interactions between electrons and/or positrons, such an interaction Lagrangian takes the form [122]

$$\mathcal{L}_{\mathrm{e_1e_2}} = \sum_{i,j=L,R} \frac{g_{ij}^2}{2\Lambda^2}\bar{e}_i\gamma_\mu e_i\bar{e}_j\gamma^\mu e_j, \tag{118}$$

where $e_{L/R} = \frac{1}{2}(1 \mp \gamma_5)\psi_e$ are the usual chirality projections of the electron spinor, Λ is the mass scale of the new contact interaction and $g_{ij} = g_{ij}^*$ are coupling constants, with $g_{RL} = g_{LR}$. Then the Parity Violation asymmetry measurement in Møller scattering has a sensitivity to new four-electron contact interaction amplitudes $g_{RR}^2 - g_{LL}^2$ equal to

$$\frac{\Lambda}{\sqrt{|g_{RR}^2 - g_{LL}^2|}} = \frac{1}{\sqrt{\sqrt{2}G_F|\Delta Q_W^e|}}, \tag{119}$$

with ΔQ_W^e the uncertainty on the measurement of Q_W^e.

The experiment E158, that took place in 2002 and in 2003 in the End Station A (ESA) at SLAC (see fig. 31), first measured the electron weak charge and $\sin^2\theta_W^{\mathrm{eff}}$ through the measurement of the Parity Violating asymmetry in Møller Scattering and eq. (115) and eq. (117) [140, 141].

It used a beam with up to 6×10^{11} electrons ~ 270 ns pulses at 120 Hz and a 1.57 m liquid-hydrogen target. The Q^2 and y values were 0.026 $(\mathrm{GeV/c})^2$ and 0.6, respectively. The beam polarization was 85% for the first 40% of the data, increased then to 90% by the use of a novel "superlattice" photocathode. No helicity-dependent cuts were applied on the data, other than the demand that the beam intensity asymmetry measured by two

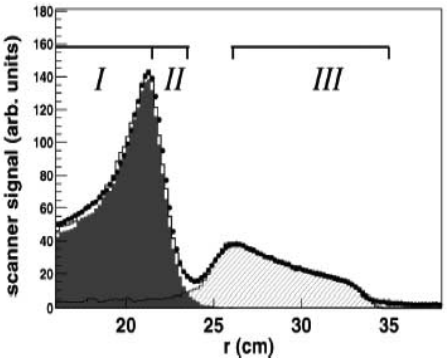

Fig. 32. – From ref. [140]. The charged particle radial profile at the calorimeter of the experiment SLACE158. The points are the data scan, and the open histogram is the Monte Carlo simulation. Møller (shaded) and e-p (hatched) contributions are also shown. Region I and III PMTs were used to measure Møller and e-p asymmetries, respectively.

independent monitors agreed to within 10^{-3} for each right-left pulse pair. The experiment run at two beam energies: 45.0 and 48.3 GeV. Because of g - 2 precession as the beam traversed a 24.5° bend after acceleration, the two beam energies corresponded to opposite orientations of longitudinal beam polarization in ESA. The use of two different energies was hence an additional method to suppress systematic effects with respect to those described in sect. **2**. Scattered particles with a laboratory scattering angle between 4.4 and 7.5 mr over the full range of the azimuth were selected by a magnetic spectrometer and transported to a calorimeter. The calorimeter was a 25 cm long cylindrical structure with a 15 (35) cm inner (outer) radius. It was assembled by layering planes of flexible fused-silica fibers between elliptical copper. The fibers directed Čerenkov light to air light guides, each of which terminated into a shielded photomultiplier tube (PMT). At the detector position, the charged particle flux was approximately azimuthally symmetric about the beam axis. The radial and azimuthal segmentation of the detector made it possible to distinguish between Møller electrons and electrons scattered from target protons (e-p scattering), with the three inner rings predominantly sensitive to Møller scattered electrons and the outermost ring sensitive to the bulk of the e-p scattering flux. This is evident in fig. 32, that shows Monte Carlo simulations of Møller and e-p scattered electrons compared with the measured radial profile at one azimuthal angle provided by the scanning detector system used in the experiment to obtain a complete radial and azimuthal map of the charged particle flux. In fig. 32 the spatial separation between the ring formed by Møller electrons in the range 13–24 GeV and the region hit by the electrons scattered from target protons is evident.

The small contribution of neutral particles, such as photons and neutrons, to the calorimeter response was measured in calibration runs. The asymmetry from pions was measured by using ten quartz bars arranged in azimuthal symmetry behind the Møller detector and lead shielding. Eight gas ionization chambers arranged in 45° azimuthal sections intercepted charged particles with $\theta_{\rm lab} \sim 1$ mr. This "luminosity" detector monitored target density fluctuations and provided a check of the null asymmetry expected at such small scattering angles. An azimuthal modulation of the raw asymmetry caused by a small non-zero transverse beam polarization component was found and corrected. An additional bias to the measured asymmetry was generated by asymmetries in higher-

order moments of beam distributions, such as temporal variations of the beam position or energy within a 270 ns beam pulse, coupled to the intrapulse variation of position or energy asymmetries. This bias was found to be small for the two innermost of the three detector rings sensitive to the Møller electrons, but to be significant for the third one. This bias was corrected in 2003 data by equipping Beam Position Monitors (BPMs) with additional readout channels, in order to digitize BPM signals for charge, energy, positions and angles. Corrections due to intrapulse variation of beam asymmetries were computed by linearly regressing Møller asymmetries against the beam asymmetries. For the 2002 run this was not accomplished and to avoid biases the data from the outermost of the three detector rings sensitive to Møller electrons were not included in the computation of the Parity Violating asimmetry. The bias due to beam spot-size fluctuations was limited using data from a retractable wire array that was inserted into the beam during some of the data collection. The major source of background was due to electrons from inelastic electron- and photon-proton interactions. The correction for this source of background was accomplished measuring the asymmetry in detector regions not sensitive to Møller electrons and with reasonable assumptions for the kinematic extrapolation to the detector regions sensitive to the Møller electrons.

The resulting $A_{\mathrm{PV}}^{\mathrm{Moll}}$ asymmetry was

$$A = -131 \pm 14\ (\mathrm{stat}) \pm 10\ (\mathrm{syst})\ \mathrm{ppb}. \tag{120}$$

From this result and from eq. (117), with $F_{\mathrm{QED}} = 1.01 \pm 0.01$ and the analyzing power $A = 3.25 \pm 0.05$ ppm, determined from Monte Carlo simulations that accounted for energy losses in the target and systematic uncertainties in the spectrometer setup, a value for $\sin^2\theta_W^{\mathrm{eff}}$ was derived. A number of definitions of the low-energy weak mixing angle exist and differ in the way various corrections of order $O(\alpha)$ are distributed between the terms $\sin^2\theta_W^{\mathrm{eff}}$, $\rho^{(e;e)}$ and Δ [142-144, 136]. Defining $\sin^2\theta_W^{\mathrm{eff}}$ in order it reproduces the effective leptonic coupling $\sin^2\theta_W^{\mathrm{eff}}(Q^2 = M_Z^2) \equiv \overline{s}_l^2 = 0.23149 \pm 0.00015$ [145], that implies $\rho^{(e;e)} = 1.0012 \pm 0.0005$ and $\Delta = -0.0007 \pm 0.0009$, the following measurement of $\sin^2\theta_W^{\mathrm{eff}}$ was obtained

$$\sin^2\theta_W^{\mathrm{eff}}(Q^2 = 0.026) = 0.2397 \pm 0.0010\ (\mathrm{stat}) \pm 0.0008\ (\mathrm{syst}). \tag{121}$$

This value agrees with the Standard Model expectations: $\sin^2\theta_W^{\mathrm{eff}}(Q^2 = 0.026) = 0.2381 \pm 0.0006$. Interpreting the result of eq. (121) as a measurement of the electroweak coupling parameter, the following value is obtained:

$$\sin^2\theta_W(Q^2 = M_Z^2)_{\overline{MS}} = 0.2330 \pm 0.0011\ (\mathrm{stat}) \pm 0.0009\ (\mathrm{syst}) \pm 0.0006\ (\mathrm{theor}), \tag{122}$$

where the last uncertainty is from evolution to M_Z. This result sets a limit on the scale Λ_{LL} of a new left-handed contact interaction characterized by a term in the Lagrangian [122] (see eq. (118) with $g_{LL}^2 = 4\pi$)

$$L = \pm\left(\frac{4\pi}{2(\Lambda_{LL}^{\pm})^2}\right)(\overline{e}_L\gamma_\mu e_L), \tag{123}$$

At 95% Confidence Level a tree-level calculation yields $L_{LL}^{+} \geq 7\,\mathrm{TeV}$ and $L_{LL}^{-} \geq 16\,\mathrm{TeV}$ for potential positive and negative deviations, respectively.

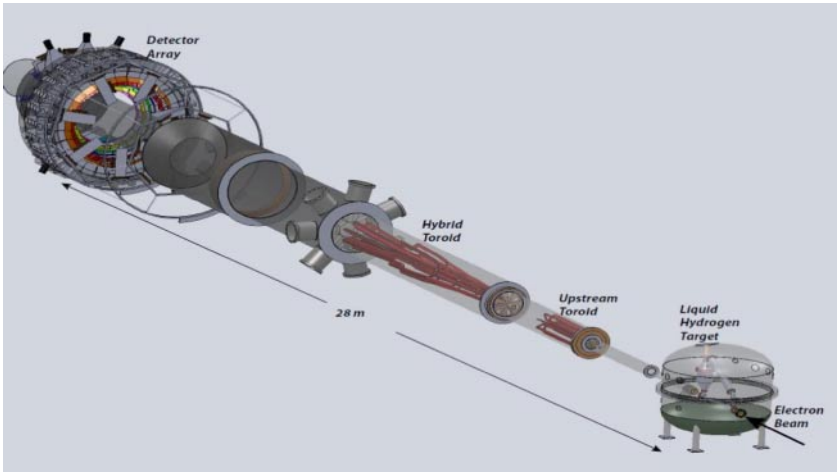

Fig. 33. – From ref. [146]. Conceptual layout of the MOLLER experiment, looking upstream. The target chamber is located on the lower right, then the upstream and hybrid toroids, Roman pots for the tracking detectors, and the main detector stand, with background detectors at the far downstream end on the upper left.

The MOLLER experiment [146], that will take place in the experimental Hall A of JLab, will test the Standard Model prediction of the weak mixing angle, $\sin^2\theta_W$, with a sensitivity of $\delta(\sin^2\theta_W) = \pm 0.00029$ by measuring the Parity Violating asymmetry $A_{\mathrm{PV}}^{\mathrm{Moll}}$ with 2.3% total uncertainty. MOLLER will also be the most sensitive probe of new flavor and CP-conserving neutral current interactions in the leptonic sector, sensitive to interaction amplitudes as small as 1.5×10^{-3} times the Fermi constant. In fact, for the MOLLER proposed measurement with 2.3% total uncertainty (and no additional theoretical uncertainty), the resulting sensitivity to new four-electron contact interaction amplitudes $g_{RR}^2 - g_{LL}^2$ as calculated from eq. (119) is $\sim \frac{246.22\,\mathrm{GeV}}{\sqrt{0.023 Q_W^e}} = 7.5\,\mathrm{TeV}$. For $g_{RR}^2 - g_{LL}^2 = 2\pi$ this will set a limit on the scale Λ equal to about 47 TeV. Thus the MOLLER proposed measurement will greatly extend the current sensitivity of four-electron contact interactions, both qualitatively and quantitatively, and is complementary to direct searches.

The MOLLER experiment (see fig. 33) will use a beam of energy of 11 GeV with $\sim$ 85% polarization, and a 1.5 m liquid-hydrogen target. Møller electrons in the full range of the azimuth (achieved by using an odd number of coils and identical particle scattering) and polar angles $5\,\mathrm{mrad} < \theta_{\mathrm{lab}} < 19\,\mathrm{mrad}$ will be separated from background and focused ~ 30 m downstream of the target by a spectrometer system consisting of a pair of toroidal magnet assemblies and precision collimators (see fig. 34). The upstream magnet is a traditional toroidal magnet, while the downstream magnet has a novel shape designed to focus the large range of scattered electron angles and energies. In the azimuthal dimension, the lower energy electrons are strongly defocussed by radial fields in the downstream magnet. The full range of azimuthal angles is populated hence on the detector plane and the energy distribution of the detected Møller electrons changes with the azimuth. The Møller electrons will be incident on a system of quartz detectors in which the resulting Čerenkov light will provide a relative measure of the scattered flux. The detector plane is segmented (6 radial bins with five of them divided into 28

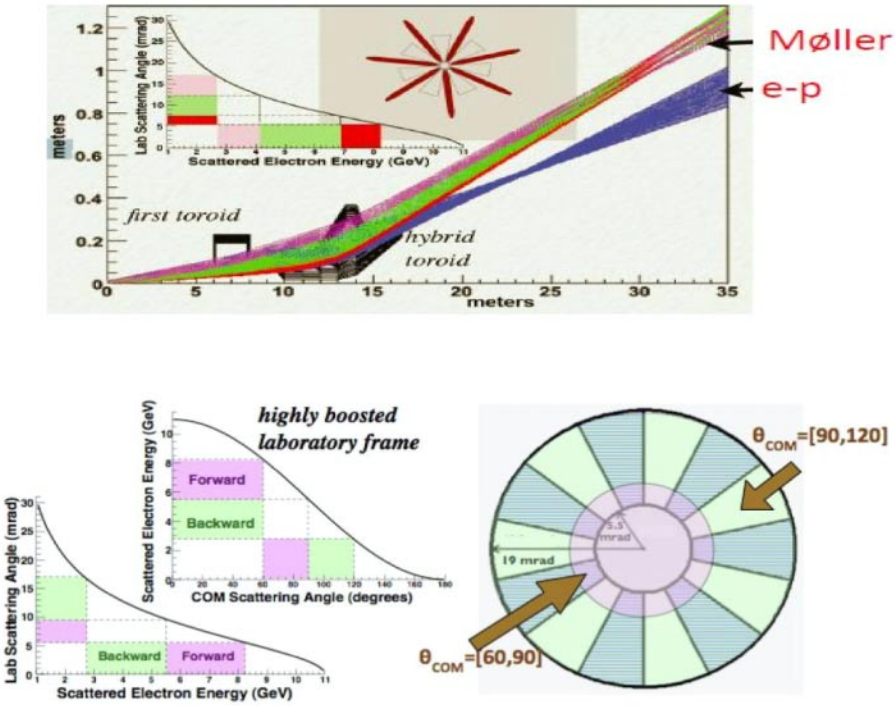

Fig. 34. – From ref. [146]. The principle of the MOLLER experiment. Top: the envelope of the scattered electron trajectories inside the spectrometer system consisting of a pair of toroidal magnets. The high-energy, low-angle Møller electrons are not greatly affected by the upstream magnet, whose total field integral is small. The lowest energy, highest angle Møller electrons are instead bent even further away from the beam line, allowing these particles to skirt the strongest field in the downstream magnet. The downstream magnet is designed so that particles at different radial distances from the beam feel very different field integral. This allows the hard, low-angle Møller electrons to be bent strongly to the radial focal position while the soft, high-angle particles are merely tickled into place. The Møller electrons will be incident on a system of quartz detectors. Bottom left: Θ_{COM} *vs.* E'_{Lab} for $E_{\mathrm{beam}} = 11\,\mathrm{GeV}$, and E'_{Lab} *vs.* θ_{lab}. Because of the Møller scattering features there is a one-to-one correspondence between Θ_{COM} (the scattering angle in the Center of Mass system) and the laboratory frame scattered electron energy E'_{Lab}. The energy-angle correlation also implies that there is a one-to-one correspondence between E'_{Lab} and θ_{lab} (the laboratory scattering angle). Bottom right: the concept for the primary acceptance collimator, which is able to achieve 100% acceptance with judiciously chosen ϕ-sectors. Since in the Møller scattering one deals with identical particles, those that are accepted in one ϕ bite also represent all the statistics available in the ϕ bite that is diametrically opposed $(180^\circ + \phi)$. In the figure, each clear ϕ sector is diametrically opposed by a shaded region, which would be shielded from the target and can be used to house magnet coils without any loss of acceptance.

azimuthal channels each and the radial bin corresponding to the Møller peak divided into 84 azimuthal channels) in order to achieve a complete understanding of the signal, background fraction and spectrometer optics. In fact (see fig. 35), high-momenta low-angle electrons produced by elastic electron-proton scattering will focus on the detector plane at smaller radii than the Møller electrons and their azimuthal distribution will be

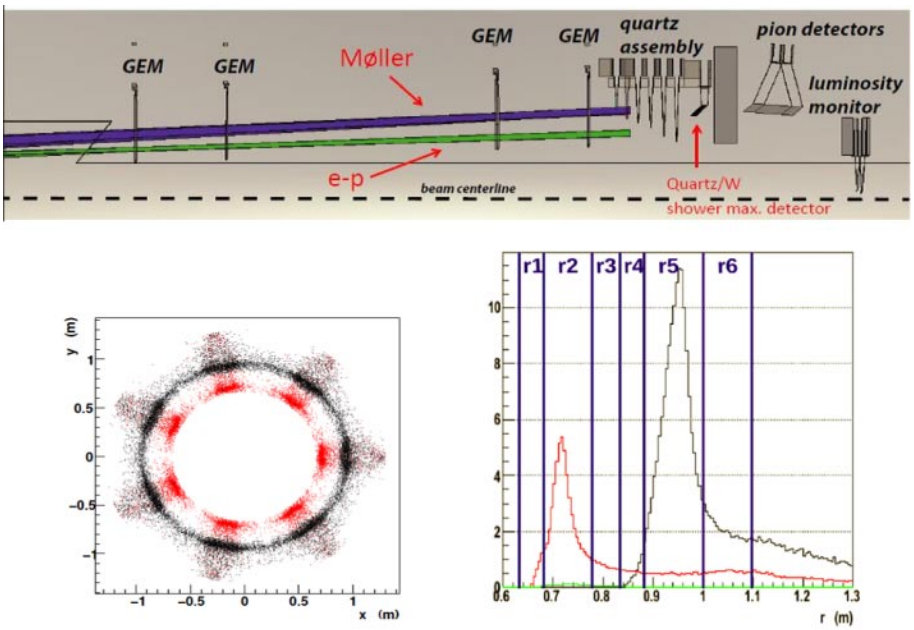

Fig. 35. – From ref. [146]. Top: layout of the main integrating and tracking detectors. Elastically scattered electrons off target protons (green) and electrons (blue) are also shown. Bottom left: transverse distribution of Møller (black) and ep (red) electrons 28.5 m downstream of target. Bottom right: radial segmentation of the scattered electron flux. The vertical lines correspond to the radial segmentation of the quartz detectors. The black, red and green curves are for electrons from Møller, elastic e-p and inelastic e-p scattering.

irregular, with gaps interspersed with areas of high density, while the azimuth angle of the Møller electrons will be function of their energy as quoted above. Moreover, the background generated by electrons produced by inelastic electron-proton scattering will produce a variation of the radial detector response as a function of the azimuth. An additional shower-max quartz/tungsten sandwich detector will provide a second independent measurement of the flux in the main Møller peak. This detector will be less sensitive to soft photon and charged hadron backgrounds. Lead-glass detectors placed behind the main Møller ring detectors and shielding, combined with two planes of gas electron multipliers (GEMs) will measure hadronic background dilutions and asymmetries during runs at very low current. A movable small single Čerenkov detector made of fused silica mounted on an x, y motion stage covering one sector of the acceptance, and located just upstream of the main detectors, will act as focal plane scanner. Three planes of GEM tracking detectors will be inserted periodically at very low current to track individual particles during calibration runs to measure the detailed shapes of all the charged particle trajectories. A luminosity monitor, consisting of quartz detectors, will detect the charged particle flux at extreme forward angles. A "two-bounce" collimation system will suppress neutral background from soft photons and neutrons. The predicted value of $A_{\mathrm{PV}}^{\mathrm{Moll}}$ for the experiment MOLLER is 35 ppb and the goal is to measure this quantity with a precision of 0.73 ppb. The construction of the MOLLER apparatus will start in the near future and work is also being done to improve beam transport and instrumentation.

6. – Parity Violating asymmetry in the nucleon resonance region

In the former sections we have reported about Parity Violating measurements in the elastic, quasielastic and Deep Inelastic electron scattering. Parity Violating asymmetry measurements in the nucleon resonance region were performed mainly to provide important constraints to nucleon resonance models relevant for calculating background corrections to elastic Parity Violating Electron Scattering measurements. However, recently their importance has increased because they are a powerful tool to check if quark-hadron duality, verified in electromagnetic interactions, is a universal feature of the quark-hadron transition and is hence also valid in charged lepton scattering via the weak interaction as speculated in [147]. In addition, in the resonance region, the Parity Violating structure functions can be described in terms of longitudinal, transverse, and axial Parity Violating response functions to specific resonance states, together with a non-resonant background, and can be decomposed in terms of their isospin content. Their measurement is hence sensitive to combinations of quark currents weighted by their electroweak couplings to the incident electrons.

The experiment PVDIS, already described in sect. **5**˙1, performed measurements of the Parity Violating asymmetry in electron scattering on deuteron at four kinematics in the nucleon resonance region. For three of these kinematics the beam energy was 4.867 GeV and the Q^2 values and the W values were 0.950, 0.831, and 0.757 $(\mathrm{GeV/c})^2$ and 1.263, 1.591, and 1.857 GeV respectively. For the fourth kinematics, the beam energy was 6.067 GeV, the Q^2 value was 1.472 $(\mathrm{GeV/c})^2$, and the W value was 1.981 GeV. For each kinematics the asymmetry was corrected for the beam depolarization caused by the passage of the beam through material before scattering, for target impurity due to the presence of a small amount of hydrogen deuteride, for the beam polarization components in the direction perpendicular to the scattering plane and for the background from π_0, the aluminum target windows, and events rescattering off the inner walls of the High Resolution Spectrometers. Background from the aluminum target windows was estimated using eq. (83), with structure functions $F_{1,3}^{\gamma Z}$ for aluminum constructed from the MSTW DIS PDF [118] extrapolated to the measured $\langle Q^2 \rangle$ and $\langle W \rangle$ values and the latest world fit on the ratio of longitudinal to transverse virtual photon electromagnetic absorption cross-sections $R \equiv \frac{\sigma_L}{\sigma_T}$ [148]. Radiative corrections were performed for both internal and external bremsstrahlung as well as ionization loss. External radiative corrections were performed based on the procedure first described by Mo and Tsai [149], and taking into account, in the simulation, the effect of the acceptance and particle identification efficiency variation across the acceptance. As inputs to the radiative corrections, Parity Violating asymmetries of elastic scattering from the deuteron were estimated using refs. [25, 17, 150, 151] and those from quasielastic scattering were based on ref. [4]. The box-diagram corrections were estimated and applied. The corrected asymmetries [152] were in agreement with calculations from Matsui, Sato, and Lee [153] (for $\Delta(1232)$ only), Gorchtein, Horowitz, and Ramsey-Musolf [67], and the Adelaide-JLab-Manitoba model [133]. The corrected asymmetries were in agreement also with an estimation made using Parton Distribution Functions (PDF) fits obtained from Deep Inelastic Scattering (DIS) data, extrapolated to the resonance region, along with the quark-Z^0 vector and axial couplings $g_{V,A}^q$ based on Standard Model values [113], with electroweak radiative corrections applied directly to $g_{V,A}^q$. For this estimation three PDF fits: MSTW [118], CTEQ-Jefferson Lab (CJ) [154], and CT10 [155], extrapolated to the measured $\langle Q^2 \rangle$ and $\langle W \rangle$ were used along with world data on R [148]. The differences among all three fits were below 1.5 ppm for all kinematics. The agreement between the

corrected asymmetries and the estimation made using (PDF) fits from (DIS) data shows that for the Q^2 range covered by the four kinematics, duality holds throughout the whole resonance region at the 10–15% level. PVDIS therefore provided the first experimental support for the hypothesis that quark-hadron duality is a universal property of nucleons in both their weak and their electromagnetic interactions.

The G0 experiment, already described in sect. **3**, measured, in "backward mode", the Parity Violating asymmetry in inelastic electron-proton scattering near the $\Delta(1232)$ resonance and found excellent agreement between its result and theoretical expectations based on the formalisms of ref. [13] and ref. [153]. The measurement determined in addition the axial transition form factor, $G_{N\Delta}^{A}$, that was consistent with the theoretical formalism of ref. [13]. These results are not yet published on a refereed journal [156].

Always in "backward mode", the G0 experiment measured the Parity Violating asymmetry in the inclusive electroproduction of π^- near the Δ^0 resonance [157]. This measurement can be expressed as a function of the asymmetries in the pion production due directly to the beam electrons and to the photons generated trough bremsstrahlung by the beam electrons

$$A_{\mathrm{PV}}^{\pi^-} = f_{\mathrm{brems}} D(y) A_\gamma^- + f_{\mathrm{virt}} A_e^-(Q^2), \tag{124}$$

with f_{brems} and f_{virt} the fractional fluxes of pions initiated by bremsstrahlung photons and virtual photons (*i.e.*, electroproduction), respectively ($f_{\mathrm{brems}} + f_{\mathrm{virt}} = 1$), y the fractional energy carried by the photon, $D(y)$ the degree of circular polarization carried by the bremsstrahlung beam, relative to the electron beam, $A_e^-(Q^2)$ the asymmetry for electroproduction of pions and A_γ^- defined as

$$A_\gamma^- = \frac{\mathrm{d}\sigma_R - \mathrm{d}\sigma_L}{\mathrm{d}\sigma_R + \mathrm{d}\sigma_L}, \tag{125}$$

with $\mathrm{d}\sigma_{R(L)}$ the differential cross-sections for right(left)-circular-polarized incident photons. A_γ^- is an important quantity. Expected to be zero in the absence of radiative corrections, could be not null in case of electron scattering from nucleons, because Parity Violation also occurs in weak interactions among quarks, and this form of an electroweak radiative correction can lead to non-zero asymmetries in the photoproduction limit. According to ref. [158], using Heavy Baryon chiral Perturbation Theory (HBχPT), neglecting non-resonant, higher-order chiral, and $\frac{1}{M_N}$ corrections, A_γ^-, for the $\vec{\gamma} + d \to \Delta^0 + p \to \pi^- + p + p$ process is equal to

$$A_\gamma^- = -\frac{2d_\Delta^-}{C_3^V}\frac{M_N}{\Lambda_\chi}, \tag{126}$$

with C_3^V the dominant $N-\Delta$ vector transition form factor, M_N the mass of the nucleon, Λ_χ the scale of chiral symmetry breaking, and d_Δ^- a new low-energy constant in the effective weak Lagrangian characterizing the Parity Violation $\gamma N\Delta$ coupling. According to ref. [158] the value of A_γ^- could be in module potentially as large as 5.2 ppm.

The measurement was performed at 360 MeV, the lowest of the two beam energies employed by the experiment in "backward mode". The main source of background was due to misidentified electrons which did not create a signal above threshold in the Čerenkov detector (see sect. **3**), and was characterized in special data-taking runs where Time-Of-Flight (TOF) spectra for particles (their flight path being from the target to the FPDs)

were used as an alternate method to determine the particles' identities. By defining hard cuts on TOF, pure samples of pions and electrons could be defined, which would then be used to characterize Čerenkov performance. Particle fluxes could be estimated from two-Gaussian fits to the TOF spectrum. The CED-FPD pairs inside the kinematic acceptance corresponding to inclusive pion production (pion locus) were selected by requiring the electron contamination of the pion sample, in a given pair, before background correction, to be below 10%. The beam possessed a slight degree of polarization transverse to the direction of propagation, in the bend plane of the accelerator. This in turn resulted in a parity conserving azimuthal dependence to the asymmetries measured by the experiment, because of the azimuthal segmentation of the detectors into octants. Dedicated runs were conducted with the degree of transverse polarization arranged to be as large as possible, so that the sensitivity of the detector to this azimuthal asymmetry could be deduced. This rather strong azimuthal dependence, possibly resulting from a sensitivity to the LT interference term seen in parity conserving pion electroproduction, was corrected using the azimuthal pion asymmetries determined for transversely polarized beam, and the degree of transverse polarization measured using the luminosity monitors that, being segmented azimuthally, were sensitive to the degree of the beam transverse polarization. After all the corrections the measured Asymetry was

$$A = -0.55 \pm 1.03\ (\text{stat}) \pm 0.37\ (\text{syst})\ \text{ppm}. \tag{127}$$

Because the experiment G0 did not detect scattered electrons in coincidence with the scattered pions, to derive A_γ^- from eq. (127) and eq. (124), Monte Carlo simulations were performed to evaluate f_{virt}, $\langle D(y)\rangle$, and $\langle Q^2\rangle$. Besides, the theoretical expectation that $A_e^-(Q^2)$ is approximately linear in Q^2 for the range of Q^2 of the experiment, with the intercept at $Q^2 = 0$ being equal to A_γ^- was assumed. Theoretical input was used to constrain the slope of the electroproduction asymmetry with Q^2. The simulation of the pion rate was found to agree with the data to within 15%. The resulting A_γ^- value was

$$A_\gamma^- = -0.36 \pm 1.06\ (\text{stat}) \pm 0.37\ (\text{syst}) \pm 0.03\ (\text{theor})\ \text{ppm}, \tag{128}$$

with the last error the theoretical uncertainty on the slope of $A_e^-(Q^2)$ with Q^2. From eq. (128) and eq. (126), with the values $C_3^V = 1.6$ and $\Lambda_\chi = 1\,\text{GeV}$ derived from ref. [159]. the following value of d_Δ^- was obtained:

$$d_\Delta^- = g_\pi(8.1 \pm 23.7\ (\text{stat}) \pm 8.3\ (\text{syst}) \pm 0.7\ (\text{theor})), \tag{129}$$

with $g_\pi = 3.8 \times 10^{-8}$. This result limits possible large Parity Violating asymmetry in pion photoproduction on the Δ resonance to the ppm level.

7. – Conclusion

Although the existence of weak neutral currents predicted by Abdus Salam's, Sheldon Glashow's and Steven Weinberg's unified theory of electroweak interactions was proved in 1973, in a neutrino experiment (the Gargamelle experiment at CERN), it was only with the experiment E122 at SLAC that the Parity Violating effects predicted by this theory were observed. This experiment proved beyond any doubt that parity is violated in scattering of electrons on protons and deuterons. The experiment SLACE122 was a

historical success. After it, many experiments that measured Parity Violating asymmetry in electron scattering followed and measured smaller and smaller asymmetries thanks to the use of high-intensity beams that decreased the statistical errors, to the availability of increasing high-quality beam whose features were more and more independent of the helicity of the beam, and to improved technologies that made it possible to reduce the systematic errors. This reduction in the minimum measurable Parity Violating asymmetry value and in its uncertainty had important consequences, making measurements at small Q^2 values possible, and consequently making possible the determination of strange quark contributions to the charge and magnetization of the nucleon (asymmetries of the order of 10^{-6}), of the neutron radius in heavy nuclei (asymmetries of the order of 5×10^{-7}), of the weak couplings between the electron and the quarks through Parity Violating Deep Inelastic Scattering (asymmetries of the order of 10^{-5} but with significant improvements in the reduction of the systematic error with respect of the experiment SLACE122), the determination of the weak charge of the proton (asymmetries of the order of 3×10^{-7}) and the measurement of the Parity Violating asymmetry in the Møller scattering (asymmetries of the order of 10^{-7}). The latter three kinds of experiments were of fundamental importance for testing the Standard Model and for the search of new physics. This topic will be the main goal of the physics studies in the future and will be the main goal of the next generation of experiments measuring Parity Violating asymmetry in electron scattering too, that are planning to measure asymmetries as low as 20–30 ppb (experiment P2 at Mainz and experiment MOLLER at JLab) with an uncertainty at the level of 2%. As quoted above, these so small asymmetries will be measurable thanks to the adoption of techniques and technologies on the frontier. With the decreasing of the measured asymmetries and of their uncertainties, some of the theoretical uncertainties that were once just added in the total errors on the physics quantities to be determined through measurements of the Parity Violating asymmetries in electron scattering have now to be reduced in order to get physical information from the measurements. To underline the importance that Parity Violating asymmetry measurements in electron scattering will have in the future we can just mention the importance of the P2 experiment at Mainz and the MOLLER experiment at Jlab that, as quoted above, will measure the smallest asymmetries ever reached, aiming to determine, respectively, the weak charge of the proton and the weak charge of the electron with very high precision. Comparing these two weak charges can be a diagnostic tool to determine whether or not the early Universe was supersymmetric and wether or not there is supersymmetric dark matter. The high-precision measurements of $\sin^2 \theta_W$ performed by the P2 and the MOLLER experiments will possibly be able to detect the modifications on the effective Lagrangian of Weak Neutral Current scattering produced by the dark photon Z, the supposed counterpart of the photon in the visible universe, that interacts with the components of dark matter. Thus, in the future, the measurements of the Parity Violating asymmetry will explore the very exciting field of the searches on dark matter.

REFERENCES

[1] Lee T. D. and Yang C.-N., *Phys. Rev.*, **104** (1956) 254.
[2] Wu C. S., Ambler E., Hayward R. W., Hoppes D. D. and Hudson R. P., *Phys. Rev.*, **105** (1957) 1413.
[3] Cates G. D. *et al.*, *Nucl. Instrum. Methods Phys. Res. A*, **278** (1989) 293.
[4] Aniol K. A. *et al.*, *Phis. Rev. C*, **69** (2004) 065501.
[5] Prescott C. Y. *et al.*, *Phys. Lett. B*, **77** (1978) 347.

[6] Prescott C. Y. *et al.*, *Phys. Lett. B*, **84** (1979) 524.
[7] Moreno O., talk at PAVI14 workshop, available at `http://www.pavi14.syr.edu`.
[8] Kaplan D. B. and Manohar A., *Nucl. Phys. B*, **310** (1988) 527.
[9] McKeown R. D., *Phys. Lett. B*, **219** (1989) 140.
[10] Mueller B. *et al.*, *Phys. Rev. Lett.*, **78** (1997) 3824.
[11] Barnet R. M. *et al.* (Particle Data Group), *Phys. Rev. D*, **54** (1996) 1.
[12] Abe K. *et al.*, *Phys. Rev. Lett.*, **74** (1995) 346.
[13] Musolf M. J. *et al.*, *Phys. Rep.*, **239** (1994) 1.
[14] Musolf M. J. and Holstein B. R., *Phys. Lett. B*, **242** (1990) 461.
[15] Musolf M. J. *et al.*, *Phys. Rev. C*, **50** (1994) 2173.
[16] Hasty R. *et al.*, *Science*, **290** (2000) 2117.
[17] Beise E. J., Pitt M. L. and Spayde D. T., *Prog. Part. Nucl. Phys.*, **54** (2005) 289.
[18] Mueller B. A. *et al.*, *Phys. Rev. Lett.*, **78** (1997) 3824.
[19] Spayde D. T. *et al.*, *Phys. Rev. Lett.*, **84** (2000) 1106.
[20] Spayde D. T. *et al.*, *Phys. Lett. B*, **583** (2004) 79.
[21] Galster S. *et al.*, *Nucl. Phys. B*, **32** (1971) 221.
[22] Zhu S.-L., Puglia S. J., Holstein B. R. and Ramsey-Musolf M. J., *Phys. Rev. D*, **62** (2000) 033008.
[23] Ito T. M. *et al.*, *Phys. Rev. Lett.*, **92** (2004) 102003.
[24] Schiavilla R., Carlson J. and Paris M., *Phys. Rev. C*, **67** (2003) 032501(R).
[25] Pollock S. J., *Phys. Rev. D*, **42** (1990) 3010.
[26] Acha A. *et al.*, *Phys. Rev. Lett.*, **98** (2007) 032301.
[27] Aniol K. A. *et al.*, *Phys. Rev. Lett.*, **82** (1999) 1096.
[28] Aniol K. A. *et al.*, *Phys. Lett. B*, **509** (2001) 211.
[29] Aniol K. A. *et al.*, *Phys. Lett. B*, **635** (2006) 275.
[30] Aniol K. A. *et al.*, *Phys. Rev. Lett.*, **96** (2006) 022003.
[31] Friedrich J. and Walcher Th., *Eur. Phys. J. A*, **17** (2003) 607.
[32] Ziskin V., PhD Thesis, MIT (2005).
[33] Geis E. *et al.*, *Phys. Rev. Lett.*, **101** (2008) 042501.
[34] Park N. W. and Weigel H., *Nucl. Phys. A*, **541** (1992) 453.
[35] Hammer H. W., Meissner U. G. and Drechsel D., *Phys. Lett. B*, **367** (1996) 323.
[36] Hammer H. W. and Ramsey-Musolf M. J., *Phys. Rev. C*, **60** (1999) 045204.
[37] Silva A. *et al.*, *Phys. Rev. D*, **65** (2001) 014016.
[38] Lewis R. *et al.*, *Phys. Rev. D*, **67** (2003) 013003.
[39] Leinweber D. B. *et al.*, *Phys. Rev. Lett.*, **94** (2005) 212001; **97** (2006) 022001.
[40] Ahmed Z. *et al.*, *Phys. Rev. Lett.*, **108** (2012) 102001.
[41] Arrington J. and Sick I., *Phys. Rev. C*, **76** (2007) 035201.
[42] Nakamura K. *et al.* (Particle Data Group), *J. Phys. G*, **37** (2010) 075021.
[43] Baunack S. *et al.*, *Phys. Rev. Lett.*, **102** (2009) 151803.
[44] Maas F. E. *et al.*, *Phys. Rev. Lett.*, **94** (2005) 152001.
[45] Maas F. E. *et al.*, *Phys. Rev. Lett.*, **93** (2004) 022002.
[46] El-Yakoubi M. A. *et al.*, in *Proceedings of 3rd Workshop on Parity Violation PAVI 2006, Milos, June 2006* (ref. [2]) p. 119.
[47] Androić D. *et al.*, *Nucl. Instrum. Methods Phys. Res. A*, **646** (2011) 59.
[48] Armstrong D. S. *et al.*, *Phys. Rev. Lett.*, **95** (2005) 092001.
[49] Kelly J. J., *Phys. Rev. C*, **70** (2004) 068202.
[50] Bernard V., Elouadrhiri L. and Meissner U. G., *J. Phys. G*, **28** (2002) R1.
[51] Leader E., Sidorov A. V. and Stamenov D. B., *Phys. Rev. D*, **67** (2003) 074017.
[52] Arrington J., *Phys. Rev. C*, **69** (2004) 022201(R).
[53] Anroič D. *et al.*, *Phys. Rev. Lett.*, **104** (2010) 012001.
[54] Roos P. G., *Eur. Phys. J. A*, **24, s2** (2005) 59.
[55] Schiavilla R., Carlson J. and Paris M., *Phys. Rev. C*, **70** (2004) 044007.
[56] Beck D. H. and McKeown R. D., *Annu. Rev. Nucl. Part. Sci.*, **51** (2001) 189.
[57] Bodek A. *et al.*, *Eur. Phys. J. C*, **53** (2008) 349.
[58] Tsai Y.-S., SLAC Report No. SLAC-Pub-848 (1971).

[59] Tjon J. A., Blunden P. G. and Melnitchouk W., *Phys. Rev. C*, **79** (2009) 055201.
[60] Liu J., McKeown R. D. and Ramsey-Musolf M. J., *Phys. Rev. C*, **76** (2007) 025202.
[61] Leinweber D. *et al.*, *Phys. Rev. Lett.*, **94** (2005) 212001; Leinweber D. *et al.*, *Phys. Rev. Lett.*, **97** (2006) 022001; Wang P. *et al.*, *Phys. Rev. C*, **79** (2009) 065202.
[62] Doi T. *et al.*, *Phys. Rev. D*, **80** (2009) 094503.
[63] Airapetian A. *et al.*, *Phys. Lett. B*, **666** (2008) 446.
[64] Blunden P. G., Melnitchouk W. and Thomas A. W., *Phys. Rev. Lett.*, **107** (2011) 081801.
[65] Sibirtsev A. *et al.*, *Phys. Rev. D*, **82** (2010) 013011.
[66] Gorchtein M. and Horowitz C. J., *Phys. Rev. Lett.*, **102** (2009) 091806.
[67] Gorchtein M., Horowitz C. J. and Ramsey-Musolf M. J., *Phys. Rev. C*, **84** (2011) 015502.
[68] Young R. D., Roche J., Carlini R. D. and Thomas A. W., *Phys. Rev. Lett.*, **97** (2006) 102002.
[69] Thomas A. W., Shanahan P. E. and Young R. D., *Nuovo Cimento C*, **35** (2012) 3.
[70] Donnelly T. W., Dubach J. and Sick I., *Nucl. Phys. A*, **503** (1989) 589.
[71] Abrahamyan S. *et al.*, *Phys. Rev. Lett.*, **108** (2012) 112502.
[72] Garcia-Recio C., Nieves J. and Oset E., *Nucl. Phys. A*, **547** (1992) 473.
[73] Ray L., Coker W. R. and Hoffmann G. W., *Phys. Rev. C*, **18** (1978) 2641.
[74] Starodubsky V. E. and Hintz N. M., *Phys. Rev. C*, **49** (1994) 2118.
[75] Clark B. C., Kerr L. J. and Hama S., *Phys. Rev. C*, **67** (2003) 054605.
[76] Trzcinska A. *et al.*, *Phys. Rev. Lett.*, **87** (2001) 082501.
[77] Lenske H., *Hyperfine Interact.*, **194** (2009) 277.
[78] Horowitz C. J., *Phys. Rev. C*, **57** (1998) 3430.
[79] Hebeler K., Lattimer J. M., Pethick C. J. and Schwenk A., *Phys. Rev. Lett.*, **105** (2010) 161102.
[80] Gandolfi S., Carlson J. and Reddy S., *Phys. Rev. C*, **85** (2012) 032801(R).
[81] Horowitz C. J. and Piekarewicz J., *Phys. Rev. C*, **64** (2001) 062802.
[82] Ozel F., Baym G. and Guver T., *Phys. Rev. D*, **82** (2010) 101301.
[83] Steiner A. W., Lattimer J. M. and Brown E. F., *Astrophys. J.*, **722** (2010) 33.
[84] Horowitz C. J. and Piekarewicz J., *Phys. Rev. C*, **66** (2002) 055803.
[85] Horowitz C. J. and Piekarewicz J., *Phys. Rev. Lett.*, **86** (2001) 5647.
[86] Lynch W. G. *et al.*, *Prog. Part. Nucl. Phys.*, **62** (2009) 427.
[87] Pollock S. J., Fortson E. N. and Wilets L., *Phys. Rev. C*, **46** (1992) 2587.
[88] Pollock S. J. and Welliver M. C., *Phys. Lett. B*, **464** (1999) 177.
[89] Michael R., talk at the workshop PAVI11, available at `http://www.roma1.infn.it/pavi11/`.
[90] Ban S., Horowitz C. J. and Michaels R., *J. Phys. G*, **39** (2012) 015104.
[91] Lalazissis G. A., Konig J. and Ring P., *Phys. Rev. C*, **55** (1997) 540.
[92] Todd-Rutel B. G. and Piekarewicz J., *Phys. Rev. Lett.*, **95** (2005) 122501.
[93] Beiner M., Flocard H., van Giai N. and Quentin P., *Nucl. Phys. A*, **238** (1975) 29.
[94] Chabanat E., Bonche P., Haensel P., Meyer J. and Schaeffer R., *Nucl. Phys. A*, **635** (1998) 231.
[95] Vautherin D. and Brink D. M., *Phys. Rev. C*, **5** (1972) 626.
[96] Ong A., Berengut J. C. and Flambaum V. V., *Phys. Rev. C*, **82** (2010) 014320.
[97] Frois B. *et al.*, *Phys. Rev. Lett.*, **38** (1977) 152.
[98] Horowitz C. J. *et al.*, *Phys. Rev. C*, **85** (2012) 032501(R).
[99] Jefferson Lab Experiment E12-11-101 (PREX-II). Proposal available at `http://hallaweb.jlab.org/parity/prex`.
[100] Jefferson Lab Experiment E12-12-004 (CREX). Proposal available at `http://hallaweb.jlab.org/parity/prex`
[101] Forssén C., Hagen G., Hjorth-Jensen M., Nazarewicz W. and Rotureau J., *Phys. Scr. T*, **152** (2013) 014022.
[102] Bender M., Heenen P.-H. and Reinhard P.-G., *Rev. Mod. Phys.*, **75** (2003) 121.

[103] Hagen G. *et al.*, C-REX Workshop 2013, available at `http://www.jlab.org/conferences/crex/program.html`
[104] Ekström A. *et al.*, *Phys. Rev. Lett.*, **110** (2013) 192502.
[105] Holt J. D. *et al.*, *J. Phys. G*, **39** (2012) 085111.
[106] Hebeler K. and Furnstahl R. J., *Phys. Rev. C*, **87** (2013) 031302.
[107] Tews I., Krueger T., Hebeler K. and Schwenk A., *Phys. Rev. Lett.*, **110** (2013) 032504.
[108] Souder P. A. *et al.*, *Phys. Rev. Lett.*, **65** (1990) 694.
[109] Feinberg G., *Phys. Rev. D*, **12** (1975) 3575.
[110] Walecka J. D., *Nucl. Phys. A*, **285** (1977) 349.
[111] Androić D. *et al.*, *Phys. Rev. Lett.*, **111** (2013) 141803.
[112] Dzuba V. A., Berengut J. C., Flambaum V. V. and Roberts B., *Phys. Rev. Lett.*, **109** (2012) 203003.
[113] Beringer J. *et al.* (Particle Data Group), *Phys. Rev. D*, **86** (2012) 010001.
[114] Heil W. *et al.*, *Nucl. Phys. B*, **327** (1989) 1.
[115] Wang D. *et al.*, *Nature*, **506** (2014) 67.
[116] Zheng X.-C., Michaels R. and Reimer P. E. (Spokespersons), $\vec{e}-{}^2$H Parity Violating Deep Inelastic Scattering (PVDIS) at CEBAF 6 GeV, proposal to Jefferson Lab PAC-33.
[117] Alcorn J. *et al.*, *Nucl. Instrum. Methods Phys. Res. A*, **522** (2004) 294.
[118] Martin A. D. *et al.*, *Eur. Phys. J. C*, **63** (2009) 189.
[119] Wood C. S. *et al.*, *Science*, **275** (1997) 1759.
[120] Bennet S. C. *et al.*, *Phys. Rev. Lett.*, **82** (1999) 2484; **83** (1999) 889(E).
[121] Ginges J. S. M. and Flambaum V. V., *Phys. Rep.*, **397** (2004) 63.
[122] Eichten E., Lane K. D. and Peskin M. E., *Phys. Rev. Lett.*, **50** (1983) 811.
[123] Schael S. *et al.*, *Phys. Rep.*, **532** (2013) 119.
[124] Jefferson Lab Experiment E12-10-007. Proposal available at `https://hallaweb.jlab.org/wiki/index.php/SoLID`.
[125] Mantry S., Ramsey-Musolf M. J. and Sacco G. F., *Phys. Rev. C*, **82** (2010) 065205.
[126] Castorina P. and Mulders P. J., *Phys. Rev. D*, **31** (1985) 2760.
[127] Fajfer S. and Oakes R. J., *Phys. Rev. D*, **30** (1984) 1585.
[128] Martin A. D., Roberts R. G., Stirling W. J. and Thorne R. S., *Eur. Phy. J. C*, **39** (2005) 155.
[129] Rodionov E. N., Thomas A. W. and Londergan J. T., *Mod. Phys. Lett. A*, **9** (1994) 1799.
[130] SOLID, Preliminary Conceptual Design Report available at `https://hallaweb.jlab.org/wiki/index.php/SoLID`.
[131] Erler J. and Ramsey-Musolf M. J., *Prog. Part. Nucl. Phys.*, **54** (2005) 351.
[132] Young R. D., Carlini R. D., Thomas A. W. and Roche J., *Phys. Rev. Lett.*, **99** (2007) 122003.
[133] Hall N. L., Blunden P. G., Melnitchouk W., Thomas A. W. and Young R. D., *Phys. Rev. D*, **88** (2013) 013011.
[134] Maas F. talk at PAVI14 workshop, available at `http://www.pavi14.syr.edu`.
[135] Zeldovich Ya. B., *Sov. Phys. JETP*, **94** (1959) 262.
[136] Czarnecki A. and Marciano W. J., *Int. J. Mod. Phys. A*, **15** (2000) 2365.
[137] Derman E. and Marciano W. J., *Ann. Phys. (N.Y.)*, **121** (1979) 147.
[138] Czarnecki A. and Marciano W. J., *Phys. Rev. D*, **53** (1996) 1066.
[139] Erler J. and Ramsey-Musolf M. J., *Phys. Rev. D*, **72** (2005) 073003.
[140] Anthony P. L. *et al.*, *Phys. Rev. Lett.*, **92** (2004) 181602.
[141] Anthony P. L. *et al.*, *Phys. Rev. Lett.*, **95** (2005) 081601.
[142] Erler J., Kurylov A. and Ramsey-Musolf M. J., *Phys. Rev. D*, **68** (2003) 016006.
[143] Ferroglia A., Ossola G. and Sirlin A., *Eur. Phys. J. C*, **34** (2004) 165.
[144] Petriello F. J., *Phys. Rev. D*, **67** (2003) 033006.
[145] Eidelman S. *et al.* (Particle Data Group), *Phys. Lett. B*, **592** (2004) 1.
[146] Experiment MOLLER. Proposal available at `http://hallaweb.jlab.org/12GeV/Moller`.
[147] Carlson C. E. and Mukhopadhyay N. C., *Phys. Rev. D*, **47** (1993) R1737.

[148] Bosted P. E. and Christy M. E., *Phys. Rev. C*, **77** (2008) 065206.
[149] Mo L. W. and Tsai Y.-S., *Rev. Mod. Phys.*, **41** (1969) 205.
[150] Abbott D. *et al.*, *Eur. Phys. J. A*, **7** (2000) 421.
[151] Pollock S. J., *Phys. Rev. D*, **43** (1991) 2447.
[152] Wang D. *et al.*, *Phys. Rev. Lett.*, **111** (2013) 082501.
[153] Matsui K., Sato T. and Lee T.-S. H., *Phys. Rev. C*, **72** (2005) 025204.
[154] Owens J. F., Accardi A. and Melnitchouk W., *Phys. Rev. D*, **87** (2013) 094012.
[155] Lai H.-L. *et al.*, *Phys. Rev. D*, **82** (2010) 074024.
[156] Androić D. *et al.*, arXiv:1212.1637.
[157] Androić D.*et al.*, *Phys. Rev. Lett.*, **108** (2012) 122002.
[158] Zhu S.-L., Maekawa C. M., Holstein B. R. and Ramsey-Musolf M. J., *Phys. Rev. Lett.*, **87** (2001) 201802.
[159] Zhu S.-L., Maekawa C. M., Sacco G., Holstein B. R. and Ramsey-Musolf M. J., *Phys. Rev. D*, **65** (2001) 033001.